Examination of acoustic backscatter from an inhomogeneous volume beneath a planar interface

Hines, P. C.

Award date:
1988

Awarding institution:
University of Bath

EXAMINATION OF ACOUSTIC BACKSCATTER FROM AN INHOMOGENEOUS VOLUME BENEATH A PLANAR INTERFACE

Submitted by P.C. Hines

for the degree of Ph. D.

of the University of Bath

1988

COPYRIGHT

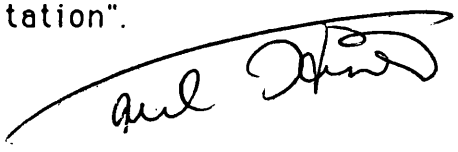

ProQuest LLC
789 East Eisenhower Parkway
P.O. Box 1346
Ann Arbor, MI 48106-1346

Dedicated to:

the memory of my parents who gave me
love as well as a love of knowledge,

Mr. Firman McCormick who taught by example that achieving
anything worthwhile requires discipline and dedication,

the Father, Son, and Holy Spirit without whom nothing is
complete.

Late 20th century scientist pictured with his principal research equipment; state-of-the-art chest waders and shovel.

ABSTRACT

Mathematical models of acoustic scattering from the ocean bottom presently available, generally fail to predict backscatter levels of sufficient magnitude, for two limiting cases; as the bottom becomes increasingly smooth and as the grazing angle becomes shallow. A mathematical model of acoustic backscattering is derived herein which attempts to address these shortcomings for the case of a sediment bottom. In the model, scattering results from fluctuations in concentration, where concentration is roughly defined as the water to particle ratio within the sediment. The model allows for penetration of the incident wave into the bottom at sub-critical grazing, and retransmission of scattered spherical waves through the (planar) interface. The frequency and grazing angle dependence of the acoustic backscatter are determined primarily by the correlation function of the concentration fluctuations, while the magnitude is controlled by the mean square value of these fluctuations.

To complement the modelling, a set of laboratory experiments were performed to measure volume backscatter from a smooth, water-saturated sand bottom at grazing angles from 10°-50° for frequencies of 25-200kHz. The model was further tested against backscatter data available in the literature over a wide range of frequency (2.5kHz-500kHz) for several sediment bottoms. Agreement between the model and both the author's data and the literature data is very good. It should be noted however, to obtain accurate model predictions, knowledge of the mean square value and correlation function of the concentration fluctuations is essential.

ACKNOWLEDGEMENTS

I wish to express my sincere thanks to my supervisor Dr. N.G. Pace as well as Dr. V.F. Humphrey and Prof. H.O. Berktay of the School of Physics for their valuable comments and criticism. Thanks are also due to the postgraduates in the underwater acoustic section, particularly Mr. A.C. Baker, Mr. G.D. Quartly, Mr. K. Anastasiadis and Mrs. C. Beckett for their general interest and many hours of informative discussion. I would also like to thank the other postgraduate students and many of the 57000 publicans in the U.K. for helping to make my stay in England so enjoyable. The technical support of Mr. B. Gay, Ms. C. Dyer and Mr. B. Ring is also acknowledged.

I wish to express my sincere gratitude to the staff of Defence Research Establishment Atlantic (DREA), Dartmouth, Canada for both technical and administrative assistance during this project; in particular, the invaluable contribution of Mr. J.S. Hutton at both a personal and professional level. Thanks are also due to the Canadian Dept. of National Defence for their financial support.

Finally and most importantly, I wish to express my deepest thanks to my wife Nancy, for her endless hours of assistance, patience, and encouragement, and for sacrificing so much of what was important to her that we might achieve what was important to me.

TABLE OF CONTENTS

LIST OF SYMBOLS FOR MAIN TEXT

This symbol list is for the main text. The appendices, have a separate list. Within the list, **bold** type denotes a complex number.

A	Scattering surface area insonified. See Equation (4.7).
A_{3dB}	Scattering surface area insonified to -3dB points.
A_0	Loss tangent of acoustic wavenumber, i.e. $k_s=\omega/c_0(1+iA_0)$.
a_0	Correlation length with spherical symmetry.
a_r,b_r,d_r,f_r,g_r	See Equation (3.22).
a_l,b_l,d_l,f_l,g_l	See Equation (3.33).
c	Acoustic wave speed (general).
c_w	Acoustic wave speed in water.
c_0	Average acoustic wave speed in the scattering volume. (specifically the bottom sediment).
C_l, D_l	See Equation (3.34).
C_r, D_r	See Equation (3.28).
D	Directivity of parametric array (PA).
f_{p1},f_{p2},f_d	Primary, difference frequency of PA in Hz.
i	$(-1)^{1/2}$.
I	Intensity of scattered wave (general).
I_0	Intensity of incident wave at scattering region.
I_s	Intensity of scattered wave at receiver.
I_{sr},I_{sl}	Refracted, lateral components of scattered wave.
$k,\mathbf{k}$	Acoustic wavenumber (general).
k_w,k_s	Acoustic wavenumber in water, bottom sediment.

k_d	Difference frequency wavenumber of PA.
K_r	Simplified notation for $\|k_s\|^2(a_r^2 + f_r^2)$.
K_l	Simplified notation for $\|k_s\|^2(a_l^2 + f_l^2)$.
L	Truncation range in calibration experiments.
L_m	Range past PA transducer of maximum difference frequency signal intensity.
L_c	Correlation length of concentration fluctuations.
L_v	Linear dimensions of insonified volume.
M_r	See Equation (3.19).
M_l	See Equation (3.30).
N_c	Correlation function of concentration fluctuations.
n_{sw}	k_w/k_s.
n_{ws}	k_s/k_w.
p, p	Acoustic pressure (general).
p_i, p_s	Incident, scattered acoustic pressure.
p_r,p_l	Refracted, lateral components of scattered wave.
P_0	Amplitude of incident wave.
Q	Source term. See Equation (3.11).
r	Range from source/receiver to scattering region i.e. $(r_T^2+z_w^2+z_s^2)^{1/2}$.
r_T	Horizontal range separating receiver from scattering point.
R_{tr}	Transducer-receiver separation in calibration experiments.
$\mathcal{R}$	Rayleigh reflection coefficient.
S	Concentration.
$\overline{(\Delta S)^2}$	Mean square value of concentration fluctuations (variance).

T_{ws}	Pressure transmission coefficient for plane wave incident from water.
T_{sw}	Pressure transmission coefficient for plane wave incident from bottom sediment.
V,V'	Scattering volume in relative, absolute coordinates.
dV,dV'	$dxdydz$, $dx'dy'dz$.
x_T,y_T	x,y components of r_T.
x,y,z	Relative Cartesian coordinates. See Equation (3.25).
x',y',z'	Absolute Cartesian coordinates. See Equation (3.26).
X_{3dB}	X dimension of A_{3dB}.
Y_{3dB}	Y dimension of A_{3dB}.
ΔY	Width of scattering volume.
z_w	Source height above water/bottom interface.
z_s	Scattering point depth below water/bottom interface.
z_0,r_0	Vertical, horizontal correlation lengths with radial symmetry.
z_0,x_0,y_0	Vertical, horizontal correlation lengths without radial symmetry.
$\alpha_{p1},\alpha_{p2},\alpha_d$	Absorption coefficient of primary and difference frequency of PA.
α_T	$\alpha_{p1}+\alpha_{p2}-\alpha_d$.
β	Incident angle of lateral wave in water. See Figure (3.2).
β'	Simplified notation for $(n_{ws}^2 - \sin^2\beta)^{1/2}$.
θ_i	Incident angle in water of incident wave. See Figure (3.1).

θ_0	Incident angle in bottom sediment of transmitted wave. See Figure (3.1).
θ_t	Incident angle of refracted wave in bottom. See Figure (3.2).
θ'	simplified notation for $(n_{sw}^2 - \sin^2\theta)^{1/2}$.
λ_p	Arithmetic mean of primary wavelengths of PA.
ρ	Density (general). Also integration variable in spherical polar coordinate system where noted.)
ρ_0	Average density in the scattering volume. Specifically the bottom sediment.
(ρ,θ,φ)	Spherical polar coordinates.
(r,θ,z)	Cylindrical polar coordinates.
σ_s	Surface backscatter coefficient. See Equation (4.7).
σ_v	Volume backscatter coefficient. See Equation (4.8).
τ	Pulse length.
φ_g	Grazing angle of incidence in water. (Complement of θ_1.)
ψ	One-sided -3dB intensity beamwidth of PA.
ω	Angular frequency in radians/second.
$\omega_{p1},\omega_{p2},\omega_d$	Primary, difference frequency of PA in radians/second.

ABBREVIATIONS

BSS	Backscattering Strength
CR	Composite Roughness
MSD	Method of Steepest Descents
PVC	Polyvinylchloride
RR	Rayleigh-Rice Approximation

RRC	Rayleigh Reflection Coefficient
XDUCER	Transducer

LIST OF SYMBOLS FOR APPENDICES

As the appendices are self-contained, many of the symbols occuring there are not found in the main text. For this reason, a separate symbol list has been compiled for the appendices. In the following list of symbols, **bold** type denotes a complex number.

A_0	Loss tangent of acoustic wavenumber, i.e. $k_s=\omega/c_0(1+iA_0)$.
A_{IC}	Pressure amplitude of incident compressional wave.
A_{TC}	Pressure amplitude of transmitted compressional wave.
A_{TS}	Pressure amplitude of transmitted shear wave.
a_w, a_b, b_b	See Equation (A.4).
a_r, b_r, d_r, f_r, g_r	See Equation (3.22).
C_r, D_r	See Equation (D.21).
c_{av}	Apparent velocity along the water/bottom interface.
c_{bc}, c_b	Compressional wave speed in bottom.
c_{bs}	Shear wave speed in bottom.
c_{wc}, c_w	Compressional wave speed in water.
c_0	Average acoustic wave speed in the bottom.
D	Partical diameter in microns.
E_b, G_b	Bulk modului of elasticity, rigidity of the bottom.
E_s, E_w, E_f	Bulk moduli of elasticity of sand, water, and frame.
F	See Equation (C.11).

$f(\Theta)$	See Equations (B.8) to (B.11).
$F(\Theta)$	See Equations (B.8) to (B.11).
$H_0^{(1)}(u)$	Zeroth order Hankel functions of first kind.
$H_0^{(2)}(u)$	Zeroth order Hankel functions of second kind.
i	$(-1)^{1/2}$.
$J_0(u)$	Zeroth order Bessel function.
k	Acoustic wavenumber magnitude.
k_w, k_s	Acoustic wavenumber in water, sediment.
M_r	See Equation (B.34).
M_l	See Equation (B.35).
N_c	Correlation function of concentration fluctuations.
n_{ws}, n_{sw}	k_s/k_w, k_w/k_s.
p_r, p_l	Refracted, lateral components of scattered wave.
p_t	$p_t + p_l$.
P	Porosity.
P_0	Amplitude of incident wave.
r	Scattering point to receiver range i.e. $(r_T^2+z_w^2+z_s^2)^{1/2}$.
r_T	Horizontal range separating receiver from scattering point.
$\mathcal{R}$	Rayleigh reflection coefficient.
S	Concentration.
T_{ws}	Pressure transmission coefficient for plane wave incident from water.
T_{sw}	Pressure transmission coefficient for plane wave incident from bottom sediment.
u	$k_s r_T \sin\Theta$.
V_w, V_b	Water volume, bottom volume.

x_T, y_T	The x, y components of r_T.
x,y,z	Relative Cartesian coordinates. See Equation (D.6a).
x',y',z'	Absolute Cartesian coordinates. See Equation (D.6b).
z_w	Receiver height above water/bottom interface.
z_s	Scattering point depth below water/bottom interface.
β, δ_1	See Equation (B.16).
Θ	Incident angle of refracted wave in bottom. Also spherical polar coordinate. See Figure (B.1).
μ_b	$c_{bs}^2 \rho_b$.
ρ_0	Average density of the bottom.
ρ_w	Density of water.
ρ_b	Density of bottom.
ρ_{w*}	Density of water as a solute.
ρ_{sd}	Density of dry sediment including air gaps.
ρ_{ss}	Density of a single sediment particle.
ρ_w	Density of water in the bottom corrected for the amount of volume it occupies. See Equation (C.4).
σ	See Equation (B.8).
$\Phi(0)$	See Equation (B.11).
φ	Spherical polar coordinate along with Θ.
φ_{IC}	Grazing angle of incident compressional wave. See Figure (A.1).
φ_{TC}	Grazing angle of transmitted compressional wave. See Figure (A.1).
φ_{TS}	Grazing angle of transmitted shear wave. See Figure (A.1).

ψ_l	Incident angle of lateral wave in water.
ψ_r	Incident angle of refracted wave in water.
ψ, δ_r	See Equation (B.31).
ψ', ψ''	Real, imaginary parts of ψ.
ψ_c	Critical angle ($\sin^{-1} n_{ws}$).
ψ	Incident angle of refracted wave in water. See Figure (B.1).
ω	Angular frequency in radians/second.

CHAPTER 1

INTRODUCTION

During the past several decades, much effort has been put into understanding the mechanisms which cause scattering of acoustic waves within the ocean. The scope of interest varies considerably: from military applications such as target detection, to biological interests in fish stocks, to geological surveying of the ocean bottom. Within each of these areas of interest, acoustic scattering can be categorized as resulting from:

a) inhomogeneities within the ocean volume such as microscopic sea life -this is generally referred to as volume scattering,

b) incoherent reflections at the water/surface interface due in part to surface waves, and in part to the bubble layer present immediately below the surface -this is generally referred to as surface scattering.

c) incoherent reflections from the water/bottom interface due to bottom roughness and from within the sea bed due to inhomogeneities -together, these are referred to as bottom scattering.

Each of these categories can be subdivided into special cases such as scatter in the specular direction (coherent scatter), and scattering antiparallel to the direction of the acoustic source (backscatter), to name two. Furthermore, each topic can be examined in terms of the usual parameters of frequency and grazing angle[1], as well as parameters specific to

---

[1] The grazing angle is the complement of the angle of incidence.

the type of scatter. For example, wind speed (in the case of surface scatter), depth (in the case of volume scatter), and bottom type and roughness (in the case of bottom scatter).

Because of the scope of interest involved in acoustic scattering in the ocean, it is necessary to limit any single research project to a fairly restricted area within this field. In this regard, the emphasis of the study contained herein is directed at backscatter from within the bottom volume and is outlined below.

1.1 Motivation For the Present Study

A great deal of research has been done in the field of bottom backscatter, most of which has been concentrated on that due to bottom roughness. Several "bottom roughness" models have been developed which attempt to estimate the magnitude of backscatter from the sea bed, as well as its dependence on frequency, grazing angle, bottom type and roughness. (cf. [1],[2],[3]) (There has also been a plethora of laboratory experiments, employing various model rough bottoms, to test the models quantitatively. cf. [4],[5],[6]) The models have been used with varying success to estimate backscatter from the ocean bottom. However, they all have one major shortcoming. Each fails to predict backscatter levels of sufficient magnitude, in the limit of a smooth bottom and/or shallow grazing.

It is generally accepted that the higher than estimated backscatter levels result from scattering from inhomogeneities within the sea bed. Most of the early models which tried to account for this considered the sea bed to consist of a large number of independent scatterers; each one uncorrelated with the

others. In 1963, Stockhausen[7] derived a scattering model for a bottom consisting of a uniform set of spherical particles. The model failed to predict the frequency independence (or near independence) observed in most ocean bottom backscatter experiments, and did not account for any return at sub-critical grazing. At about the same time, Nolle et alia[8] performed extensive laboratory experiments to measure backscatter from a volume of water-saturated sand. The expression they developed did follow the general trend of their data. However, it was unable to estimate absolute levels nor did it predict the relatively high levels of backscatter at shallow grazing. The model developed by Crowther[9] too, underestimates backscatter levels at shallow grazing.

Ivakin and Lysanov[10] have employed Chernov's[11] work on wave propagation in an inhomogeneous medium to develop a bottom backscattering model. While fairly crude, the model does account for correlation between scatterers and the frequency independence of much of the ocean bottom backscattering data. However, it approximates both the refractive index and the pressure transmission coefficient to unity, so as to avoid boundary considerations at the water/bottom interface. Furthermore, there were no quantitative laboratory experiments against which to test the model.

In the present paper, a detailed mathematical model of acoustic scattering from the volume beneath the bottom is derived. The model follows Chernov's work but accounts for the effects of a smooth water/bottom interface on transmission into and out of the sea bed. Following the mathematical development,

the results of a set of laboratory experiments performed on a model sea bed are presented, providing data against which to test the model. Finally, the robustness of the model is tested by comparing it to a range of experimental data contained in the literature.

Before deriving the model for backscatter from the bottom volume, we shall present an overview of some of the literature dedicated to the field of acoustic scatter in the past.

CHAPTER 2

LITERATURE SURVEY

In this chapter, a review of the research done in the field of underwater acoustic scattering is presented. Due to the volume of work done on the subject, it is virtually impossible to outline all related papers. However, this chapter contains a review of the most significant contributions in the field. The reader should note that for the most part, the notation employed in this chapter, follows that of the articles reviewed and is independent of the remainder of the thesis.

2.1 Scattering From Periodic Surfaces

Perhaps the most commonly cited reference with respect to acoustic wave scattering from a rough interface is the work of J.W. Strutt[12], (Lord Rayleigh), at the end of the 19th century. He examined acoustic scattering from interfaces with periodic undulations. Due to the periodicity of the undulations, the scattered pressure wave is assumed to propagate in discrete modes making angles Θ_i with the vertical, such that:

$$\sin(\Theta_i) = \sin(\Theta) + i\frac{\lambda}{\Lambda}; \quad i = 0,\pm1,\pm2... \tag{2.1}$$

where λ is the acoustic wavelength and Λ is the wavelength of the surface. Rayleigh's model agrees reasonably well with experiment so long as the interface relief is not too rough. However, the work is not without criticism. Uretsky[13] points out that one of the assumptions Rayleigh applies in his theoretical development is not at all obvious. Rayleigh assumes

that the expression for the total field, p(x,z), is valid everywhere above and on the boundary.

$$p(x,z) = e^{ik(x\sin\theta - z\cos\theta)} + \sum_{i=-\infty}^{\infty} A_i e^{ik(x\sin\theta_i + z\cos\theta_i)} \qquad (2.2)$$

where the A_i's are the amplitudes of the plane waves and k is the acoustic wavenumber defined as $k=2\pi/\lambda$.

Uretsky states that in particular the assumption breaks down in the valleys between the peaks. Uretsky rederived the scattering formula keeping Rayleigh's boundary conditions for $z \geq h$, but for $z<h$ (i.e. the "valleys") he used the Helmholtz formula with Green's functions. The Uretsky method is mathematically complicated in comparison to Rayleigh's, but is very rigorous and requires few assumptions.

Meecham[14] too, expressed concern over Rayleigh's second assumption. He used an error minimizing procedure to improve on Rayleigh's method. Heaps[1] cast doubt on the validity of Rayleigh's assumption in the following way. He attempted to estimate the pressure on the boundary by measuring the scattered pressure field and assuming it resulted from an infinite sum of plane waves. The estimate of the pressure at the boundary he obtained required the surface to be sound absorbing. (i.e. not a pressure release type.) Thus, near the surface one must account for types of re-radiation other than plane waves, all of which must be included in the boundary condition, which Rayleigh didn't do.

It is only fair to mention in defence of Rayleigh's method that most scientists who have analysed it, acknowledge its usefulness in dealing with surfaces of gentle undulations.

2.2 Scattering From a Random Boundary

The above papers all deal with scattering from a periodic boundary. This does provide insight into the problem of scattering from a rough surface. However the majority of surfaces encountered in underwater acoustic problems are random in nature. Thus, we need a theory to estimate scattering from random surfaces as well. For this situation two models are generally used and the adherents to each shall be discussed presently.

2.2.1 The Rayleigh-Rice (RR) Method

Steven Rice[15] developed this model to describe the scattering of electromagnetic waves from a perfectly conducting, randomly rough interface which is "almost, but not quite flat". He based the development on the same boundary conditions used by Rayleigh for the periodic surface, with the result that it suffers the same shortcomings. The validity of Rice's expression for the scattered field is further limited by his approximations of the constants in his expression for the total electric field. These constants, correct to order $f^2(x,y)$ (where the surface is described by $z=f(x,y)$) are determined by assuming that

$$kf(x,y)<<1 \text{ and } f_x, f_y<<1 \qquad (2.3)$$

where k is the wavenumber of the incident radiation and f_x, f_y are the gradients of $f(x,y)$ in the x and y directions. These are the small waveheight, small surface slope approximations.

Marsh[3] extended the Rayleigh-Rice method (henceforth denoted RR) to include scattering of acoustic waves from a pressure release interface. The interface he examined was a wind driven water surface. He developed the theory through "extensive use of Wiener's generalized harmonic analysis". (See Reference [16].) Marsh deals with a one-dimensional surface of the form z=z(x). He seeks an expression for the scattered pressure field 'g' of the form:

$$g \cdot e^{-i\omega t} = \int e^{-i(\lambda\xi - \nu kz)} dG(\lambda) \qquad (2.4)$$

where $\xi = kx$; and λ and ν are the direction cosines of the scattered wave and the generalized spectrum of g(z) is denoted $G(\lambda)$.

There corresponds to $G(\lambda)$, a correlation function, $\varphi(\xi)$, with the Fourier transform:

$$\Lambda(\lambda) = \frac{1}{2\pi}\int e^{i\lambda\xi}\varphi(\xi)\, d\xi \qquad (2.5)$$

where $\Lambda(\lambda)$ is proportional to the intensity of the scattered spectrum in the direction of the scattered wave. It is $\Lambda(\lambda)$ which Marsh seeks.

Marsh represents $G(\lambda)$ as a power series in σ, the rms surface height. By setting

$$G(\lambda) = \sum_{m=0}^{\infty} \sigma^m A_m(\lambda) \qquad (2.6)$$

and solving for the coefficients A_m (not a trivial exercise!) he obtains $G(\lambda)$. This can be substituted back into Equation (2.4) to obtain the scattered pressure, g. He obtains $\varphi(\xi)$, the correlation

function of the scattered pressure field from the usual definition of the correlation function; that is $\varphi(\xi) = \langle g(\xi)g^*(\xi')\rangle$. (The '*' denotes complex conjugate.)

Marsh, Schulkin and Kneale[17] use the method in a companion paper to solve for scattering from the ocean surface in the specular direction. They use the Neumann-Pierson[18] ocean roughness spectrum and solve only for the coefficients A_0, A_1, A_2 in determining $G(\Lambda)$. In Marsh[19], he retains the necessary terms in $\Lambda(\lambda)$ to estimate backscatter levels at shallow grazing as a function of frequency. The latter paper is little more than an outline however, limiting its usefulness.

In yet another paper, Marsh[20] reverses the process, using experimental measurements of the pressure field scattered from the surface of the North Sea to estimate the sea surface wave spectrum. He states that the spectrum deduced is "somewhat different than the Neumann-Pierson model employed in ([3] and [17]) but conforms well with the spectrum of Phillips[21] and Burling[22]".

Kuo[23] extended Marsh's model to include the case of imperfect reflectors. He examined backscatter in detail, deriving a result similar to Marsh's, but modified by a somewhat different reflection coefficient. This modified reflection coefficient, R, is nearly equal to Rayleigh's reflection coefficient at normal incidence, but differs considerably at shallow grazing angles. He lists the following definition for his modified reflection coefficient:

$$R = \Re + 2\frac{1-\gamma^2}{\gamma^2}\frac{\rho_2}{\rho_1}\left(\frac{\rho_2}{\rho_1}-1\right)\left[\frac{\rho_2}{\rho_1}+\frac{k_2}{k_1\gamma}f(\gamma)\right]^{-2} \qquad (2.7)$$

where $\Re$ is the Rayleigh reflection coefficient; ρ_1,ρ_2,k_1,k_2 are the densities and wavenumber magnitudes in media "1" and "2" respectively; γ is the cosine of the angle of incidence; and $f(\gamma) = (1-(k_1/k_2)^2(1-\gamma^2))^{1/2}$.

Before continuing, it is necessary to define the term "backscattering coefficient", denoted σ_s. This is a dimensionless expression which quantifies the efficiency with which a rough interface scatters energy back in the direction of the source of the energy. It is defined as:

$$\sigma_s = I_s r^2/I_0 A \qquad (2.8)$$

where I_0 is the intensity of the pressure wave incident on the interface; I_s is the intensity of the backscattered wave measured a distance 'r' from the interface and 'A' is the area of the insonified part of the interface. Kuo obtained an expression for the backscattering coefficient of:

$$\sigma_s = 4\cdot(k_1\gamma_1)^4\cdot\varphi(K)\cdot RR^* \qquad (2.9)$$

where $\varphi(K)$ is the roughness spectrum of the two-dimensional surface in wavenumber space. Kuo argues that non-specular scattering is selective. That is, scattering from the rough surface occurs only in the vicinity of the wavenumber, $K=k_i-k_s$. Here k_i is the horizontal component of the incident wave wavenumber, and

k_s is the horizontal component of the scattered wave wavenumber. For backscatter, $K=2k_i$.

Using data collected in a laboratory experiment by Nolle et alia[8], Kuo utilized Equation (2.9) to estimate the roughness spectra of Nolle et alia's sand surface. Kuo also examined data collected by Urick and Saling[24] in an ocean experiment in which acoustic energy was backscattered from the ocean bottom. For this data too, he obtained an estimate of the roughness spectra of the scattering surface. It is interesting to note that Nolle attributes the backscatter observed in his experiments to inhomogeneities within the scattering volume, not roughness effects.

Kuo[25] has since extended his model to include the effect of variations in the bottom surface density. He uses the model to explain qualitatively, experimental results obtained by Roderick and Dullea[26] in which bottom surface density fluctuations resulted from Sand Dollar activity.

Recently, Jackson et alia[27] presented rather convincing evidence that the validity of the RR method extends beyond the constraints of Equation (2.3). They base their argument on the equivalence (at least to 5th order) of terms obtained applying the RR method with those obtained from the extinction theorem; a much more rigorous perturbation method. They admit that the reason(s) for the extended validity is not yet clear. Nonetheless, the RR method is still only valid for rough interfaces with small gradients and small surface heights, even if the limitations are less restrictive than implied in Equation (2.3). We shall now examine the method used when these criteria are not met.

2.2.2 The Helmholtz Integral With Kirchhoff Boundary Condition

An alternative approach (to the RR method) to solve for the field scattered from a randomly rough interface is to use the Helmholtz integral. This equates the scattered field to the sum of contributions from an infinite number of point sources (or Huygen's wavelets) located on the boundary. The integral is given by:

$$p_s(R) = \frac{1}{4\pi}\iint_S \left[\frac{\partial p_s}{\partial n}\left(\frac{e^{ikr}}{r}\right) - p_s\frac{\partial}{\partial n}\left(\frac{e^{ikr}}{r}\right)\right] dS \qquad (2.10)$$

where p_s is the scattered pressure and n is the inward pointing surface normal. As can be seen from the integral, the scattered field is given in terms of the scattered pressure on the boundary and its derivative with respect to the surface normal.

Eckart[2] used this equation to examine the case of acoustic waves originating underwater, incident on a randomly rough ocean surface. This case approximates a pressure release interface for which we have the boundary condition:

$$p_s + p_0 = 0 \qquad (2.11)$$

where p_0 is the incident wave. This can be substituted into Equation (2.10) above. But as Eckart pointed out, "it is not so easy to obtain a good approximation for the normal derivative" of the scattered pressure on the boundary. To do this, he noted that if the surface was a plane, one would have:

$$\frac{\partial p_s}{\partial n} = \frac{\partial p_0}{\partial n}. \qquad (2.12)$$

Eckart observed that for an interface that had gentle undulations Equation (2.12) would be a reasonable approximation. This is the so-called Kirchhoff approximation. In this way he equated the scattered pressure at any point (in the half-space bounded by the ocean surface) to an integral containing pressure terms which involved only the incident field. Using Equation (2.10), Eckart developed an expression for the pressure field scattered from a randomly rough pressure release interface.

Eckart derives expressions for the scattered pressure for two limiting cases. First, if the wavelength of the incident radiation is much larger than the rms surface roughness he obtained:

$$\sigma_s = (k^2c^2/4\pi)^2 \cdot S(ka,kb) \qquad (2.13)$$

where k is the magnitude of the acoustic wavenumber and S(ka,kb) is the wavenumber spectrum of the surface waves. ('a' is the sum of the x direction cosines of the vectors pointing from source to scattering patch and scattering patch to receiver; 'b' and 'c' are the corresponding sums for the y and z direction cosines.) If the wavelength of the incident radiation is much smaller than the rms surface roughness he obtained:

$$\sigma_s = (1/8\pi\alpha\beta) \cdot \exp\{-.5[(a/\alpha c)^2 + (b/\beta c)^2]\} \qquad (2.14)$$

where α, β are the rms surface slopes in the x,y directions respectively.

From these expressions Eckart notes that long wavelength sound at various grazing angles can be used to estimate the surface roughness. Short wavelength sound, on the other hand, yields much less information about the surface spectrum. This is rather interesting because as he points out "this is almost the reverse of the situation encountered in atomic and molecular physics, where the scattering of radiation whose wavelength is less than the dimensions of the scattering structure yielded much more information than did the longer waves." Although Eckart modelled scattering from the surface of the ocean, one can apply these results to the ocean bottom simply by removing the time dependence from the equations.

It should be mentioned that Mintzer[28] showed that the boundary condition defined by Equation (2.12) is at best an approximation for smooth surfaces. The physical reason for this is that once p_s is defined on the boundary (as it has been in Equation (2.11)) dp_s/dn cannot be defined independently. Meecham[29] later showed that the Kirchhoff approximation is valid only if the local radius of curvature is much larger than the wavelength of the incident radiation. McDaniel and Gorman[30], express the limitation of the validity of the Kirchhoff approximation as:

$$2\cdot(kr_c\sin^3(\varphi_g))^{-1} < 1 \qquad (2.15)$$

where k is the incident wave wavenumber, r_c is the local radius of curvature of the surface, and φ_g is the grazing angle.

Clay[31] modified Eckart's theory to include an omni-directional acoustic source by subdividing the surface into rectangles within which the Eckart theory could be applied.

Beckmann and Spizzichino[32] improved on Eckart's application of the Kirchhoff approximation by modifying the boundary condition given by Equation (2.12). Their scattering theory was developed for electromagnetic waves. They equated the scattered electric field and the normal derivative of the scattered field to the values one would obtain on a plane tangent to the surface at any point. They express the limitation on the validity of the Kirchhoff approximation in two conditions; Equation (2.15) and the following:

$$2kr_c\sin(\varphi_1) >> 1 \qquad (2.15a)$$

where φ_1 is the local grazing angle. (The local grazing angle is the angle between the tangent plane to the surface and the incident wave.) Bass and Fuks[33] demonstrate that the conditions given by Equations (2.15, 2.15a) are in fact related. More importantly, they point out that it isn't possible to accurately determine the limits of validity of the Kirchhoff approximation. Jackson et alia[34] express the difficultly of defining the exact region of validity of the Kirchhoff approximation by stating "The condition on (surface) curvature is not as ... definite as one would like, owing to the extreme difficulty of estimating errors resulting from the various assumptions".

Clay and Medwin[35] follow the Eckart development fairly closely but modify the boundary condition of Equation (2.12) as did Beckmann and Spizzichino. Clay and Medwin expand Eckart's

explanation somewhat, providing a useful tutorial on the Helmholtz integral with the Kirchhoff approximation. They express the boundary condition given by Equation (2.12) as:

$$\frac{\partial p_s}{\partial n} = \mathcal{R}\frac{\partial p_o}{\partial n} \qquad (2.16)$$

where '$\mathcal{R}$' is the Rayleigh reflection coefficient.

Introducing the reflection coefficient into the integral further complicates its evaluation. To simplify things, they approximate $\mathcal{R}$ to a constant and remove it from inside the integral. They state that "this approximation is best near vertical incidence and may be poor at shallow grazing angles."

Thorne and Pace[36], follow the Clay and Medwin[35] approach in applying Eckart's theory to a gravel surface to study normal incidence backscatter in a laboratory experiment. They used a parametric array for the acoustic source. The Fresnel, rather than the usual Fraunhofer approximation was used to examine the frequency dependence of backscattering for several receiver-to-surface separations. They obtained better agreement between theory and experiment when the Fresnel approximation was used, especially for small receiver-to-surface separations, not surprisingly.

Pace et alia[37] extended this work to look critically at the normal incidence backscattered pressure as a function of receiver range from the surface. They concluded that in the far field the expression for the backscattering coefficient reduces to:

$$\sigma_{sff} = \frac{\mathfrak{R}^2}{4\pi S^2} \tag{2.17}$$

where $\mathfrak{R}$ is the Rayleigh reflection coefficient and S is the mean square surface slope. Note that Equation (2.17) is a function only of the surface slope. In the near field the backscattering coefficient reduces to:

$$\sigma_{snf} = \left(\frac{\mathfrak{R}^2}{A}\right)\left[\frac{R_1 R_0}{R_1 + R_0}\right]^2 \tag{2.18}$$

where 'A' is the area of the insonified patch, R_0 is the source to patch separation, and R_1 is the receiver to patch separation. In this case the average backscattered intensity is that expected from a plane surface with reflection coefficient $\mathfrak{R}$.

Al-Hamdani [38], followed Clay and Medwin's development of the Helmholtz integral and solved it for the case of a rough surface with gaussian statistics and a side scan sonar acoustic source with a gaussian beam pattern. He examined backscatter data as a function of grazing angles down to 30°. The experimental data matches his theoretical work quite well. However, Al-Hamdani noted the following shortcoming in his experiments. Three surfaces of various roughness were examined. The interface backscattering coefficient is actually a function of the surface slope, S, defined as: $S=(2h/T)^{1/2}$, where h is the rms height and T is the autocorrelation length of the surface. It occured that for his three surfaces, S remained approximately constant at about 0.7. The result is that the model wasn't tested

as rigorously as it might have been for successively smaller surface slopes.

Kuperman[39] employs a perturbation method developed by Bass[40] to examine specular reflection from a rough sea surface. The method involves replacing the usual boundary conditions of continuity of pressure, and continuity of the normal derivative of velocity given by:

$$\rho_1 u_1 = \rho_2 u_2 \; ; \; \frac{\partial u_1}{\partial n} = \frac{\partial u_2}{\partial n} \tag{2.19}$$

with a set of perturbed boundary conditions:

$$\rho_1 u_1(z)\Big|_{z=z_0} = \rho_2 u_2(z)\Big|_{z=z_0} \; ; \; \frac{\partial}{\partial n}\Big(u_1(z)\Big)\Big|_{z=z_0} = \frac{\partial}{\partial n}\Big(u_2(z)\Big)\Big|_{z=z_0} . \tag{2.20}$$

In the above expressions ρ_1, ρ_2, u_1, u_2 are the densities and velocity potentials in media "1" and "2' respectively. The surface is described by $z=z(x,y)$ where $z=z_0$ represents the boundary.

Kuperman derives the boundary conditions without assuming any local reflection law, so that the method isn't limited by the Kirchhoff approximation. He shows that his results reduce to the Kichhoff approximation in the appropriate limit. The drawback to Kuperman's method is the increased mathematical complexity involved.

There are few instances in which either the RR method or the Helmholtz integral with Kirchhoff approximation holds completely. We now turn our attention to a compromise of these two approximations.

2.2.3 The Composite Roughness (CR) Model

The composite roughness (henceforth CR) method was developed to treat surfaces with more than one roughness scale. Use of the method assumes that the surface can be decomposed into a large scale surface for which the Helmholtz integral with Kirchhoff approximation holds, and a small scale surface for which the RR method is valid.

In 1963, Kur'yanov[41] developed a model for the CR method. He noted that "the complete resultant wave is not, generally speaking, the sum of effects of the scattering at large and small irregularities on the surface". He solved the problem for the case of backscatter from a surface comprised of periodic small scale roughness coupled with, in one case periodic large scale roughness, and in a second case, a randomly rough large scale surface.

Bachmann[42] developed a CR model for backscatter from the ocean surface. He extended Marsh's[3] method of dealing with a small scale randomly rough surface, to include large scale random roughness. Bachmann improved upon Marsh's model by accounting for local changes in grazing angle due to the large scale roughness. He interpreted these changes in local grazing angle as being analogous to "carrier waves modulating the local grazing angle". The large scale roughness which concerned him resulted from ocean swell.

As McDaniels and Gorman[30] pointed out, both CR models discussed above, were derived heuristically. McDaniels and Gorman developed a rigorous derivation of the CR theory which enabled them to estimate contributions from neglected terms.

They expressed the constraints on applying the CR theory as "the wavenumber spectrum of the surface (roughness) must decay sufficiently fast with increasing wavenumber that a large scale surface may be defined on which the Kirchhoff approximation holds and a small scale surface defined for which the RR approximation is applicable".

They developed the model for a pressure release surface and evaluated it for the simplified case of backscatter. They compared the model to backscatter data obtained experimentally at 3kHz and 20 kHz. The model and experimental data agreed at 3kHz but not for 20kHz. Upon re-examining the model and, in particular, examining the contribution from neglected terms, McDaniels and Gorman concluded that the model is in fact valid and the disagreement between model and experimental data at 20kHz is likely a result of other scattering mechanisms.

2.3 Self-Shadowing Effects

If one deals with a sufficiently rough surface or interests lie in the region of shallow grazing angles, one must account for self-shadowing effects. Self-shadowing occurs when part of a surface acts to shield another part from the incident radiation. This can best be explained with the aid of a diagram. See Figure (2.1) for an example.

Eckart[2] refers briefly to the question of shadowing but merely states that his boundary conditions

$$\frac{\partial p_s}{\partial n} = \frac{\partial p_o}{\partial n} \qquad (2.21)$$

might more appropriately be modified to

$$\frac{\partial p_s}{\partial n} = -\frac{\partial p_o}{\partial n} \qquad (2.22)$$

in regions of deep shadow.

Horton et alia[4] applied Eckart's scattering model to experimental data collected in a laboratory environment. They found that agreement between theory and experiment was poor until they modified Eckart's boundary condition to

$$\frac{\partial p_s}{\partial n} = 0 . \qquad (2.23)$$

This, they felt represented an effective compromise between no shadowing and deep shadowing for their randomly rough surface. For justification they pointed to the excellent agreement between Eckart's theory (modified by their boundary condition of Equation (2.23)) and experiment.

Beckmann[43] examined the question of shadowing directly. He introduced a shadowing function S, a probability that a point on the surface z=f(x) will be illuminated by the incident radiation. The probability that a point on the surface is shadowed depends on both its height and slope. These two parameters are related but Beckmann treated them as independent to simplify the ensuing mathematics.

Wagner[44] followed Beckmann's definition of the shadowing function but maintained the dependence of the height and surface slope at a point. His results differed from Beckmann's but agreed with a computer simulation of the shadowing function carried out by Brockelman and Hagfors[45]. Further verification of

Wagner's results came from Smith[46] who used a simplified method to evaluate the shadowing function defined by Wagner. Smith's results were in close agreement with Wagner's.

Bachmann[42] employed Smith's shadowing function to account for shadowing effects in his composite roughness model discussed earlier. Bachmann compares this model with a small sample of experimental data taken at sea and the agreement is good, experimental errors considered.

2.4 Scattering By Inhomogeneities Within the Seabed

Thus far, boundary scattering has been assumed to result strictly from interface roughness. While this assumption may be considered accurate in the case of the sea surface, (in the absence of a bubble layer) there is increasing evidence that it is not always valid for scattering from the ocean bottom.

Stockhausen[7], as early as 1963, derived an expression for the intensity of a sound wave backscattered from the volume of the ocean bottom. In his model, he assumes a spherically spreading acoustic pulse of time width τ, is incident on the water/bottom interface. Part of the energy is refracted into the bottom volume. The model assumes that the bottom is composed of solid spherical particles which act to scatter the acoustic energy. The intensity of the backscattered wave, I_s, is given by:

$$\delta I_s(t,\tau) = I_0(\tau)H_1Z_1\eta_1H_2Z_2\eta_2\sigma_v\delta V \qquad (2.24)$$

where I_0 represents the intensity of the source pulse measured at unit distance; H_1 and H_2, represent the geometrical spreading from source to volume and volume to receiver respectively; Z_1 and Z_2 represent the mismatch loss factors at the interface for

ingoing and outgoing waves respectively; η_1 and η_2 represent attenuation factors due to absorption and scattering within the bottom, for ingoing and outgoing waves respectively; σ_v represents the bottom volume backscattering coefficient and is defined in analogy with the surface backscattering coefficient, σ_s, defined in Equation (2.8).

$$I_s = I_0 \sigma_v \delta V / r^2 . \qquad (2.25)$$

Stockhausen employes geometrical arguments to account for H_1 and H_2, Rayleigh's reflection coefficient to account for Z_1 and Z_2, and experimental data [47] to account for η_1 and η_2. He uses equations from Morse[48] to calculate the volume backscattering coefficient given by:

$$\sigma_v = \frac{64\pi^3 a^3 f^4 (1-P)}{3c_2^4} \qquad (2.26)$$

where 'a' is the particle radius, c_2 is the sound speed in medium '2' and P is the porosity.

Nolle et alia[8] have also derived a volume scattering model. However, they considered the volume backscattering coefficient, σ_v, to consist of an "average scattering amplitude factor per unit volume" similar to Stockhausen, and a term "δ" to account for local deviations in the scattering strength of individual scattering centres. Altering the notation of <u>their</u> Equation (12) to our notation, we write:

$$\sigma_v(x,y,z) = \sigma_{v0}(1+\delta(x,y,z)) \qquad (2.27)$$

where σ_{v0} is the average scattering strength.

Treating the deviations as random, and centred about a mean volume scattering strength, they defined an autocorrelation function for the scattering strength. With no justification other than simplifying the ensuing mathematics, they assumed a form for the scattering autocorrelation of an exponential decay. (They based this form on experimental work by Liebermann on the autocorrelation function of temperature fluctuations in the ocean.) Nolle et alia then derive an expression for the intensity of a backscattered wave assuming a plane wave incident on the bottom volume.

Nolle et alia compared their model to laboratory data they collected by scattering acoustic waves from a smooth sand surface. It occured that the correlation length only appeared in the amplitude term of their model, not in the frequency or grazing angle dependence. Since they had no way of knowing the length scale of their autocorrelation function, they examined frequency and grazing angle dependence, but not absolute levels. They note that "The observed and calculated results agree as to the presence of a region where the backward-scattering coefficient is nearly independent of angle, and in the decrease of the coefficient as the grazing angle is reduced below the critical angle. The decrease observed experimentally was never as rapid as that predicted by the theory, however." They offer a few explanations for the discrepancy between experiment and theory but interestingly, none related to surface roughness effects; this in spite of the fact that earlier in the paper they note that "a

complete analysis should include a suitably weighted combination of a volume scattering model...with a surface scattering model."

Crowther[9] combined roughness and volume effects in his model of backscattering from the ocean bottom. He employed Kuo's[23] model discussed earlier, for scattering from a randomly rough surface and assumed a roughness spectrum similar to those obtained for the ocean surface. (He offered no justification for this choice of spectrum.) He assumed a flat, two fluid interface at the boundary. Due to space limitations in the paper, he merely quotes his expression for the volume backscattering coefficient, M_{BV}. Crowther defines M_{BV}, as the mean target strength per unit volume.

$$M_{BV} = \frac{\lambda^2 |T\,T^*|^2 \cdot T_{12}(2k')}{4 \cdot \Im m\{\tau\}} \qquad (2.28)$$

where TT* is the two way transmission into and out of the sea bed; $T_{12}(2k')$ is the local scattering in the sea bed due to fluctuations in the correlation function of the impedance of the sea bed; and τ is the magnitude of the vertical component of the wavenumber in the sea bed. To solve for $T_{12}(2k')$, one must know the correlation function of the sea bed. He assumes an elliptical exponential. Note that in Crowther's expression for the volume backscattering coefficient, M_{BV}, he includes the effects of transmission to and from the scattering volume. This is in contrast with Stockhausen[7] and Nolle et alia[8] who account for these terms separately. For them, the volume backscattering coefficient, merely represents the scattering of the acoustic wave by a unit of volume within the bottom.

Crowther compares his model to the Nolle et alia laboratory backscatter data, and sea data collected by various authors [49,50,51]. Crowther assumes a correlation length of the order of the particle radius to compare his model to Nolle's data. For this case his ellipsoidal correlation coefficient is spherical. He concludes that agreement is as good as can be expected in light of the uncertainty in the correlation coefficient. Crowther's model predicts too rapid a decrease in the backscattering coefficient. (Recall that Nolle et alia encountered a similar disagreement between theory and data. Also, as with Nolle et alia, Crowther chose not to estimate the interface roughness scattering contribution, although he does estimate it for the sea data discussed next.)

The sea data collected [49,50,51], ranged in frequency from 1 to 6 kHz. The bottom type in the region was soft. From core samples taken in the area where the sea data was gathered, Crowther estimated the vertical length scale for the correlation coefficient. Estimating the horizontal correlation coefficient was more difficult so he merely tried several guesses to obtain agreement between the model and the data. He plotted curves of Kuo's interface roughness model as well as the volume scattering model and compared them to the sea data. From the comparison, it appeared that volume scattering would likely dominate in regions of soft bottom sediment.

Wyber[52] examines the question of bottom volume backscattering from a signal processing point of view. He too, considers the case of non-zero correlation between scatterers. He points out that the assumption employed in the classical sonar

equation, i.e. that one can form an incoherent sum over scatterers within a given region, is equivalent to assuming the correlation function varies rapidly compared to the pulse length.

Ivakin and Lysanov[10] attempt to account for the lack of frequency dependence for bottom backscatter, particularly in coastal waters, in the range 1-100kHz, via a volume backscattering model[1]. They take as their starting point, an expression for the coefficient of backscattering from an absorbing layer with random inhomogeneities, from Volovov and Zhitkovskii[53]. Ivakin and Lysanov denote the coefficient m_s (equivalent to σ_s in Equation (2.8)) and write

$$m_s = (2\beta)^{-1} m_v \sin(\varphi_g) \tag{2.29}$$

where β is the sound absorption coefficient of the bottom, φ_g is the grazing angle and m_v is the volume scattering coefficient of the bottom, equivalent to σ_v in Equation (2.25). Chernov[11] gives the following expression for m_v if the linear dimensions of the scattering volume are large compared to the inhomogeneity space scale:

$$m_v = 2\pi k^4 G(q) \tag{2.30}$$

---

[1] Ivakin and Lysanov cite data from Zhitkovskii[56], and Volovov and Zhitkovskii[53] to back this statement. Several Western papers indicate a weak frequency dependence for backscatter from the sea bed. See the discussion on experimental data in section 2.5 for examples.

where k is the magnitude of the acoustic wavenumber. (Ivakin and Lysanov assumed that the change in density and sound speed is minimal from water to water-saturated sediment so that k is the same in both media. This also results in no critical angle.) The three-dimensional vector $q=k_i-k_s$, where k_i,k_s are the wave-numbers of the incident and scattered waves, respectively. For backscatter, $q=2k_i$. They define G(q), the power spectrum of the inhomogeneities, as the Fourier transform of the refractive index fluctuations in the sediment. This is similar to the volume scattering models of Nolle et alia[8] and Crowther[9] in that scattering is assumed to result from variations in the acoustic impedance of the sea bed.

The paper involves deriving a general form for G(q), which makes m_s independent of frequency. This implies that G(q) is proportional to k^{-3} since β is proportional to k^{-1}[54]. Ivakin and Lysanov examine the refractive index fluctuations in the sea bed in terms of its vertical and horizontal components. They assume that the length scale of the vertical component, z_1 is much less than the horizontal component, r_1. (This corresponds to a sedimentation model for the seabed for which evidence exists, particularly in coastal waters. See Reference [55].) With the vertical correlation length chosen sufficiently short, the vertical component of G(q) is a constant. Assuming a horizontally isotropic correlation function in the form of an exponential decay, they obtain the expression:

$$m_s \approx \langle\mu\rangle^2 \cdot \frac{(k/\beta)(z_1/r_1)}{16\pi\cos^3(\varphi_g)} \cdot \sin(\varphi_g) \qquad (2.31)$$

where $\langle\mu\rangle^2$ is the mean square value of the refractive index fluctuations. They compare averaged data taken from Bunchuk and Zhitkovski[57] to the model, inserting typical values for the sound absorption coefficient, and mean square value of the correlation. The model and data are plotted as a function of grazing angle and the agreement is excellent. Note however, that the ratio of the vertical to horizontal correlation length was left as a free parameter in order to match the model to the absolute level of the experimental data. Finally, they prove that any horizontal correlation coefficient which has a nonvanishing first derivative for r=0, where r=(x,y), will result in G(q) being proportional to k^{-3}. This includes exponential decay types, for example.

In a second paper by Ivakin and Lysanov[58], published a few months later, they revise the model to account for the effect that a rough interface has on the expression for m_s. They also allow for different densities and sound speeds in the two media. They begin with the Helmholtz equation given as:

$$\Delta p(R) + [k_0 n(R)]^2 p(R) = 0 \qquad (2.32)$$

where k_0 is the magnitude of the sound speed wavenumber, R=(x,y,z), and n(R) is the refractive index (n(R)=1 in the water). To account for random changes in the refractive index, n(R) is written as:

$$n(R) = n_0(1 + \mu(R)), \quad \mu(R) = (n-n_0)/n_0 \ . \qquad (2.33)$$

The pressure is broken into a component, p_0, present if μ was everywhere zero and a scattered component, p_s, due to the refractive index fluctuations. Green's functions are used to solve for p_s, and an expression for m_s is obtained:

$$m_s \approx \left[\frac{2(\rho_1/\rho_0)}{(\rho_1/\rho_0)+n_0}\right]^4 \cdot \left(\frac{g_0(\varphi_g)}{(\rho_1/\rho_0)^2}\right) \cdot \left(\frac{2\pi k^4 G(q)}{2\beta}\right) \qquad (2.34)$$

The function $g_0(\varphi_g)$ approaches unity for grazing angles greater than critical and for angles less than critical it approaches 0. It approaches 0 more slowly for rough interfaces than smooth interfaces, as rough interfaces enhance penetration of sound into the bottom. If the densities of both media are the same (i.e. $\rho_0=\rho_1$) and the index of refraction of both media are the same, Equation (2.34) reduces to Equation (2.31) with $g_0(\varphi_g)$ replacing $\sin(\varphi_g)$ to account for surface roughness.

In Reference [59], Ivakin and Lysanov indicate the low frequency (0.8-4kHz), small grazing angle (1.5°-8°) dependence of their volume backscatter model derived primarily in [10] and [58]. The model contained in [59] is given by:

$$m_v \approx A \cdot \left|\frac{W(\varphi_g)}{W(\pi/2)}\right|^4 \frac{h_{eff}(\varphi_g)}{h_{eff}(\pi/2)} \cdot (2k_0 a)^3 (1+(2k_0 a)^2)^{-3/2} \qquad (2.35)$$

where W is the (complex) pressure coefficient of sound transmission from the water into the bottom, 'A' is a nondimensional constant, 'a' is the length scale of the inhomogeneity fluctuations, and h_{eff} is the effective thickness of the bottom layer which is a function of grazing angle and bottom

attenuation. Equation (2.35) is frequency independent for ka >> 1, so that for ka << 1 the model goes like f^3. At low grazing, the model predicts a sharp decrease in backscatter resulting from the $|W|^4$.

There is some confusion in their work, however, since they assume that the inhomogeneities are isotropic but at the same time choose a "power coefficient ... so that the scattering coefficient will be independent of frequency at sufficiently high frequencies". The confusion arises because the power coefficient "-3/2" is typical of inhomogeneities, isotropic in two dimensions, not three. Recall, from References [10] and [58], the model was based on two-dimensional inhomogenieties in the horizontal plane. Nor does it appear that they actually *mean* two-dimensional isotropicity in their present paper, since they state that G(q)=G(q)=G(2k) which implies three-dimensional isotropicity. (For the two-dimensional isotropic case we have for backscatter, $G(q)=G(k_r,k_z)=G(2k\cos\varphi_g,2k\sin\varphi_g)$.)

In Reference [60], Ivakin extends the model for scattering from inhomogeneities within the ocean bottom, to account for stratification of the bottom. Previously, the model accounted only for small perturbations in the acoustic parameters of the bottom (density, sound speed and absorption coefficient), from their mean values, which otherwise, were considered to remain constant with depth. Now he examines the effect of stratified layers with considerably different properties from one another. In particular, he considers the cases of a linear growth in sound velocity with depth and a linear decrease in sound velocity with depth. In both cases, the following result immerges. For $\sin^2(\varphi_g)$

$<< (n^2-1)/(m^2+1)$, the backscattering coefficient is proportional to $\sin(\varphi_g)$, the so-called Lommel-Seeliger law. (Here n is the refractive index at the water/bottom interface and m is the density ratio at the water/bottom interface.) For $\sin(\varphi_g) > (n^2-1)^{1/2}$, the backscattering coefficient is proportional to $\sin^2(\varphi_g)$, Lambert's law.

Recently, Jackson et alia[34] published a paper which combines several of the models in this review to estimate backscattering as a function of grazing angle for frequencies of 30 and 35kHz. Using heuristic arguments, they extend McDaniel and Gorman's composite roughness model to include the case of a penetrable, two-fluid boundary. They assume a Gaussian, isotropic wavenumber spectrum of the bottom roughness, W, of the form:

$$W(\mathbf{k}) = Bk^{-g} \qquad (2.36)$$

where k is the two-dimensional, horizontal wavenumber, g is a constant (thought to be in the range of 3 to 3.5) and B is a constant. They employ Kuo's[23] expression for the small scale roughness scattering and the Helmholtz integral with the Kirchhoff approximation for the large scale roughness effects. This model is valid for grazing angles less than 70°. For grazing angles greater than 70°, certain approximations break down and it becomes necessary to use the Helmholtz integral with Kirchhoff approximation alone. Wagner's shadowing function is also included in the model.

To account for any volume scattering contribution, Jackson et alia use the expression Stockhausen[7] derived for the

effective surface scattering coefficient due to volume scattering. Jackson et alia insert this term into their composite roughness model as an independent source of backscatter.

Jackson et alia compare their total model to experimental data gathered at two ocean sites. The experimental data is plotted along with the interface scattering model. They then adjust a free parameter in the volume scattering component of the model to provide the best agreement between experiment and model. This free parameter is related to the attenuation of the sound wave in the sediment due to both scattering and absorption. Stockhausen's model does provide expressions to evaluate this term but physical parameters such as the frequency dependence of the absorption coefficient must be known. The agreement between the total model and the experimental data is quite good. Also, the matching of the two interface scattering models in the vicinity of 70° grazing is within 3 dB.

Inherent in Jackson et alia's approach is the assumption that any correlation between volume and roughness contributions to scattering is neglected. In defence of this assumption, they comment that "This is reasonable, since the volume scatterers are distributed over distances considerably greater than the acoustic wavelength, which should randomize the phase between interface and volume fields." While the actual contribution of volume and interface scattering components may be independent, they neglect the possibility that the shape of the boundary can affect the volume scattering term. (Recall the term, $g_0(\varphi_g)$ from Ivakin & Lysanov[58].)

2.5 Experimental Data of Acoustic Scattering

Theoretical models of scatter from the ocean surface can be applied to the ocean bottom by removing the time dependence of the surface and altering the statistics of the surface appropriately. For this reason, models developed to explain interface scattering for both the ocean surface and bottom have been discussed in this review. Experimental data, however, depend directly on the statistics of the rough interface from which the wave has been scattered. For this reason, only data collected for scattering from rough bottoms (either in the lab or at sea) are reviewed in this chapter.

LaCasce and Tamarkin[6] performed experiments on three sinusoidally rough, pressure release surfaces of different roughness. They compared their results to the models of Eckart[2], Brekhovskikh[61] and Rayleigh[12]. The best agreement was obtained for the surface of slightest roughness. The experiment consisted of measuring acoustic wave scattering as a function of angle and frequency. Both the angle of incidence and the angle at which the scattered wave was measured were varied. Their data has been used by several other scientists ([13], [62], [63]) to verify the validity of their own models. Fortuin[64] compares the results of the LaCasce and Tamarkin paper, including the models of Eckart, Brekhovskikh and Rayleigh, to the models of Heaps[65], Jordan[63], Uretsky[13], Parker[62], and Meecham[66]. It should also be mentioned, that the paper by Fortuin provides an excellent review of the literature available on acoustic scattering from the ocean surface up until 1969.

In 1961, Mackenzie[67] presented measurements of backscatter from the deep ocean bottom. The data were taken at frequencies of 530 and 1030Hz. The data follow a $\sin(\varphi_g)$ to $\sin^2(\varphi_g)$ dependence, where φ_g is the grazing angle. It is interesting to note that MacKenzie claims this grazing angle dependence from 30° to 90°, whereas most authors only note this type of dependence for grazing angles less than about 50°.

Urick and Saling[24] measured backscattered levels off the North American Continental rise. They employed explosive charges as the sound source so as to provide a nearly omnidirectional signal with a wide frequency bandwidth. Data analysed in the octave bands 500Hz to 1000Hz and 4kHz to 8kHz were plotted vs. grazing angle for angles of 30° to 90°. The data followed a $\sin^2(\varphi_g)$ dependence from about 30° to 50°. For steeper grazing angles the data rose more rapidly. In fact, the data fit the grazing angle dependence of Ivakin and Lysanov[10] outlined earlier.

Patterson[68] presented acoustic backscatter data obtained from the deep ocean bottom. He used a 2.5kHz tone burst for the acoustic source. His data show a marked peak in the vicinity of 30° grazing. The peak is similar to the peak in curves presented in Jackson et alia[34] discussed earlier, in which Jackson used Kuo's[23] model for scattering from a rough interface. (See Figure 2 of Reference [34].) Employing heuristic arguments, Patterson developed an empirical model to estimate backscatter levels. His expression for the model is:

$$S_\varphi = 10\log(A(B+C)) \qquad (2.37)$$

where 'A' is the Rayleigh reflection coefficient, 'B' is a constant times "some sort of random probability density function" and 'C' is a constant times the sine of the grazing angle raised to some power.

McKinney and Anderson[69] collected acoustic backscatter data from the ocean bottom at 16 shallow water locations along the U.S. coast. The data were classed according to roughness type; mud, clay, sand, or gravel. They plotted the data as a function of both frequency and grazing angle. They varied the frequency from 13 to 300kHz and the grazing angle from 2° to about 80°. A frequency dependence of $f^{1.6}$ was evident for sandy bottoms but no discernable frequency dependence for the other bottom types was noted. The dependence of backscatter level on grazing angle varied from $\sin(\varphi_g)$ to $\sin^2(\varphi_g)$ depending on the bottom type, for grazing angles up to about 50°. For grazing angles steeper than 50°, the dependence on angle is not so clear cut. McKinney and Anderson's data have been used extensively by others to provide an experimental data base to check various acoustic backscattering models.

Merklinger[49] gathered backscatter data from five deep water locations in the North Atlantic using an explosive sound source. His data showed a $\sin^{1/2}(\varphi_g)$ to $\sin^2(\varphi_g)$ dependence on grazing angle over the five locations. He examined the frequency domain in seven, one octave bands, from 100Hz to 12.8kHz. He noted a frequency dependence which varied from $f^{.67}$ to $f^{1.1}$.

Buckley and Urick[50] performed an experiment similar to Merklinger's, independently, at three locations off the west coast of Bermuda in 16000 ft. waters. They too, used an explosive

source but examined data in the 2-4kHz band. The data followed a $\sin(\varphi_g)$ to $\sin^2(\varphi_g)$ in their case. It is interesting to note the following comment which they made upon examining the data: "there is a tendency for the rate of decrease (in backscattering level) to become less at low angles so as to suggest an admixture of scattered sound from the volume of the sea or from the volume of the sea bottom".

Wong and Chesterman[70] collected backscattering data in the shallow waters around Hong Kong. For a sound source they employed a 48kHz tone burst. They noted "a clear dependence of the backscattering coefficient on bottom type." The backscattering coefficient increased from its value for clay through sand to rock, indicating "that the particulate nature of the bottom is at least partly responsible for the backscattering." Within any one particle type grouping, no clear dependence was noted which suggested "that bottom roughness also plays an important role in the scattering mechanism." A useful feature of their paper is a comparison of backscatter data collected by various scientists which Wong and Chesterman group in terms of the particular bottom type.

Bunchuk and Zhitkovskii[57] present an overview of scattering in shallow water regions. They discuss the definition of the scattering coefficient and scattering strength as well as several of the experimental techniques employed to obtain scattering data from the sea bottom. A summary of the available data is provided and the dependence on frequency, grazing angle and bottom type of the data is given. They also point to the weakness of bottom roughness scattering models to fully

describe acoustic scattering, suggesting that contributions from the bottom volume may exist.

Boehme et alia[71] collected data at very shallow grazing (2°-10°) in experiments performed off the Pacific coast of the United States. They examined the frequency band, 30-95kHz. The data were analyzed to determine the dependence of bottom backscatter on frequency, grazing angle, bottom type, and beamwidth and type of transmit signal. Their results can be summarized as follows: The frequency dependence was in the range of $f^{1.0}$ to $f^{1.5}$. The data followed a Lamberts law dependence with respect to grazing angle. The measurements were independent of both transmit signal type and beamwidth. The dependence on bottom type was inconclusive.

Jackson et alia[72] present acoustic backscatter data obtained from several ocean sites. The sites included sand, silt and gravel. Their experiment improved on previous experiments of a similar type in that bottom parameters such as grain size, bottom density, compressional sound speed, and bottom roughness were categorized for each site. The overriding conclusions of the experiment remained consistent with previous work. That is: the backscattering coefficient increases with frequency only slightly in the range 20-85kHz. (1-2dB/octave on average.) The backscattering coefficient is generally smallest in silt/sand, and largest in gravel/rock bottoms. Within any one bottom type, variations of 10-15 dB in the backscattering coefficient can occur, indicating that bottom type alone is insufficient to determine backscattering strength.

In the following chapters we return to the focus of the present work as discussed in Chapter 1. To begin with, a mathematical model is derived for acoustic scattering from the volume beneath a water/sediment interface.

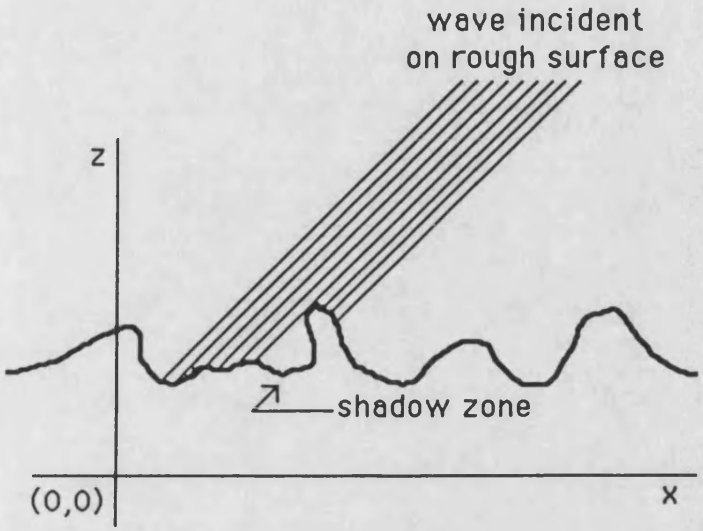

Figure (2.1): Schematic of a rough surface partially shadowing itself.

CHAPTER 3

THEORETICAL DEVELOPMENT OF ACOUSTIC SCATTERING MODEL

In the following chapter we derive a theoretical model for acoustic backscatter from the volume, below a water/bottom interface. We base the derivation on the propagation of a plane wave in an inhomogeneous medium. The theoretical development follows that of Chernov[11]. Complications arise because the source is located in the water so that one must consider the effect of the boundary (assumed smooth) on transmission. In the model, the individual "scattering centres" are not necessarily uncorrelated. Of particular interest then, is the dependence of scattering on the form of the correlation function. Following the general derivation, expressions for the backscattered intensity are obtained, for several forms of the correlation function.

3.1 The Wave Equation in an Inhomogeneous Medium

We shall take as our point of departure, the wave equation in an inhomogeneous medium. Numerous texts present its derivation. (cf. [11].) The equation can be written as:

$$\frac{1}{c^2(x,y,z)} \cdot \frac{\partial^2 p}{\partial t^2} - \nabla^2 p + \frac{\nabla \rho(x,y,z)}{\rho(x,y,z)} \cdot \nabla p = 0 \qquad (3.1)$$

where c is the acoustic wave speed, ρ is the medium density, and p the pressure. Note that in Equation (3.1), c and ρ are functions of position, hence the medium is inhomogeneous[1]. (Of

[1] In general, c and ρ may also be functions of time in an inhomogeneous medium. In this study, however, temporal inhomogeneities are so slowly varying as to be negligible.

course, the pressure is a function of time and space but is written simply as 'p', for the sake of brevity.)

No general solution exists for Equation (3.1), a second order partial differential equation with variable coefficients. In fact, it can only be solved exactly for a few special cases. However, if the parameters c and ρ deviate only slightly from their mean values, the method of small perturbations can be employed to obtain an approximate solution. This technique is examined now.

3.2 Application of the Method of Small Perturbations to Acoustic Scattering : A Review

Before attempting the problem at hand, it is instructive to review the method of small perturbations as it applies to the case of acoustic scattering. We begin by expressing the fluctuating parameters c and ρ as a Taylor expansion, retaining terms to first order.

$$c = c_0 + \Delta c(x,y,z); \quad \rho = \rho_0 + \Delta\rho(x,y,z) \tag{3.2}$$

where c_0, ρ_0 are the mean wave speed and density of the medium, and $\Delta c(x,y,z)$, $\Delta\rho(x,y,z)$ represent small fluctuations about the mean values. By small we mean

$$\Delta c(x,y,z) \ll c_0; \quad \Delta\rho(x,y,z) \ll \rho_0 . \tag{3.3}$$

Substituting Equation (3.2) into (3.1) we obtain:

$$\frac{1}{(c_0+\Delta c)^2}\frac{\partial^2 p}{\partial t^2} - \nabla^2 p + \frac{\nabla(\rho_0+\Delta\rho)}{(\rho_0+\Delta\rho)}\cdot\nabla p \tag{3.4}$$

where the notation (x,y,z) has been suppressed to ease writing. Expressing $(c_0+\Delta c)^2$ as a binomial expansion, retaining terms only to first order, and making the approximation $\rho_0+\Delta\rho \approx \rho$ in the denominator of the final term in Equation (3.4) results in:

$$\frac{1}{c_0^2}\cdot\frac{\partial^2 p}{\partial t^2} - \nabla^2 p = \frac{2\Delta c}{c_0^3}\cdot\frac{\partial^2 p}{\partial t^2} - \frac{\nabla(\Delta\rho)}{\rho_0}\cdot\nabla p \qquad (3.5)$$

Application of Equation (3.5) to the scattering problem proceeds as follows: We note that for small perturbations in c and ρ, the scattered wave will be much smaller in magnitude than the incident wave. Because the scattered wave is small, we neglect any reduction in magnitude of the incident wave due to scattering. Writing the total pressure as the sum of the incident pressure wave, p_i, and the scattered pressure wave, p_s:

$$p = p_i + p_s;\ p_i >> p_s \qquad (3.6)$$

and substituting Equation (3.6) into (3.5), we obtain:

$$\frac{1}{c_0^2}\cdot\frac{\partial^2 p_s}{\partial t^2} - \nabla^2 p_s \approx \frac{2\Delta c}{c_0^3}\cdot\frac{\partial^2 p_i}{\partial t^2} - \frac{1}{\rho_0}\nabla(\Delta\rho)\cdot\nabla p_i \qquad (3.7)$$

Equation (3.7) is a first order approximation for the scattered pressure, p_s, in terms of the incident pressure, p_i. It remains to solve this equation to obtain the scattered pressure. We now proceed to obtain an approximate solution to Equation (3.7) for the case of acoustic backscatter.

3.3 Backscatter of a Water-borne Plane Wave in Inhomogeneous Sediment

We seek a solution for the scattered pressure under the following conditions. A plane wave incident from water, refracts into an inhomogeneous bottom comprised of water-saturated sediment. The bottom is assumed fluid.[2] The inhomogeneities scatter the incident plane wave, thereby acting as point sources of spherical waves. The model developed assumes single scattering only. That is, the scattered waves generated by each point source are not scattered again as the waves propagate to the receiver.[3] Attenuation in the sediment is accounted for by making the acoustic wavenumber in the sediment complex. Throughout the text, vectors shall be depicted by an arrow overhead and complex numbers shall be in bold type; eg. $\vec{k}=(k_x,k_y,k_z)$ where $k_x=a+ib$, $k_y=c+id$, $k_z=e+if$. Here the complex vector $\vec{k}$ consists of components k_x,k_y,k_z each of which consist of a real and imaginary part.

We shall assume that the scattering volume, with dimensions of order L_v, and the receiver, located at a range R, obey the inequality $R>>L_v$. Furthermore, if L_c is the correlation length, then $L_v>>L_c$. The validity of these assumptions must, of course, be examined for a particular experiment.

---

[2] The term fluid implies that the bottom is incapable of supporting shear waves. The validity of the fluid bottom assumption is discussed in Appendix A.

[3] While it is unrealistic to assume that the waves would not be rescattered, it is reasonable to assume that second and higher order scattering may contribute a negligible amount to the total.

Figure (3.1) depicts the geometry for the backscatter problem. Because $R>>L_v$, the problem is represented in two dimensions and the axes oriented so that the waves propagate in the xz plane. (This is a far field approximation.) In the figure, a source located at M generates a plane wave with incident angle Θ_i, which refracts into the bottom at angle Θ_0. A spherical wave scatters from each insonified point P. Part of the scattered wavefront propagates back to the receiver, also located at M.

We express the incident wave p_i, at any point in the sediment as:

$$p_i = P_0 T_{ws} \cdot e^{ik_s(x_T \cdot \sin\Theta_0 + z_w \sqrt{n_{sw}^2 - \sin^2\Theta_0} - z_s \cos\Theta_0)} \cdot e^{i\omega t} \qquad (3.8)$$

where P_0 is the amplitude of the incident plane wave, T_{ws} is the pressure transmission coefficient for a plane wave incident from the water, k_s is the complex wave number in the sediment and $n_{sw}=k_w/k_s$. [4]

Substituting Equation (3.8) into (3.7) and differentiating the right hand side of the latter obtains:

$$\frac{1}{c_0}\frac{\partial^2 p_s}{\partial t^2} - \nabla^2 p_s = -\left[2\frac{\Delta c}{c_0}k_s^2 + \frac{ik_s}{\rho_0}\left\{\frac{\partial(\Delta\rho)}{\partial x}\sin\Theta_0 - \frac{\partial(\Delta\rho)}{\partial z}\cos\Theta_0\right\}\right]p_i \qquad (3.9)$$

---

[4] As both n_{sw} and its inverse, n_{ws}, occur frequently throughout the text, we avoid the term "refractive index" to prevent possible misunderstanding.

Next we note that Equation (3.9) is the wave equation with the right hand side representing a source term. With this in mind, we rewrite (3.9) as:

$$\frac{1}{c_0^2}\frac{\partial^2 p_s}{\partial t^2} - \nabla^2 p_s = 4\pi Q\delta(\vec{r}) \qquad (3.10)$$

where the notation '$4\pi Q\delta(\vec{r})$' signifies that each scatterer acts as an individual point source, and $\vec{r}$ is a vector drawn from the scattering point to the receiver. In this notation

$$Q = -\frac{1}{4\pi}\left[2\frac{\Delta c}{c_0}k_s^2 + \frac{ik_s}{\rho_0}\left\{\frac{\partial(\Delta\rho)}{\partial x}\sin\theta_0 - \frac{\partial(\Delta\rho)}{\partial z}\cos\theta_0\right\}\right]p_i \qquad (3.11)$$

The formal solution to Equation (3.10) may be obtained via an application of Green's functions. The result for the three-dimensional wave equation is well known however, and shall merely be quoted.

$$p_s = Q\cdot T\cdot\frac{e^{i\vec{k}\cdot\vec{r}}}{r}. \qquad (3.12)$$

Equation (3.12) states that each scatterer acts as a spherical point source with complex amplitude Q. The factor T accounts symbolically for the transmission of the spherical wave through the boundary. The total scattered pressure is the sum of all contributing point sources within the insonified volume. That is:

$$p_s = \int_V Q \cdot T \cdot \frac{e^{i\vec{k}\vec{r}}}{r} dV . \qquad (3.13)$$

Due to the geometry of the problem, i.e., a planar interface separating water and sediment, it is expedient to represent each scattered spherical wave as an integral over plane waves. A steepest descent integration can then be used to obtain an approximate solution in the form of plane waves scattered from each point. This reduces the complexity of Equation (3.13) as T can be replaced by T_{sw}, the pressure transmission coefficient for a plane wave incident from the sediment, a known quantity.

Appendix B contains a detailed discussion of the transmission of a spherical wave from the bottom to water through a planar interface, using the above procedure. Briefly, we approximate each scattered spherical wave by two plane wave components: a refracted wave and a lateral, or evenescent wave. As sketched in Figure (3.2), the refracted wave propagates along the usual Snell's path PQM to the receiver. The lateral wave propagates along the path PSM. (Note that the lateral wave only exists under the condition $\sin(|\beta|) > |1/n_{sw}|$.) These waves shall be denoted p_r and p_l, respectively and written:

$$T \cdot \frac{e^{i\vec{k}\vec{r}}}{r} \approx p_r + p_l . \qquad (3.14)$$

A straightfoward substitution of Equation (3.14) into (3.13) yields:

$$p_s = \int_V Q \cdot (p_r + p_l) dV . \qquad (3.15)$$

The backscattered intensity from a single point scatterer is given by pp^* (where '*' denotes the complex conjugate operation). The total backscattered intensity I_s, from the insonified volume will be the sum of $p_{si}p_{sj}$ over all pairs of scatterers i,j. (See Figure (3.3).) We write the total backscattered intensity in integral form as:

$$I \approx \int_{V_1}\int_{V_2} Q_1 Q_2^* \cdot (p_{r1} + p_{11}) \cdot (p_{r2} + p_{12})^* dV_1 dV_2 \ . \qquad (3.16)$$

The solution of Equation (3.16) is by no means trivial and any simplifications would be quite useful. To this end, we note that the phase of the lateral wave actually "begins" at the interface. Furthermore, recall that the correlation length is much less than the dimensions of the insonified volume. Hence, only for points very near the surface, will the scattered refracted wave be correlated with the scattered lateral wave, thereby contributing to the scattered intensity. For this reason, we shall neglect contributions from the cross terms, $p_{r1}p_{12}^*$ and $p_{11}p_{r2}^*$, considering them to be only a small percentage of the total intensity. With this approximation, we rewrite Equation (3.16) as:

$$I \approx \int_{V_1}\int_{V_2} Q_1 Q_2^* \cdot (p_{r1} p_{r2}^* + p_{11} p_{12}^*)\, dV_1 dV_2 \ . \qquad (3.17)$$

The remaining two terms dominate the backscattered intensity; one due to the refracted wave and a second due to the lateral wave. It now remains to solve Equation (3.17) to obtain

them. We shall consider each contribution separately, starting with the refracted wave.

3.3.1 Backscattered Intensity of the Refracted Wave

We are required to solve the equation:

$$I_{sr} \approx \int_{V_1}\int_{V_2} Q_1 Q_2^* \cdot p_{r1} p_{r2}^* \, dV_1 dV_2 \qquad (3.18)$$

to obtain I_{sr}, the backscattered intensity of the refracted wave. Q is given by Equation (3.11) and an expression for p_r is obtained in Appendix B.

$$p_r \approx M_r \exp\left\{ik_s\left(x_T \sin\theta_t + z_w\sqrt{n_{sw}^2 - \sin\theta_t^2} - z_s\cos\theta_t\right)\right\} \qquad (3.19)$$

$$M_r \approx \frac{T_{sw}(\theta_t)\sqrt{\sin\theta_t}}{\sqrt{x_T}\left[x_T\sin\theta_t - z_s\cos\theta_t + z_w\left\{\dfrac{\cos(2\theta_t)}{\sqrt{n_{sw}^2-\sin^2\theta_t}} + \dfrac{\sin^2(2\theta_t)}{4(n_{sw}^2-\sin^2\theta_t)^{3/2}}\right\}\right]^{1/2}}$$

where $T_{sw}(\theta_t)$ is the pressure transmission coefficient for a plane wave incident from the sediment at incident angle θ_t. The variables x_T, z_S, z_W and θ_t are depicted in Figure (3.2).

Substituting Equations (3.19) and (3.11) into (3.18), and using the (slightly) simpler notation of $\theta' \equiv (n^2_{sw} - \sin^2\theta)^{1/2}$, yields:

$$I_{sr} \approx \frac{|M_r|^2 |T_{ws}|^2 P_0^2}{16\pi^2} \int_{V_1,V_2} \int \left\{ \left[2\frac{\Delta c_1}{c_0} k_s^2 + i\frac{k_s}{\rho_0}\left\{ \frac{\partial(\Delta\rho_1)}{\partial x_{T1}} \sin\theta_0 - \frac{\partial(\Delta\rho_1)}{\partial z_{s1}} \cos\theta_0 \right\} \right] \cdot \right.$$

$$\left[2\frac{\Delta c_2}{c_0} (k_s^2)^* - i\frac{k_s^*}{\rho_0}\left\{ \frac{\partial(\Delta\rho_2)}{\partial x_{T2}} \sin^*\theta_0 - \frac{\partial(\Delta\rho_2)}{\partial z_{s2}} \cos^*\theta_0 \right\} \right] \cdot$$

$$\exp\left\{ ik_s(x_{T1}\sin\theta_{t1} + z_w\theta'_{t1} - z_{s1}\cos\theta_{t1}) - ik_s^*(x_{T2}\sin^*\theta_{t2} + z_w(\theta'_{t1})^* - z_{s2}\cos^*\theta_{t2}) \right\}$$

$$\left. \exp\left\{ ik_s(x_{T1}\sin\theta_0 + z_w\theta'_0 - z_{s1}\cos\theta_0) - ik_s^*(x_{T2}\sin^*\theta_0 + z_w(\theta'_0)^* - z_{s2}\cos^*\theta_0) \right\} \right\} \cdot$$

$$dV_1\, dV_2 \,. \qquad (3.20)$$

Solving Equation (3.20) will be extremely difficult unless we make some simplifying approximations. We note that for the experiments reported on herein, the receiver is located far from the insonified volume. (Recall that $R >> L_v$.) In this case we may replace θ_{t1}, θ_{t2} with θ_0 in the magnitude term $|M_r|^2$. Next referring to Figure (3.4) we note that since the correlation length is quite short, only points P_1, P_2 which are close to one another in the insonified volume, contribute to the intensity. Thus, we make the approximation $\theta_{t1} \approx \theta_{t2} \equiv \theta_t$ in the phase term of Equation (3.20).

Employing these simplifications, and factoring common terms in the exponents, we rewrite Equation (3.20) as:

$$I_{sr} \approx \frac{|M_r|^2 |T_{ws}|^2 p_0^2}{16\pi^2} \int_{V_1,V_2} \int \left\{ \left[2\frac{\Delta c_1}{c_0} k_s^2 + i\frac{k_s}{\rho_0}\left\{ \frac{\partial(\Delta\rho_1)}{\partial x_{T1}} \sin\theta_0 - \frac{\partial(\Delta\rho_1)}{\partial z_{s1}} \cos\theta_0 \right\} \right] \cdot \right.$$

$$\left[2\frac{\Delta c_2}{c_0} (k_s^2)^* - i\frac{k_s^*}{\rho_0}\left\{ \frac{\partial(\Delta\rho_2)}{\partial x_{T2}} \sin^*\theta_0 - \frac{\partial(\Delta\rho_2)}{\partial z_{s2}} \cos^*\theta_0 \right\} \right] \cdot$$

$$\exp\left\{ i|k_s|\left[a_r(x_{T1}-x_{T2}) - f_r(z_{s1}-z_{s2}) \right] \right\} \cdot \qquad (3.21)$$

$$\left. \exp\left\{ -|k_s|\left[b_r(x_{T1}+x_{T2}) + 2d_r z_w + g_r(z_{s1}+z_{s2}) \right] \right\} \right\} \, dV_1 dV_2$$

where

$$|k_s| a_r = \mathcal{R}e\{k_s(\sin\theta_0 + \sin\theta_t)\} \qquad a)$$

$$|k_s| f_r = \mathcal{R}e\{k_s(\cos\theta_0 + \cos\theta_t)\} \qquad b)$$

$$|k_s| b_r = \mathcal{I}m\{k_s(\sin\theta_0 + \sin\theta_t)\} \qquad (3.22c)$$

$$|k_s| d_r = \mathcal{I}m\{k_s\sqrt{n_{sw}^2 - \sin^2\theta_t}\} \qquad d)$$

$$|k_s| g_r = \mathcal{I}m\{k_s(\cos\theta_0 + \cos\theta_t)\} \, . \qquad e)$$

The variables a_r, b_r, d_r, f_r, g_r have been introduced to facilitate separating the exponents into real and imaginary parts; the real part accounting for attenuation of the wave in the sediment.

We now assume that fluctuations in wave speed and density in the bottom result from fluctuations in concentration. Concentration, denoted S, is defined as the ratio of the solute

density to the solvent density.[5] In the present example, the solute is water and the solvent is sediment. Thus, we may write:

$$\Delta c = \frac{\partial c}{\partial S}\Delta S, \quad \Delta \rho = \frac{\partial \rho}{\partial S}\Delta S. \tag{3.23}$$

Now define the correlation function, N_c, as:

$$N_c = \frac{\overline{\Delta S_1 \Delta S_2}}{\overline{(\Delta S)^2}} \tag{3.24}$$

where $\overline{(\Delta S)^2}$ is the mean square value of the concentration fluctuations, $\overline{\Delta S_1 \Delta S_2}$ is the cross correlation of the concentration fluctuations and the overbar signifies statistical averages of these values.

Next introduce a set of relative coordinates (x,y,z) such that:

$$x = x_{T1} - x_{T2} \tag{3.25a}$$

$$y = y_{T1} - y_{T2} \tag{3.25b}$$

---

[5] We use the quantity concentration, rather than the more common quantity porosity, to remain consistant with Chernov. The two quantities are related by: $S=\rho_{sw}\cdot[(1-P)\rho_{sd}]^{-1} - 1$, where ρ_{sw} is the wet density of the sediment (typically $\approx$ 1900kg/m^3 for water-saturated sand), ρ_{sd} is the dry density of the sediment if it contained no air gaps (typically $\approx$ 2600kg/m^3 for sand) and P is porosity. A more complete discussion of the relationship between porosity and concentration is contained in Appendix C.

$$z = z_{s1} - z_{s2} \qquad c)$$

and a set of absolute coordinates (x',y',z') such that:

$$x' = (x_{T1} + x_{T2})/2 \qquad a)$$

$$y' = (y_{T1} + y_{T2})/2 \qquad (3.26b)$$

$$z' = (z_{s1} + z_{s2})/2 \,. \qquad c)$$

Carrying out the multiplication of the terms enclosed in square brackets in Equation (3.21), employing the definitions for Δc, $\Delta \rho$, and N_c contained in Equation (3.23) and (3.24), and performing the variable transformation to relative and absolute coordinates, we may rewrite Equation (3.21) as:

$$I_{sr} \approx \frac{|M_r|^2 |T_{ws}|^2 P_0^2 (\overline{\Delta S})^2}{16\pi^2} \int_{V,V'} \int \Bigg[\frac{4|k_s|^4}{c_0^2} \left(\frac{\partial c}{\partial S}\right)^2 N_c +$$

$$i \frac{2|k_s|^2}{\rho_0 c_0} \cdot \frac{\partial c}{\partial S} \cdot \frac{\partial \rho}{\partial S} \left\{ \frac{\partial N_c}{\partial x} \left(k_s^* \sin\Theta_0 + k_s \sin^*\Theta_0 \right) - \frac{\partial N_c}{\partial z} \left(k_s^* \cos\Theta_0 + k_s \cos^*\Theta_0 \right) \right\} -$$

$$\frac{|k_s|^2}{\rho_0^2} \left(\frac{\partial \rho}{\partial S}\right)^2 \left\{ \frac{\partial^2 N_c}{\partial x^2} |\sin\Theta_0|^2 + \frac{\partial^2 N_c}{\partial z^2} |\cos\Theta_0|^2 - \frac{\partial^2 N_c}{\partial x \partial z} \left(\sin\Theta_0 \cos^*\Theta_0 + \sin^*\Theta_0 \cos\Theta_0 \right) \right\} \cdot$$

$$\exp\left\{ i|k_s| (a_r x - f_r z) - 2|k_s| (b_r x' + d_r z_w + g_r z') \right\} \Bigg] dV \, dV' \qquad (3.27)$$

where dV=dxdydz, and dV'=dx'dy'dz'. Equation (3.27) is valid as long as the concentration fluctuations are stationary. The details of the transformation of Equation (3.21) to (3.27) are contained in Appendix D.

Following Chernov[11], we perform an integration by parts on the derivatives of N_c contained in Equation (3.27). The details of this too are relegated to Appendix D. The integration by parts yields:

$$I_{sr} \approx C_r \cdot \int_{V,V'} \int D_r(x',z') N_c \exp\left\{ i|k_s|(a_r x - f_r z) - 2|k_s|(b_r x' + d_r z_w + g_r z') \right\} dV\, dV' \tag{3.28}$$

$$C_r = \frac{|M_r|^2 |T_{ws}|^2 P_0^2 (\overline{\Delta S})^2 |k_s|^4}{16\pi^2}$$

$$D_r(x',z') = \left[\frac{4}{c_0^2}\left(\frac{\partial c}{\partial S}\right)^2 + \frac{4}{\rho_0 c_0} \cdot \frac{\partial c}{\partial S} \cdot \frac{\partial \rho}{\partial S} \left\{ a_r \mathcal{R}e\{(1-iA)\sin\theta_0\} + f_r \mathcal{R}e\{(1-iA)\cos\theta_0\} \right\} + \right.$$

$$\left. \frac{1}{\rho_0^2} \cdot \left(\frac{\partial \rho}{\partial S}\right)^2 \left\{ a_r^2 |\sin\theta_0|^2 + f_r^2 |\cos\theta_0|^2 + 2 a_r f_r \mathcal{R}e\{\sin\theta_0 \cos^* \theta_0\} \right\} \right]$$

where $k_s \equiv \omega/c_0(1+iA_0)$ with A_0 real and much less than 1.

No further progress can be made on Equation (3.28) without an estimate of the correlation function, N_c. Before doing so, we shall derive an expression for the backscattered intensity of the lateral wave, employing a method similar to that of section (3.3.1).

3.3.2 Backscattered Intensity of the Lateral Wave

We are required to solve the equation:

$$I_{sl} \approx \int_{V_1,V_2} \int Q_1 Q_2^* \cdot p_{11} p_{12}^*\, dV_1 dV_2 \tag{3.29}$$

to obtain I_{sl}, the backscattered intensity of the lateral wave. Q is given by Equation (3.11) and an expression for p_1 is obtained in Appendix B.

$$p_1 \approx M_1 \exp\left\{ik_w\left(x_T\sin\beta+z_w\cos\beta-z_s\sqrt{n_{ws}^2-\sin^2\beta}\ \right)\right\} \qquad (3.30)$$

$$M_1 \approx \frac{n_{sw}T_{sw}(\beta)\sqrt{\sin\beta}\cos\beta\Big/\sqrt{1-n_{sw}^2\sin^2\beta}}{\sqrt{x_T}\left[x_T\sin\beta+z_w\cos\beta-z_s\left\{\dfrac{\cos(2\beta)}{\sqrt{n_{ws}^2-\sin^2\beta}}+\dfrac{\sin^2(2\beta)}{4(n_{ws}^2-\sin^2\beta)^{3/2}}\right\}\right]^{1/2}}$$

where $T_{sw}(\beta)$ is the pressure transmission coefficient for a plane wave incident from the sediment at angle β and $n_{ws}=1/n_{sw}$. (Refer to Figure 3.2.)

Substituting Equations (3.30) and (3.11) into (3.29), writing $k_w=k_s n_{sw}$, and using $\theta'\equiv(n^2_{sw}-\sin^2\theta)^{1/2}$, $\beta'\equiv(n^2_{ws}-\sin^2\beta)^{1/2}$, yields:

$$I_{s1} \approx \frac{|M_1|^2|T_{ws}|^2p_0^2}{16\pi^2}\int_{V_1,V_2}\int\left\{\left[2\frac{\Delta c_1}{c_0}k_s^2+i\frac{k_s}{\rho_0}\left\{\frac{\partial(\Delta\rho_1)}{\partial x_{T1}}\sin\theta_0-\frac{\partial(\Delta\rho_1)}{\partial z_{s1}}\cos\theta_0\right\}\right]\cdot\right.$$
$$\left.\left[2\frac{\Delta c_2}{c_0}(k_s^2)^*-i\frac{k_s^*}{\rho_0}\left\{\frac{\partial(\Delta\rho_2)}{\partial x_{T2}}\sin^*\theta_0-\frac{\partial(\Delta\rho_2)}{\partial z_{s2}}\cos^*\theta_0\right\}\right]\cdot\right.$$
$$\exp\left\{ik_s n_{sw}(x_{T1}\sin\beta_1+z_w\cos\beta_1-z_{s1}\beta_1')-ik_s^*n_{sw}^*(x_{T2}\sin^*\beta_2+z_w\cos^*\beta_2-z_{s2}(\beta_2')^*)\right\}$$
$$\left.\exp\left\{ik_s(x_{T1}\sin\theta_0+z_w\theta_0'-z_{s1}\cos\theta_0)-ik_s^*(x_{T2}\sin^*\theta_0+z_w(\theta_0')^*-z_{s2}\cos^*\theta_0)\right\}\right\}\cdot$$
$$dV_1\,dV_2\,. \qquad (3.31)$$

Following the lead of Equation (3.20), we approximate the angle β by θ_0 in the magnitude term $|M_1|^2$. Further, we let $\beta_1\approx\beta_2\equiv\beta$ in the exponents of Equation (3.31).

Employing these simplifications, and factoring common terms in the exponents, we rewrite Equation (3.31) as:

$$I_{s1} \approx \frac{|M_1|^2|T_{ws}|^2 P_0^2}{16\pi^2}\int_{V_1,V_2}\left\{\left[2\frac{\Delta c_1}{c_0}k_s^2+i\frac{k_s}{\rho_0}\left\{\frac{\partial(\Delta\rho_1)}{\partial x_{T1}}\sin\theta_0-\frac{\partial(\Delta\rho_1)}{\partial z_{s1}}\cos\theta_0\right\}\right]\cdot\right.$$

$$\left[2\frac{\Delta c_2}{c_0}(k_s^2)^*-i\frac{k_s^*}{\rho_0}\left\{\frac{\partial(\Delta\rho_2)}{\partial x_{T2}}\sin^*\theta_0-\frac{\partial(\Delta\rho_2)}{\partial z_{s2}}\cos^*\theta_0\right\}\right]\cdot$$

$$\exp\left\{i|k_s|\left[a_1(x_{T1}-x_{T2})-f_1(z_{s1}-z_{s2})\right]\right\}\cdot$$

$$\left.\exp\left\{-|k_s|\left[b_1(x_{T1}+x_{T2})+2d_1z_w+g_1(z_{s1}+z_{s2})\right]\right\}\right\}\,dV_1dV_2 \qquad (3.32)$$

where

$$|k_s|a_1 = \mathcal{R}e\{k_s(\sin\theta_0+\sin\beta)\} \qquad a)$$

$$|k_s|f_1 = \mathcal{R}e\{k_s(\cos\theta_0+n_{sw}\sqrt{n_{ws}^2-\sin^2\beta}\,)\} \qquad b)$$

$$|k_s|b_1 = \mathcal{I}m\{k_s(\sin\theta_0+\sin\beta)\} \qquad (3.33c)$$

$$|k_s|d_1 = \mathcal{I}m\{k_s n_{sw}\cos\beta\} \qquad d)$$

$$|k_s|g_1 = \mathcal{I}m\{k_s(\cos\theta_0+n_{sw}\sqrt{n_{ws}^2-\sin^2\beta}\,)\}\,. \qquad e)$$

The similarity between Equations (3.32), (3.33) and Equations (3.21), (3.22) is clearly in evidence. Employing an analogous procedure on Equation (3.32), to that used in transforming Equation (3.21) to Equation (3.28), we obtain:

$$I_{s1} \approx C_1 \int_{V,V'} \int D_1(x',z') N_c \exp\left\{ i|k_s|(a_1 x - f_1 z) - 2|k_s|(b_1 x' + d_1 z_w + g_1 z') \right\} dV\, dV'$$

$$C_1 = \frac{|M_1|^2 |T_{ws}|^2 P_0^2 (\overline{\Delta S})^2 |k_s|^4}{16\pi^2} \qquad (3.34)$$

$$D_1(x',z') = \left[\frac{4}{c_0^2}\left(\frac{\partial c}{\partial S}\right)^2 + \frac{4}{\rho_0 c_0}\cdot\frac{\partial c}{\partial S}\cdot\frac{\partial \rho}{\partial S}\left\{ a_1 \mathcal{R}e\{(1-iA)\sin\theta_0\} + f_1 \mathcal{R}e\{(1-iA)\cos\theta_0\}\right\} + \right.$$

$$\left. \frac{1}{\rho_0^2}\cdot\left(\frac{\partial \rho}{\partial S}\right)^2 \left\{ a_1^2 |\sin\theta_0|^2 + f_1^2 |\cos\theta_0|^2 + 2 a_1 f_1 \mathcal{R}e\{\sin\theta_0 \cos^*\theta_0\}\right\}\right] .$$

Obtaining numerical estimates of the backscattered intensity from Equations (3.28) and (3.34), requires specific expressions for the correlation function. Several possible expressions are presented below.

3.4 Solutions to the Backscattering Equations for Specific Forms of the Correlation Function

In the following section, Equations (3.28) and (3.34) are evaluated using three different forms for the correlation function, N_c. Two of the choices, an exponentially decaying correlation and a Gaussian correlation, are based on the model ocean bottom used in the experiments. The third choice, assumes that the bottom consists of a large number of independent scattering centres. The latter has often been used in empirical acoustic scattering models[73].

Before substituting the various expressions for the correlation function into Equations (3.28) and (3.34), we make the following observations. θ_t and β are functions of both absolute and relative coordinates. However, if the correlation length is short (as has been assumed all along), then the volume which

contributes appreciably to the integral over the relative coordinates is much less than the volume insonified. This allows us to approximate the angles θ_t and β to constants for the integration over the relative coordinates. Furthermore, since the dimensions of the insonified volume are much greater than the correlation length, we may extend the limits of integration of the relative coordinates to infinity, without altering the result significantly. We now turn to the exponentially decaying correlation function.

3.4.1 Case 1: The Exponentially Decaying Correlation Function

We shall begin by assuming that the correlation function is independent in the vertical and horizontal directions and that it exhibits radial symmetry in the horizontal plane. We write:

$$N_c = e^{-\left(\frac{r}{r_0}+\frac{z}{z_0}\right)} \tag{3.35}$$

where $r=(x^2+y^2)^{1/2}$ and r_0 and z_0 are the radial and vertical correlation lengths, respectively. As before, we shall deal with the refractive and lateral terms separately, beginning with the refractive term.

Subtituting Equation (3.35) into (3.28), we are required to solve:

$$I_{sr} \approx C_r \int_{V'} D_r(x',z') \cdot e^{-2|k_s|(b_r x' + d_r z_w + g_r z')} \cdot \left[\int_V e^{-\left(\frac{r}{r_0}+\frac{z}{z_0}\right)+i|k_s|(a_r x - f_r z)} dx\,dy\,dz \right] \cdot dx'\,dy'\,dz' \tag{3.36}$$

where the integral over the relative coordinates (x,y,z) is given by the expression in square brackets. To take advantage of symmetry, we transform the integral in square brackets to cylindrical coordinates to obtain:

$$I_{sr} \approx C_r \int_V D_r(x',z') \exp\left\{-2|k_s|(b_r x' + d_r z_w + g_r z')\right\} \cdot \left[\int_{0,0,-\infty}^{\infty,2\pi,\infty} \exp\left\{-\frac{r}{r_0} - \frac{z}{z_0} + i|k_s|(a_r r - f_r z)\right\} r \, dz \, d\theta \, dr \right] dV. \quad (3.37)$$

Performing the integration over the relative coordinates (r,Θ,z) and substituting the result into Equation (3.36) yields:

$$I_{sr} \approx 4\pi C_r \int_{V'} D_r(x',z') \cdot \frac{z_0 r_0^2 \cdot e^{-2|k_s|(b_r x' + d_r z_w + g_r z')}}{(1+(r_0 a_r |k_s|)^2)^{3/2}(1+(z_0 f_r |k_s|)^2)} dV'. \quad (3.38)$$

Since Equation (3.38) is independent of y', the integral over dy' merely introduces a factor of ΔY, the width of the insonified patch. However, the author has not managed to integrate the x',z' coordinates analytically. Instead, a two-dimensional Monte Carlo integration was used, the details of which are contained in Appendix E. Thus, the backscattered intensity of the refractive component, with a correlation function defined by Equation (3.35) is:

$$I_{sr} \approx 4\pi \cdot C_r \Delta Y \int_{x',z'} D_r(x',z') \frac{z_0 r_0^2 \cdot \exp\left\{-2|k_s|(b_r x' + d_r z_w + g_r z')\right\}}{(1+(r_0 a_r |k_s|)^2)^{3/2} \cdot (1+(z_0 f_r |k_s|)^2)} dx' dz'. \quad (3.39)$$

To obtain the backscattered intensity of the lateral wave, we substitute Equation (3.35) into Equation (3.34), transform the relative coordinates from rectangular to cylindrical, and perform the integration over dv and dy'. Thus, we obtain, for the backscattered intensity of the lateral wave:

$$I_{sl} \approx 4\pi \cdot C_l \, \Delta Y \iint_{x',z'} D_l(x',z') \cdot \frac{z_0 r_0^2 \cdot \exp\left\{-2|k_s|(b_l x' + d_l z_w + g_l z')\right\}}{(1+(r_0 a_l |k_s|)^2)^{3/2} \cdot (1+(z_0 f_l |k_s|)^2)} dx'dz' \qquad (3.40)$$

which is solved using a two-dimensional Monte Carlo integration over x',z'.

If the correlation function is not radially symmetric in the horizontal plane, but instead independent in the x and y directions, we can write:

$$N_c = e^{-\left(\frac{x}{x_0} + \frac{y}{y_0} + \frac{z}{z_0}\right)}. \qquad (3.41)$$

If Equation (3.41) is substituted into (3.28) and the integration over dv and dy' is performed, we obtain for the backscattered intensity of the refracted wave:

$$I_{sr} \approx 8 \cdot C_r \, \Delta Y \iint_{x',z'} D_r(x',z') \frac{x_0 y_0 z_0 \exp\left\{-2|k_s|(b_r x' + d_r z_w + g_r z')\right\}}{(1+(x_0 a_r |k_s|)^2)(1+(z_0 f_r |k_s|)^2)} dx'dz' \qquad (3.42)$$

and for the backscattered intensity of the lateral wave:

$$I_{sl} \approx 8 \cdot C_l \, \Delta Y \iint_{x',z'} D_l(x',z') \cdot \frac{x_0 y_0 z_0 \exp\left\{-2|k_s|(b_l x' + d_l z_w + g_l z')\right\}}{(1+(x_0 a_l |k_s|)^2) \cdot (1+(z_0 f_l |k_s|)^2)} dx'dz'. \qquad (3.43)$$

3.4.2 Case 2: The Gaussian Correlation Function

Again, we begin by considering a correlation function independent in the vertical and horizontal directions which is radially symmetric in the horizontal plane. For a Gaussian normalized to unity with zero mean, we write:

$$N_c \approx e^{-\left(\left(\frac{r}{r_0}\right)^2+\left(\frac{z}{z_0}\right)^2\right)} . \tag{3.44}$$

To obtain the refractive term, we substitute Equation (3.44) into (3.28) and transform the integral over rectangular coordinates (x,y,z) to cylindrical coordinates (r,Θ,z). This obtains:

$$I_{sr} \approx C_r \int_V D_r(x',z') \cdot \exp\left\{-2|k_s|(b_r x' + d_r z_w + g_r z')\right\} \cdot$$

$$\left[\int_{0,0,-\infty}^{\infty,2\pi,\infty} \exp\left\{-\left(\frac{r}{r_0}\right)^2-\left(\frac{z}{z_0}\right)^2+i|k_s|(a_r r - f_r z)\right\} r\, dz\, d\Theta\, dr\right] dV' . \tag{3.45}$$

Performing the integration over dr,dΘ,dz and dy' obtains the backscattered intensity of the refracted wave, for a correlation function given by Equation (3.44):

$$I_{sr} \approx \pi^{3/2} C_r \Delta Y \iint_{x',z'} D_r(x',z') \cdot \exp\left\{-2|k_s|(b_r x' + d_r z_w + g_r z')\right\} \cdot$$

$$z_0 r_0^2 \cdot \exp\left\{-\left(\frac{r_0 a_r |k_s|}{2}\right)^2-\left(\frac{z_0 f_r |k_s|}{2}\right)^2\right\} dx'\, dz' . \tag{3.46}$$

To obtain the lateral wave contribution, we substitute Equation (3.44) into (3.34) and transform the integral over

relative coordinates from rectangular to cylindrical. Performing the integration over dr,dΘ,dz and dy' obtains the backscattered intensity of the lateral wave, for a correlation function given by Equation (3.44):

$$I_{sl} \approx \pi^{3/2} C_l \Delta Y \iint_{x',z'} D_l(x',z') \cdot \exp\left\{-2|k_s|(b_l x' + d_l z_w + g_l z')\right\} \cdot$$

$$z_0 r_0^2 \cdot \exp\left\{-\left(\frac{r_0 a_l |k_s|}{2}\right)^2 - \left(\frac{z_0 f_l |k_s|}{2}\right)^2\right\} dx'\,dz' . \qquad (3.47)$$

If the Gaussian correlation function is not radially symmetric in the horizontal plane, but instead independent in the x and y directions we can write:

$$N_c = e^{-\left(\left(\frac{x}{x_0}\right)^2 + \left(\frac{y}{y_0}\right)^2 + \left(\frac{z}{z_0}\right)^2\right)} . \qquad (3.48)$$

If Equation (3.48) is substituted into (3.28) and the integration over dv and dy' is performed, we obtain for the backscattered intensity of the refracted wave:

$$I_{sr} \approx \pi^{3/2} C_r \Delta Y \iint_{x',z'} D_r(x',z') \cdot \exp\left\{-2|k_s|(b_r x' + d_r z_w + g_r z')\right\} \cdot$$

$$x_0 y_0 z_0 \cdot \exp\left\{-\left(\frac{x_0 a_r |k_s|}{2}\right)^2 - \left(\frac{z_0 f_r |k_s|}{2}\right)^2\right\} dx'\,dz' \qquad (3.49)$$

and for the backscattered intensity of the lateral wave:

$$I_{s1} \approx \pi^{3/2} C_1 \Delta Y \iint_{x',z'} D_1(x',z') \cdot \exp\left\{-2|k_s|(b_1 x' + d_1 z_w + g_1 z')\right\} \cdot$$

$$x_0 y_0 z_0 \cdot \exp\left\{-\left(\frac{x_0 a_1 |k_s|}{2}\right)^2 - \left(\frac{z_0 f_1 |k_s|}{2}\right)^2\right\} dx'\,dz' \,. \qquad (3.50)$$

3.4.3 Case 3: Zero Correlation Between Individual Scatterers

As stated above, many empirical models of volume scattering assume that the bottom consists of a large number of independent scatterers. In this case, the total backscattered intensity is the uncorrelated sum of the contribution from each of the scatterers. To deal with this using the present model, we consider the scattering volume to consist of a large number of scattering centres; each one uncorrelated with its "neighbours". Within the volume of any scattering centre the correlation will be unity. As this is a fairly crude approximation, three-dimensional radial symmetry shall be assumed without justification. The correlation function may be written:

$$N_c = \begin{cases} 1; & \rho \le a_0 \\ 0; & \rho > a_0 \end{cases} \qquad (3.51)$$

where a_0 is the radius of the scattering centre and ρ is the displacement from the origin (in the relative coordinate system) to the point (x,y,z).

To obtain the refractive term we substitute Equation (3.51) into (3.28) and transform the integral over rectangular coordinates (x,y,z) to spherical polar coordinates (ρ,θ,φ). This obtains:

$$I_{sr} \approx C_r \int_{V'} D_r(x',z') \exp\{-2|k_s|(b_r x' + d_r z_w + g_r z')\} \cdot$$

$$\left[\int_{0,0,0}^{a_0,\pi,2\pi} \exp\{iK_r \rho \cos\varphi\} \rho^2 \sin\varphi \, d\theta d\varphi d\rho \right] dV' \qquad (3.52)$$

where $K_r = |k_s|^2(a_r^2 + f_r^2)$. Note that we can no longer extend the limits on the relative coordinates to infinity due to the discontinuous nature of the correlation function. Instead we integrate only over the volume of the scattering centre, noting that the contribution outside will be zero. Performing the integration over $dr, d\theta, d\varphi$ and dy' obtains the backscattered intensity of the refracted wave, for a correlation function given by Equation (3.51):

$$I_{sr} \approx \frac{4\pi}{K_r^3} C_r \Delta Y \int_{x',z'} \int D_r(x',z') \exp\{-2|k_s|(b_r x' + d_r z_w + g_r z')\} \cdot$$

$$(\sin(K_r a_0) - K_r a_0 \cos(K_r a_0)) \, dx' dz' . \qquad (3.53)$$

To obtain the lateral wave contribution, we substitute Equation (3.51) into (3.34) and transform the integral over rectangular coordinates (x,y,z) to spherical polar coordinates (r,θ,φ). Performing the integration over $dr, d\theta, d\varphi$ and dy' obtains the backscattered intensity of the lateral wave, for a correlation function given by Equation (3.51):

$$I_{s1} \approx \frac{4\pi}{K_1^3} C_1 \Delta Y \iint_{x',z'} D_1(x',z') \cdot \exp\left\{-2|k_s|(b_1 x' + d_1 z_w + g_1 z')\right\} \cdot$$

$$(\sin(K_1 a_0) - K_1 a_0 \cos(K_1 a_0))\, dx'dz' \qquad (3.54)$$

where $K_1 = |k_s|^2(a_1^2 + f_1^2)$.

This completes the theoretical development of acoustic backscatter from the volume beneath a planar, water/sediment interface. The curves obtained from Equations (3.28) and (3.34) for the choices of correlation function outlined above will be discussed presently. We turn first, however, to a discussion of the experiments performed to measure the backscattered intensity.

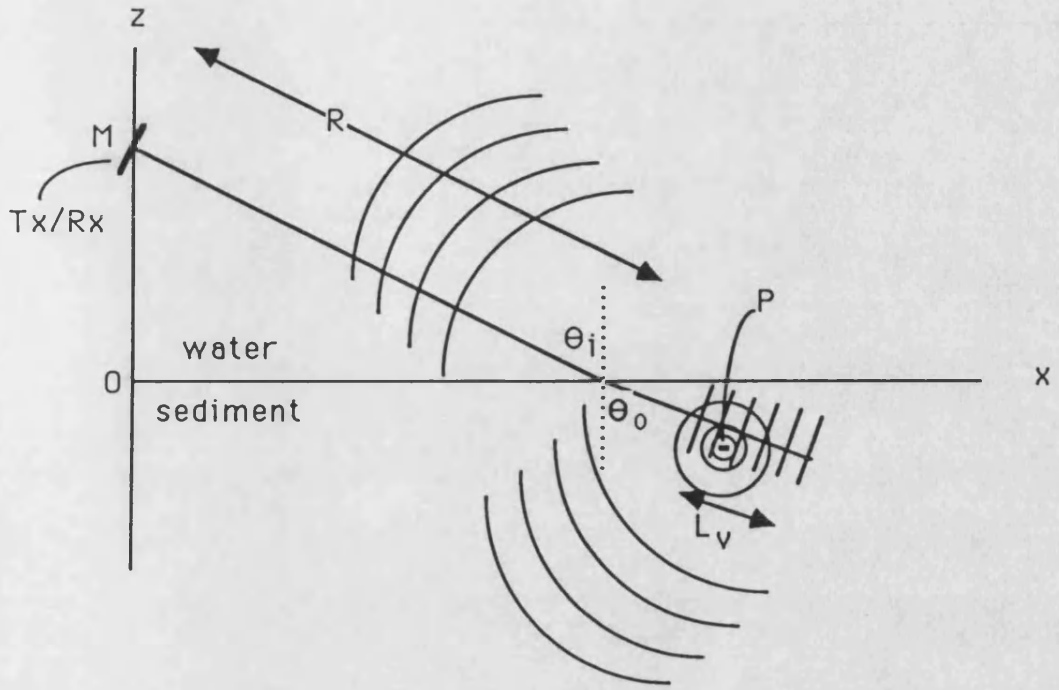

Figure (3.1): Schematic of backscatter geometry. The inhomogeneities at 'P' scatter part of the incident plane wave into spherical waves.

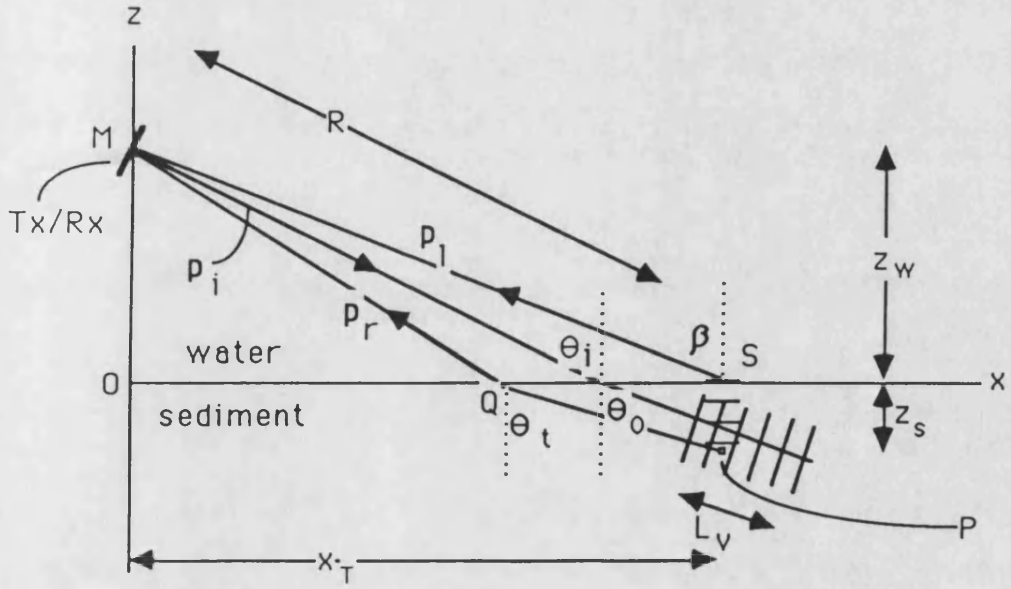

Figure (3.2): Paths for incident, refracted and lateral waves in steepest descents approximation.

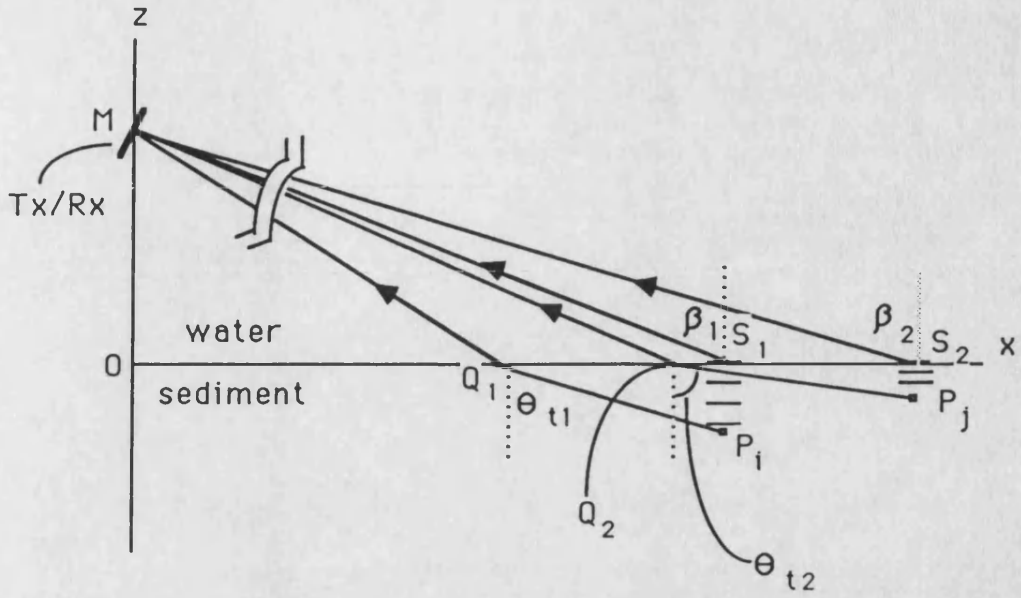

Figure (3.3): Steepest descent paths of waves scattered from points P_i and P_j. Incident ray paths are omitted for clarity.

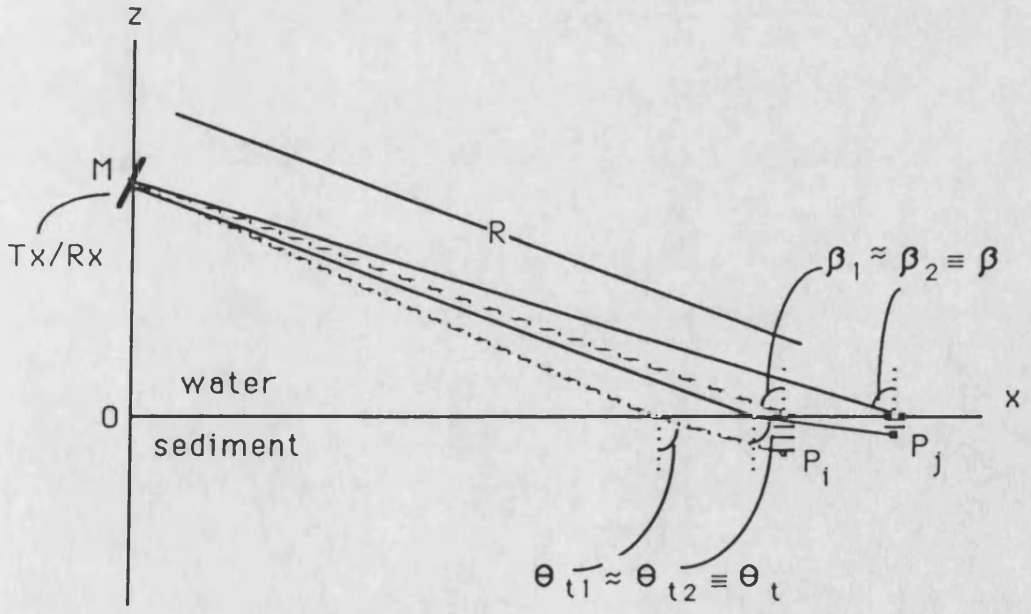

Figure (3.4): Approximations for the backscatter angles used in phase terms of Equations (3.20) and (3.31).

CHAPTER 4

EXPERIMENTAL FACILITY AND THE EXPERIMENT

A set of laboratory experiments were performed to measure acoustic backscatter from the volume beneath a smooth interface. A laboratory experiment permitted control of parameters such as bottom type and grazing angle. (This is in stark contrast to most sea based experiments.) Furthermore, by carefully setting up the experiment, one could avoid anomalies often present in the ocean bottom; biological activity in the form of Sand Dollars, for example. In this chapter, the experimental setup and procedure, as well as the data acquisition systems are described.

4.1 General Experimental Facility

The experiments were carried out at the University of Bath, School of Physics, Bath, England. A water filled tank measuring approximately 5m x 1.5m x 2m, (LxWxD) housed the experiment. Set inside this tank was an inner tank measuring 1.3m x 1.3m x 1m. The inner tank was filled with water-saturated sand which was used as the inhomogeneous medium.

4.1.1 The Gantry System

Control of the experiments was maintained via, a computerized gantry. Figure (4.1) contains a schematic diagram of the tank and gantry. The gantry system permits acoustic sensors mounted to it, five degrees of freedom. Movement in the horizontal plane, denoted (x,y), is accomplished via two sets of horizontal tracks. One set is laid in the x direction along either side of the tank. A framework, housing a central, vertical column and mounted onto a set of 4 wheels is placed on the tracks. This permits the framework to travel in the x direction. Part of this

framework consists of a second set of tracks, positioned perpendicular to the first set (y direction). The central column is fixed to a second, wheeled framework to permit movement in the y direction. The central column can be lowered or raised (z direction) and rotated about its vertical axis (Θ direction) as required. A small, motorized armature at the base of the central column enables sensors attached to it to rotate, thereby varying the grazing angle (φ_g direction). Movement in all directions, except z, are controlled via a Hewlett Packart hp9825 minicomputer. The z direction is manually controlled.

4.1.2 The Parametric Array

A parametric array was utilized as the acoustic source for the backscatter experiments. Berktay[74] contains a general discussion of parametric arrays. Briefly, a parametric array is formed by the nonlinear interaction of a pair of collimated waves propagating simultaneously through the same region of water. The nonlinear interaction of the waves of frequencies f_{p1} and f_{p2}, (known as primaries) generates a wave of frequency, $f_d=f_{p2}-f_{p1}$ (known as the difference frequency). In practice, the primaries are generated by the same transducer.

There are several advantages in using the parametric array. First, the difference frequency has a much narrower beamwidth than would be obtained by generating a signal at the difference frequency directly, with a transducer of the dimensions used to generate the primaries. The two-sided -3 dB (intensity) beam width for a parametric array, denoted 2ψ, measured in the farfield, is contained in Thorne[5]:

$$2\psi = 4\sin^{-1}[(\alpha_T/2k_d)^{1/2}] \quad (4.1)$$

where k_d is the difference wavenumber and $\alpha_T=\alpha_{p1}+\alpha_{p2}-\alpha_d$, and α_{p1}, α_{p2}, α_d are the absorption coefficients of the primary frequencies and difference frequency respectively. Secondly, the difference frequency wave has no side lobes. The directivity function, D, also contained in Thorne[5] is:

$$D = [1 + (2k_d/\alpha_T)^2\sin^4(\psi/2)]^{-1/2} \quad (4.2)$$

which decreases monotonically. The third advantage in using a parametric array is that a low 'Q' is achieved at the difference frequency. This means that the parametric array can be used as a wideband source at the difference frequency. Mathematically, Muir and Blue[75] approximate the difference frequency 'Q' as:

$$Q_d = Q_p f_d[(f_{p1} + f_{p2})/2]^{-1} \quad (4.3)$$

where Q_p is the 'Q' at the primaries.

The main disadvantage in employing a parametric array is that the conversion of energy from the primary frequencies to the difference frequency is a second order process, making it quite inefficient. However, if one is not limited by the magnitude of the pressure generated at the difference frequency, this is not a problem. In the present case, the experiments performed indicated that sufficient signal could be attained employing a parametric array, provided enough time averages were taken.

4.2 Design and Construction of a Model Ocean Bottom

The aim of the experiments was to test the ability of the model developed in Chapter 3, to predict volume backscatter in an inhomogeneous medium. The medium chosen, thin layers of water-saturated sand, contained random fluctuations in the density and wave speed, which were independent horizontally and vertically. This choice of medium, was based on the geophysical model of the ocean discussed in section 2.4 [55]. This afforded an opportunity to compare the laboratory results, with backscatter data obtained from experiments at sea.

To achieve the desired inhomogeneities in a laboratory medium, a sequence of horizontal sand layers was used. Each layer comprised sand of a specific mean grain size. Since porosity (and hence concentration) is a function of grain size [35], altering the grain size results in fluctuations in concentration[1]. (The relationship between these parameters is discussed in Appendix C.) The layer thickness controlled the length scale of the vertical inhomogeneities[2]. Gentle undulations in individual layer thickness, due to the sand laying process (described below) resulted in horizontal inhomogeneities. This is depicted schematically in Figure (4.2).

There were a number of practical considerations in constructing the model ocean bottom. These are examined next.

---

[1]Recall from Equation (3.23) that concentration fluctuations result in wave speed and density fluctuations which in turn result in scattering.

[2]Fluctuations about the mean grain size within a given layer were considered to be a second order effect and consequently ignored.

4.2.1 The Criteria For the Sand Volume

Keeping the vertical inhomogeneities short scale required making each sand layer as thin as possible. Design limitations in the layering device described below, restricted this minimum to 7mm. To prevent the incident wave from "seeing" individual layers, an upper limit of 200kHz ($\lambda \approx 8.5$mm in the sediment.) was placed on the frequency range of the experiments.

A further limitation in constructing the scattering medium was the availablity of sands of different mean grain size, within a useable range. A mean grain size of less than about 50μm was too "clay like", making layering and smoothing very difficult. Mean grain sizes larger than about 1000μm made it difficult to construct the thin layers required in the model. Also, many assumptions valid for sand and clay are not valid for pebbles. Restricting particle sizes to less than 1000μm prevented inclusion of "pebble sized" particles. These limits on useable particle sizes are somewhat arbitrary of course, but provided a framework for selecting the sands.

Within the useable range, four candidate sizes of sand were available. The mean grain sizes of the four sands were: 50μm, 130μm, 250μm, and 600μm. A random number generator was used to select the layering sequence of the four sand sizes. Recall from Equation (3.27) that volume backscatter is proportional to the mean square of the concentration fluctuations. By biasing the output of the random number generator to favour the extreme grain sizes, the mean square of the concentration fluctuations, and hence the backscatter could be increased.

Biasing the choice of layers, while increasing backscatter, generated a new difficulty. It increased the probability that the random number generator would select the same grain size twice in a row. Theoretically, this is quite acceptable in a random sequence. However, the layer thickness was already determining the upper frequency limit of the backscatter experiments. Any further limitations were undesirable, making back to back layering of the same grain size unacceptable.

A 50μsec pulse was to be used in the backscatter experiments. This equates to a sand depth of about 8cm at normal incidence. Sixteen layers were placed so that the whole pulse would be contained within the inhomogeneous medium. Beneath the bottom layer was a further 75cm of 250μm sand to prevent scattering from abrupt impedance changes at the boundary.

Finally, the smallest practical grain size was chosen for the water/bottom interface to reduce surface roughness scattering. The 50μm sand was too difficult to smooth after being laid, so the 130μm size was used as a compromise.

A random number generator was run, selecting from the four choices of sand until a sequence was found which fit the above criteria. The sequence is shown in Table 4.1. There now remained the difficulty of laying the sand.

4.2.2 Constuction of the Sand Volume Using the "Sandlayer"

The 50μm, 130μm, and 250μm sand grades were purchased from "British Industrial Sands", in Redhill, Surrey, England. A fourth grade of mean grain size 600μm was purchased from "Buckland Silica Sand" in Reigate, Surrey.

Before placing the dry sand in the tank, the sand required de-airing. Otherwise erroneous backscattering measurements would be recorded, as the dominant inhomogeneities would result from air bubbles trapped between the sand grains. To accomplish the de-airing, a single sand grade was loaded into a vacuum sealed container in portions of one hundred weight. A vacuum pump reduced the pressure in the container to a level of 2 kPa gauge. The vacuum was maintained for a period of one hour. Water was then bled into the container to saturate the sand. The container, with the vacuum maintained, was lowered underwater via a crane. The sand was removed from the container, while underwater, and placed inside a temporary holding vessel. This procedure was repeated until 4 vessels, each containing a different sand grade, were filled. The inner tank was then filled with 250μm sand to a depth of 75 cm. At this point, the layering process began.

Table 4.1

Layer #	Mean particle size (μm)	Layer #	Mean particle size (μm)
1 (deepest)	250	9	130
2	600	10	250
3	50	11	50
4	600	12	130
5	130	13	600
6	600	14	50
7	250	15	250
8	600	16 (surface)	130

In order to construct the scattering layers, a unique (to the author's knowledge) sand layering device was designed. Hereafter, the device will be referred to as the "sandlayer". A photograph of the sandlayer in operation is shown in Figure (4.3).

Figure (4.4) contains a schematic of the sandlayer. It consisted of an aluminum frame with levelling legs, and a removable, polyvinylchloride (PVC) tray. The tray was set 7mm below the top plane of the frame. Along the width of the underside of the tray, a 1cm diameter aluminum rod was mounted. The rod was free to rotate axially. Fastened to the front end of the frame, along the entire width of the tray, was a sheet of thin plastic. The plastic lay on top of the tray and was fastened to the aluminum rod at the other end.

The sandlayer was set on top of the inner tank and leveled. The appropriate sand grade was scooped in small portions and layed on the plastic sheet covering the tray. When enough sand had been placed on the tray, a length of angle aluminum was layed across the width of the sandlayer frame and used to scrape off the excess sand. (Pieces of plastic skirting were hung from the four sides of the frame to prevent the sand that was scraped off from corrupting previous layers.) After scraping, a smooth 7mm layer of sand remained on the tray. The tray was then connected to the motorized gantry which pulled it out of the frame at a slow, constant speed (0.75cm/sec). As the tray was removed, the plastic was wound onto the aluminum rod. Because there was no relative motion between the sand and the plastic sheet, the sand simply fell vertically from the tray into the tank to form a

layer.[3] (See Figure (4.5)). This process was repeated until the layer sequence of Table 4.1 was finished. When the final layer of sand was in place, it was carefully smoothed to minimize surface backscatter. All volume backscatter experiments were performed using this volume.

4.3 The Experiments

Having constructed a model ocean bottom, experiments were performed to measure volume and surface backscatter from it. Along with backscatter experiments, the incident intensity of the acoustic source was measured, to facilitate calculation of the backscattering strength. Finally, an experiment designed to estimate the length scale of the horizontal inhomogeneities was performed. Before describing the experiments, a description of the transmit and receive electronics, used in the backscatter experiments is presented.

4.3.1 Transmit and Receive Electronics: Backscatter Experiment

The transmit and receive electronics are depicted schematically in Figure (4.6). The primary frequencies for the parametric array were generated by modulating a carrier wave of the form $A_1 \cdot \cos(\omega_c t)$, with a signal of the form $\cos(\omega_m t)$. The carrier wave was generated by an analogue sine wave generator on which both pulse length and duty cycle could be controlled. This signal was input to a digital function generator which could be programmed to output the required modulation waveform. The resulting signal, W, can be expressed mathematically as:

---

[3]The plastic sheet separating sand and tray was crucial to the functioning of the sandlayer. Without it, friction caused the sand to remain on the tray as it was removed from the frame.

$$W = A_1 \cdot \cos(\omega_m t)\cos(\omega_c t) \quad (4.4)$$

where A_1 is the pressure amplitude and ω_m and ω_c are respectively, the modulation and carrier frequencies expressed in radians/second. Equation (4.4), is equivalent to:

$$W = (A_1/2)\cdot(\cos(\omega_{p1} t) + \cos(\omega_{p2} t)) \quad (4.5)$$

where $\omega_{p1}=\omega_c+\omega_m$, and $\omega_{p2}=\omega_c-\omega_m$, and the subscripts "p1" and "p2" denote primary frequencies. The resultant signal was fed into an attenuator via a voltage follower. (The voltage follower provided impedance matching between the modulator and attenuator.) The attenuator output could be varied from 0 dB to -100 dB in 1dB increments providing control of the transmitted signal amplitude. The output of the attenuator was input to a 200W ENI power amplifier. The output of the power amplifier was fed into the transmit transducer, as well as an oscilloscope for monitoring.

The receive transducer was a bk8103 hydrophone, omnidirectional in its xy plane to within ±2dB. (See Figure (4.7a).) This was input to a passive, nine pole Butterworth filter cornered at 250kHz. The filter was required to reduce the level of the backscattered primaries which would otherwise overload the amplification circuitry at a later stage in the receive

electronics[4]. The output of the Butterworth filter was fed into a Brookdeal amplifier on which the gain could be varied from 30dB to 100dB in 1dB increments. Once amplified, the signal was fed into an active bandpass filter. The filter, centred on the frequency of the backscattered signal, further attenuated the primaries and reduced any low frequency noise contaminating the received signal. The output of the bandpass filter was fed in parallel into an oscilloscope for monitoring and a transient recorder for digitization. The transient recorder stored the returned signal as 4096 digitized samples at an amplitude resolution of eight bits. Sampling at a rate of .2μsec, prevented aliasing problems at all frequencies of interest and successive time averages attained the required Signal-to-Noise ratio. The signal was then transferred to the hp9825 computer and stored on cassette tape for future analysis.

4.3.2 Backscatter From a "Smooth" Sand Volume

The volume backscatter experiments were performed at third octave intervals over the frequency band of 25kHz-200kHz. No single transducer was available which could cover the entire band, even when operated in the parametric mode. Instead, a 500kHz transducer (nominal) was used as the parametric source for the band, 25kHz-100kHz and a 900kHz transducer (nominal) was used as the parametric source for the band, 100kHz-200kHz. The overlap at 100kHz provided a check that the backscatter

---

[4]A passive filter was required because the scattered signals of interest were of such small level that electrical nonlinearities inherent in "off the shelf" active filters, might be mistaken for the scattered signals of interest.

measurements were independent of the transducer used. Both transducers were 2.5cm in radius.

The hydrophone was fixed adjacent to the transducer so that it received backscattered signals in its omnidirectional plane. Both sensors were mounted to the base of the central gantry column as depicted in Figure (4.7b). Backscatter measurements were taken over the range of grazing angles, 10° to 25° in 5° increments and 35° to 85° in 10° increments. A normal incidence measurement was taken for completeness, although it was expected that specular reflection would dominate this return.

For an unterminated array, the axial intensity of the difference frequency rises smoothly with range from the parametric source, levels off and then begins to fall smoothly. This can be explained qualitatively as follows: as the range increases, there are more virtual sources contributing to the array gain. Eventually, spherical spreading of the primary signals (limiting their non-linear interaction) and absorption of the primary and difference signals outweigh the gain due to increased array aperture. From this point onward, the intensity begins to fall. The range, L_m, at which the maximum signal level of the difference frequency occurs, is given by the inequality [76] :

$$0.6\pi a^2/\lambda_p \leq L_m \leq 0.8\pi a^2/\lambda_p \qquad (4.6)$$

where 'a' is the transducer radius and λ_p is the arithmetic mean of the primary wavelengths. Inequality (4.6) was used as a rough guide to calculate the optimum length for the terminated array. (In the present experimental setup, array termination was automatically provided by the sand bottom.) For the 900kHz

transducer, we obtain 70cm ≤ L_m ≤ 100cm. For grazing angles of 10° to 45°, the straight line distance from the face of the 900kHz transducer to the sand was maintained at 100cm.[5] Due to depth limitations of the laboratory tank, the range had to be reduced to 70cm for grazing angles of 55° to 90°.

In the case of the 500kHz transducer, Inequality (4.6) yields 40cm ≤ L_m ≤ 55cm. The straight line distance from the face of the 500kHz transducer to the sand was maintained at 70cm for all grazing angles. This was reasonably close to the optimum length and allowed for easy comparison with results obtained using the 900kHz transducer at the steeper grazing angles.

After setting the grazing angle and range, a pulse was transmitted from the transducer. The pulselength was chosen to be as close to 50μsec as possible, and still consist of an integral number of modulated wavelengths. This resulted in transmitting pulses ranging from 40μsec to 60μsec. The return signal was timegated to pass 100μsec beginning at the onset of the first volume return. This permitted backscatter analysis from two, 50μsec "chunks" of the bottom. After taking 100 time averages of the backscattered signal, the result was recorded. The (x,y) coordinates of the source/receiver were then altered so as to insonify a separate patch of sand and the process was repeated. In all, sixteen independent patches were insonified for each grazing

---

[5] Choosing the upper limit of Inequality (4.6) increased the validity of any far field assumptions that might have been employed in the modelling, with regard to the parametric source. In the event, none were necessary as the assumption of an incident plane wave proved adequate.

angle/frequency combination. This provided a spatial ensemble average of the backscatter. Roughly the same sixteen patches of sand were insonified for each grazing angle/frequency.

It was necessary to ensure that the data recorded at shallow grazing was acoustic backscatter and not background noise. To do this, the source/receiver was rotated to 0° grazing and the backscatter experiment was repeated. By taking measurements with the source/receiver placed at the same sixteen (x,y,z) coordinates used in the 10° grazing experiment, the background noise could be compared directly to the results of the 10° backscatter experiment. This experiment was done at octave frequencies from 25-200kHz. To check the results of the 15° backscatter experiments, the 0° grazing experiment was repeated at the sixteen (x,y,z) coordinates corresponding to 15° grazing, again at octave frequencies from 25-200kHz. Since the background noise measurements at 10° and 15° were the same, within the bounds of experimental error, they were not repeated for steeper grazing angles.

4.3.3 Backscatter From a "Smooth" Sand Surface

By simply examining the signals scattered from the layered sand, it isn't possible to distinguish between backscatter from the bottom volume and backscatter from the bottom surface. For this reason, an experiment was performed to estimate the component of backscatter measured, resulting from bottom roughness. A two-dimensional scattering surface was constructed using a piece of 2cm thick PVC approximately $1m^2$. The PVC was made a pressure release surface by gluing to it, a 3mm thick neoprene sheet. The surface was placed in the water

and covered with a 7mm layer of 130μm sand. The sand was smoothed so as to resemble the top layer of sand used in the volume scattering experiment.

With the 900kHz transducer operating in parametric mode, backscatter from the PVC surface was measured. The measurements were taken from 100kHz-200kHz at third octaves, at grazing angles of 35° to 85° in 10° increments, as well as at normal incidence. The procedure followed for the volume backscatter experiments was adhered to. This allowed direct comparison of the surface backscatter results with the volume backscatter results made previously.

4.3.4 Measurement of Incident Intensity

The standard definition of the surface backscattering coefficient, σ_s, is:

$$\sigma_s = I_s \cdot r^2 / I_0 \cdot A \qquad (4.7)$$

where 'A' is the area of the insonified patch of surface, usually taken to the -3dB points, I_s is the intensity of the backscattered wave measured a distance r from the surface, and I_0 is the intensity of the incident wave measured at the scattering patch. The definition of the volume backscattering coefficient, σ_v, is similar:

$$\sigma_v = I_s \cdot r^2 / I_0 \cdot V \qquad (4.8)$$

where the area insonified is replaced by the volume insonified, V; the other terms remaining the same.

Equations (4.7) and (4.8) each require the incident intensity, including the -3dB beam width, at the point of insonification. Measuring this for the exact experimental setup was not feasible, as scatter from the inhomogeneous medium immediately below would interfere. Instead, an estimate of the incident intensity was obtained as follows:

(a) Beam Calibration of the Untruncated Array

The bk8103 hydrophone used as the receiver in the backscatter experiments was removed from the source/receiver mount and replaced by a second, physically identical hydrophone. This "dud" hydrophone, was not connected electrically. The source/"dud" was placed in an open area of the large tank, well removed from any source of scatter or reflection. The bk8103 receiver hydrophone was fixed to a small, manual gantry 70cm away, at the same depth as the source/"dud". The source/"dud" was then moved in 2cm horizontal increments so that the parametric beam swept the receiver and the difference frequency intensity was measured. This was done at each difference frequency using the appropriate source transducer. The process is shown schematically in Figure (4.8a). The procedure was then repeated for a separation of 100cm. By fixing the "dud" hydrophone to the source, any anomalies in the beam pattern caused by the receive hydrophone's presence during the backscatter experiments would be recorded. Using the same receiver for both backscatter and calibration experiments made absolute calibration of the source-receiver unnecessary.

(b) Beam Calibration of the Truncated Array

As previously noted, the sediment provides an unavoidable termination of the parametric array. Terminating the array acts to widen the beamwidth. To insure that this did not have too significant an effect on the area insonified, the beam calibrations were repeated with the array truncated. Truncation was achieved by inserting a low pass acoustic filter between the receiving hydrophone and the parametric array, transverse to the acoustic axis. The difference frequency passed through virtually unattenuated, whereas the primaries were reduced by approximately 15dB for the 500kHz array and 30dB for the 900kHz array. The filter was composed of polypropylene and measured 1cm thick by $1m^2$. A plot of the transmission of the acoustic filter as a function of frequency is given in Figure (4.12) [77].

Beam calibration of the truncated array was performed with the acoustic filter at ranges of 70cm and 100cm from the parametric source; the distances corresponding to the ranges used in the backscatter experiments. In both cases, the receiving hydrophone was placed immediately behind the acoustic filter. A schematic of the experimental arrangement is shown in Figure (4.8b).

(c) Range Calibration of the Untruncated Array

Again, the source/"dud" was placed in an open area of the large tank, with the receiver fixed to the small, manual gantry 50cm away, on the beam axis of the source/"dud". The "on axis" intensity at the difference frequency was measured at 10cm increments up to a range of 120cm. This span included all ranges

used in the backscatter experiments and provided a check on Inequality (4.6) as to the location of the peak intensity of the difference frequency. The experimental arrangement is shown schematically in Figure (4.9a).

(d) Range Calibration of the Truncated Array

Truncating a parametric array results in a significant decrease in acoustic intensity axially, past the point of truncation [78]. This is in contrast to the gentle rise, flattening off, and then gentle fall, of axial intensity vs. range for the unterminated array. To examine the effect of truncation on the axial intensity, a range calibration experiment was performed on the truncated array. Once again, the acoustic filter was inserted between the receiving hydrophone and the parametric array, transverse to the acoustic axis. With the truncation fixed at 70cm, the hydrophone was placed on axis, and intensity measurements were taken in the range of 75cm to 140cm from the parametric source. Next the truncation was fixed at 100cm and intensity measurements were taken in the range of 105cm to 140cm from the parametric source. A schematic of the arrangement is shown in Figure (4.9b).

4.3.5 Estimate of Horizontal Inhomogeneity Length Scale

(The Echosounder Experiment)

As noted earlier, to obtain an estimate of volume backscatter we require the length scale of the vertical and horizontal concentration fluctuations in the bottom. A reasonable estimate of the vertical correlation length can be made based on the layer thickness used in the model volume. The horizontal correlation length is less obvious. However, note that the

Rayleigh reflection coefficient is a function of density which, as we have already mentioned, is closely related to concentration. (The relationship between these parameters is discussed in Appendix C.) Therefore, measuring the reflection coefficient as a function of position can be used to obtain a rough estimate of the horizontal correlation length of the concentration fluctuations .

The transmit and receive electronics used in the echosounder experiment are depicted schematically in Figure (4.10a,b). A 500kHz transducer was used as source and receiver and operated linearly, rather than parametrically. A linear oscillator generated a 500kHz toneburst which was fed directly into the attenuator. The output of the attenuator was input to the 200W ENI power amplifier. The output of the power amplifier was fed into a transmit/receive switch and the "transmit" output of the switch was connected to the transducer. The output of the ENI amplifier was monitored on an oscilloscope.

The "receive" output of the transmit/receive switch was fed into the Brookdeal amplifier. Once amplified, the signal was fed in parallel into an oscilloscope for monitoring and the transient recorder for digitization. A sampling rate of .05μsec was selected providing 40 data points/wavelength at 500kHz.

The measurement of the reflection coefficient was performed as follows. A 500kHz circular transducer of 1.5cm radius was fixed to the armature at the base of the gantry's central column. The transducer was directed at normal incidence to the sand volume and positioned to one corner, arbitrarily chosen to be (x,y)=(0,0). The perpendicular distance from the transducer face to the sand surface was set to 8cm. This provided

a very small spot size to get maximum resolution of the reflection coefficient. A 500kHz tone burst of 40μsec duration was transmitted and the return echo was time gated and stored on digital tape for processing at a later time. The transducer was moved 0.5cm in the x direction and another pulse was transmitted, the echo received and again stored on tape. This was repeated at 0.5cm intervals across the width of the scattering volume. The transducer was reset to (x,y)=(0,10cm) and another horizontal sweep was made. In all, four such sweeps were made; at y= 0cm, 10cm, 20cm, and 30cm. The transducer was reset to (x,y)=(0,0) and a series of 4 sweeps were performed in the y direction at x= 0cm, 10cm, 20cm, and 30cm. Sweeping in both directions provided a check to see if there was horizontal directionality in the correlation.

Storage of the entire echo signal would represent a significant amount of tape space since it had to be repeated at each grid point over the surface. The data was therefore reduced in the following way. Only the reflection coefficient was of interest. This was obtained by averaging several maxima (and minima) in the steady state region of the echo. (See Figure (4.11).) This average was normalized by the reflection coefficient obtained from the water/air interface which has a reflection coefficient very close to unity. The echo returned from the water/sand interface, now reduced to a normalized reflection coefficient, was stored on cassette tape for future analysis.

A 40μsec pulse corresponds to a penetration depth of about 30mm so that it provided a horizontal correlation length averaged over several layers of sand. To see if the correlation length

differed when a single layer was insonified, the experiment was repeated with a 10μsec pulse. This corresponds to a penetration depth of about 7mm or only the surface layer.

This completes the description of the experiments. We now turn to an examination of the data obtained.

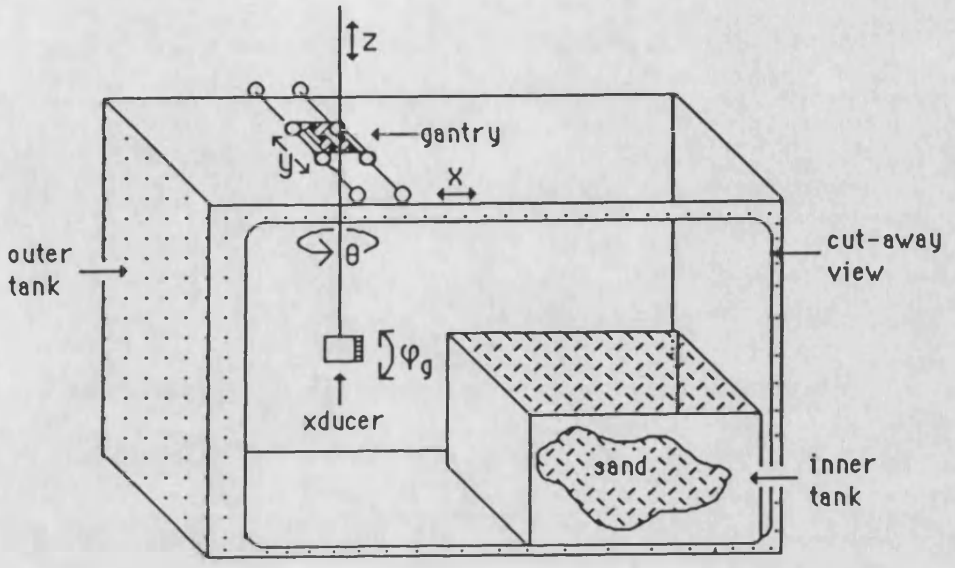

Figure (4.1): Experimental tank and gantry system.

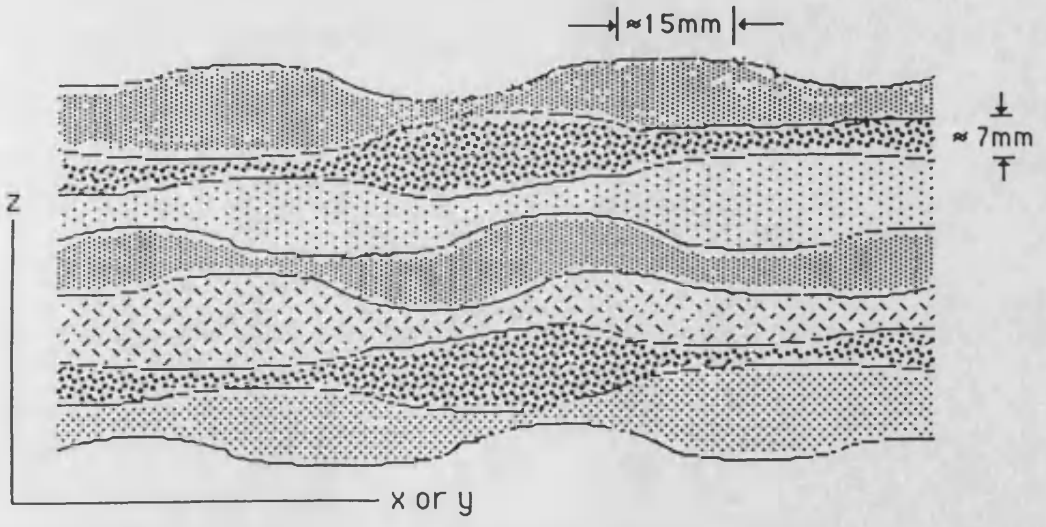

Figure (4.2): Cross section of several sand layers, with exaggerated view of layer thickness variations.

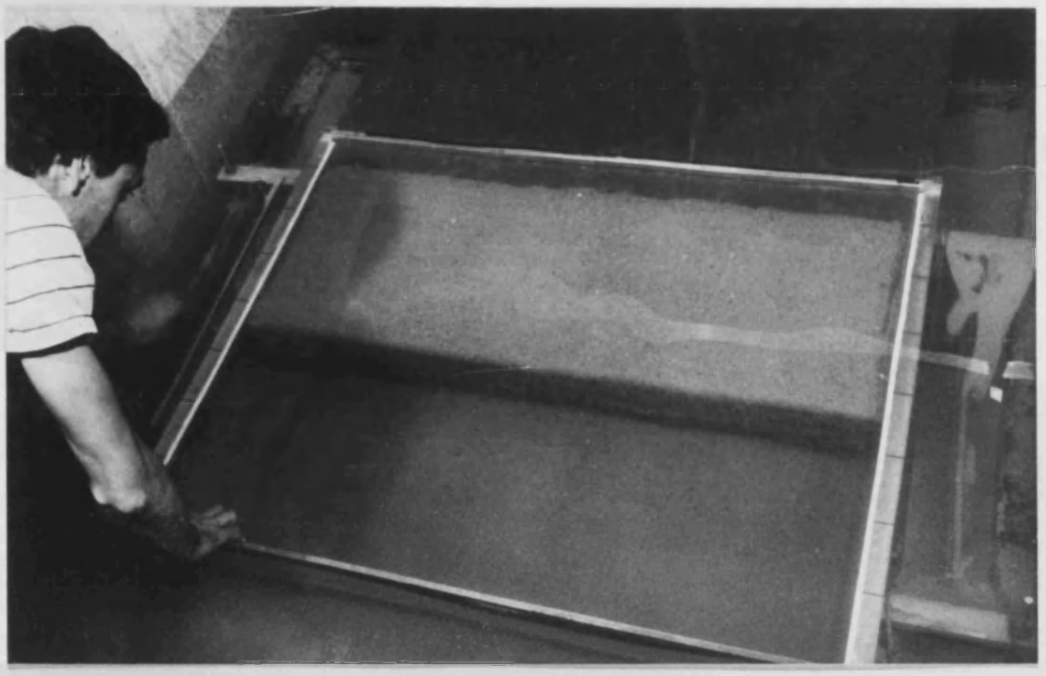

Figure (4.3): Photograph of Sandlayer in operation.

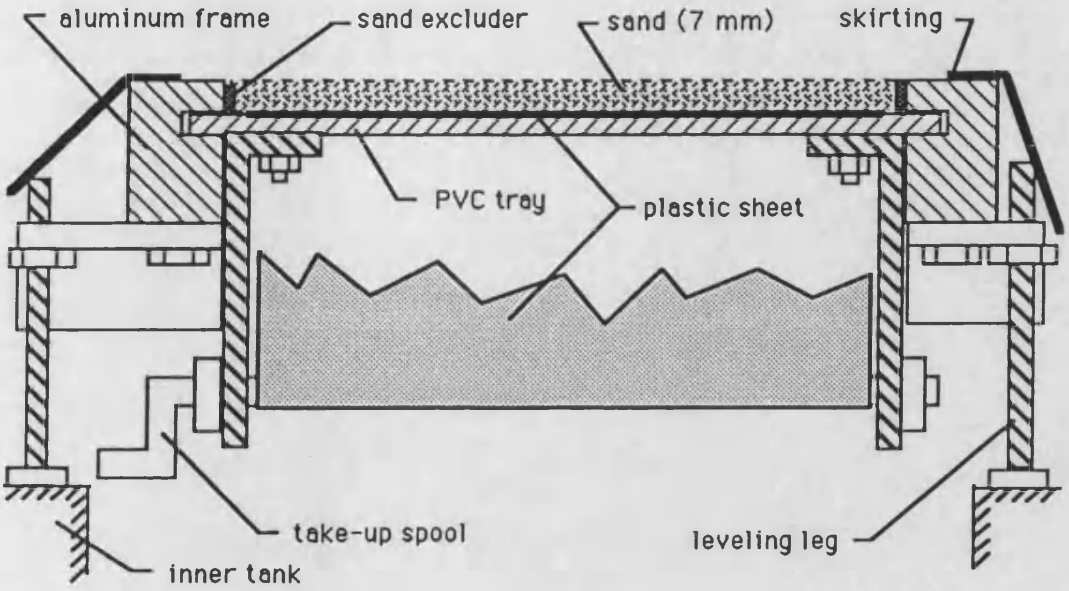

Figure 4.4: Schematic of Sandlayer.

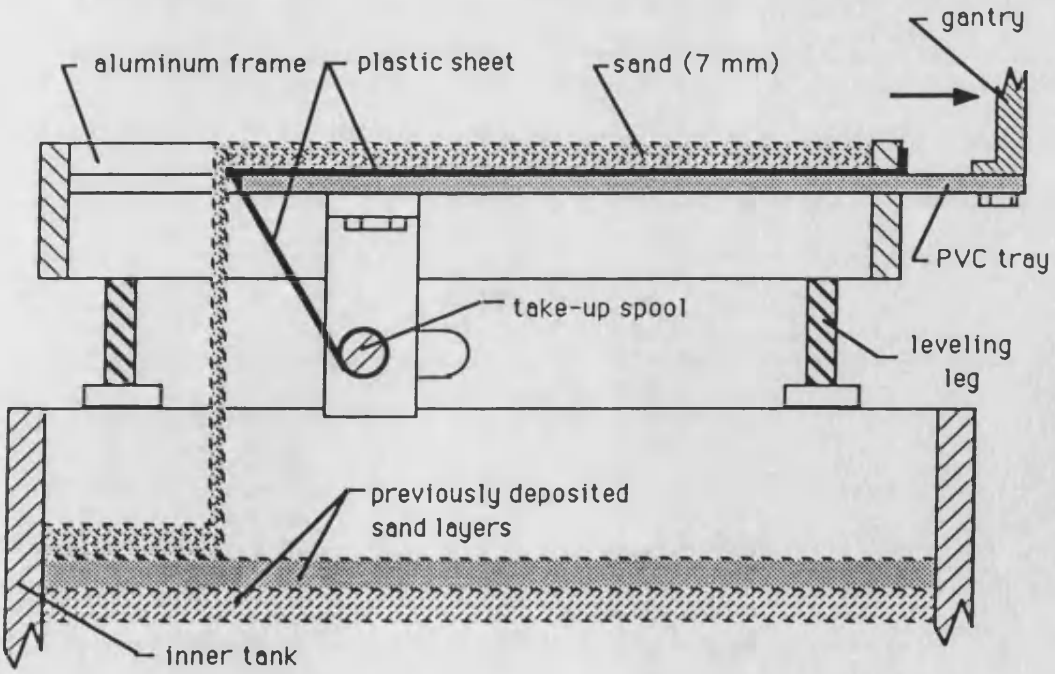

Figure 4.5: Sandlayer in operation.

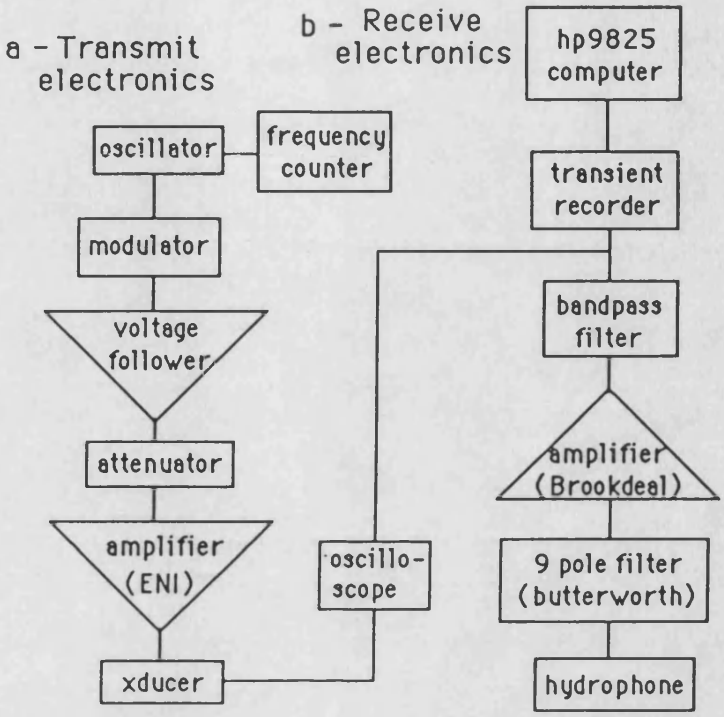

Figure (4.6): Block diagram of electronics used in backscatter experiments.

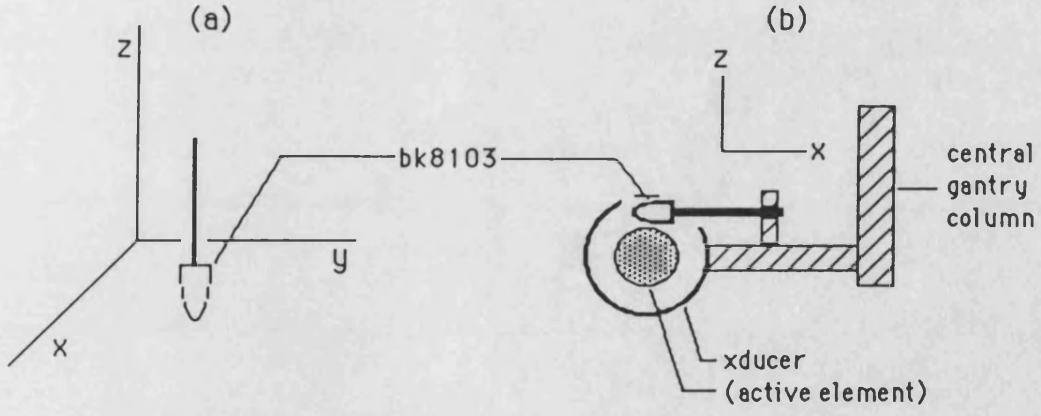

Figure (4.7): (a) Coordinate system showing omnidirectional (xy) plane of bk8103. (b) sensor positions for backscatter experiments.

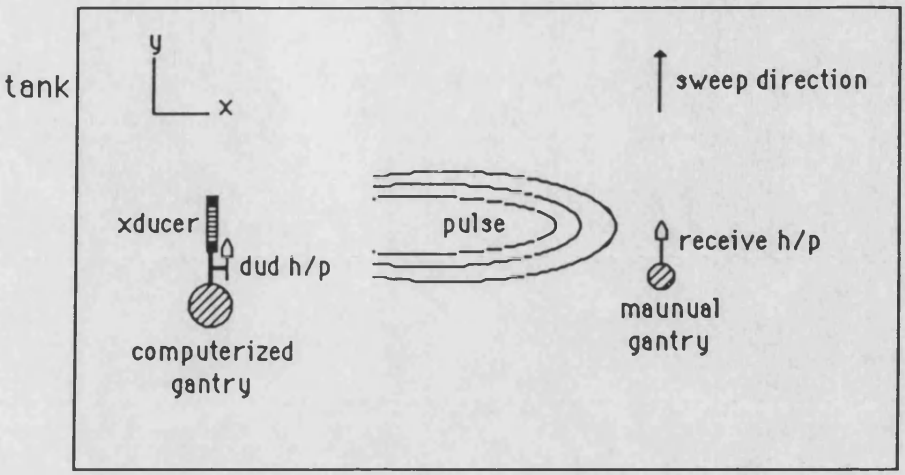

Figure (4.8a): Plan view of tank showing geometry for beam calibration of untruncated parametric array.

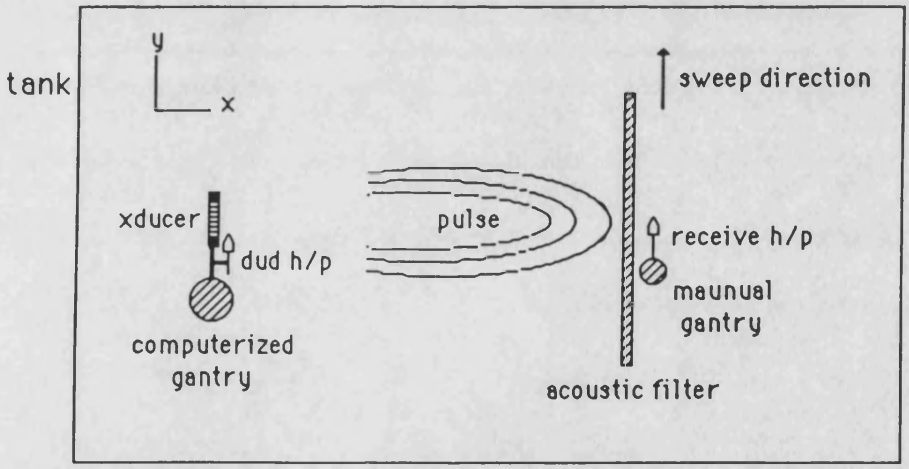

Figure (4.8b): Plan view of tank showing geometry for beam calibration of truncated parametric array.

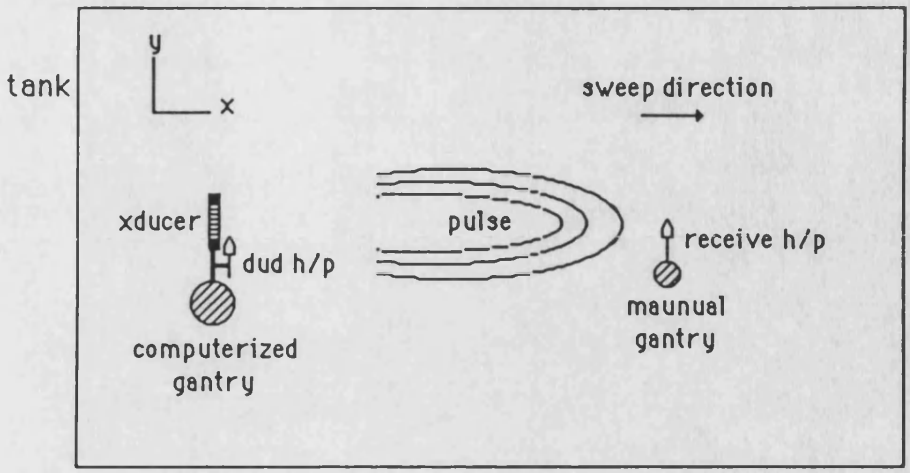

Figure (4.9a): Plan view of tank showing geometry for range calibration of untruncated parametric array.

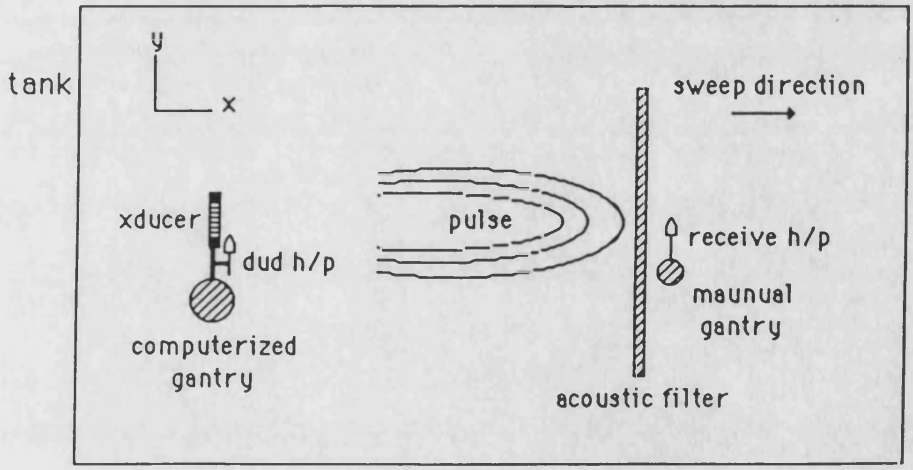

Figure (4.9b): Plan view of tank showing geometry for range calibration of truncated parametric array.

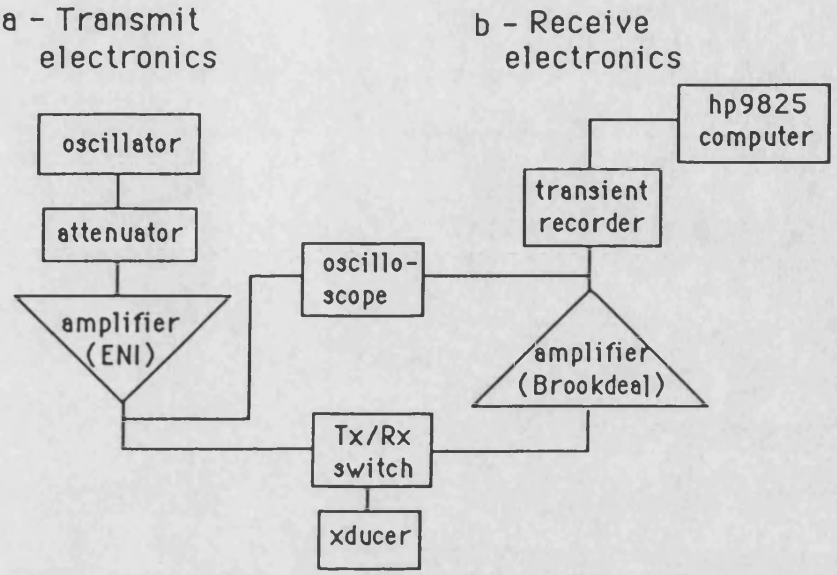

Figure (4.10): Block diagram of electronics used in echosounder experiment.

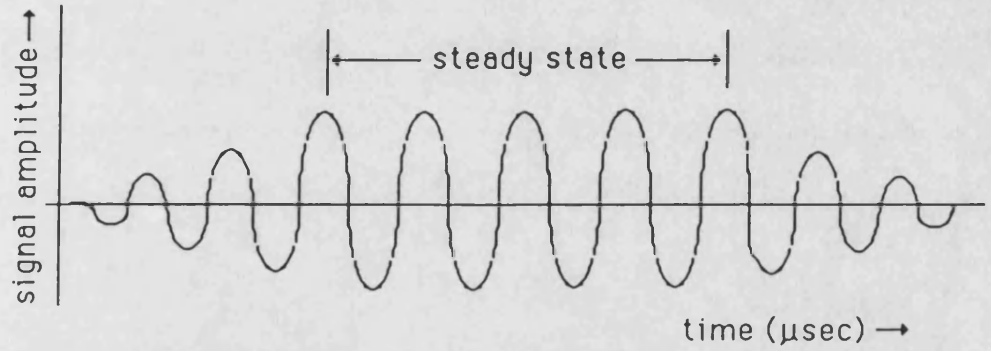

Figure (4.11): Typical echo returned from sand in echosounder experiment.

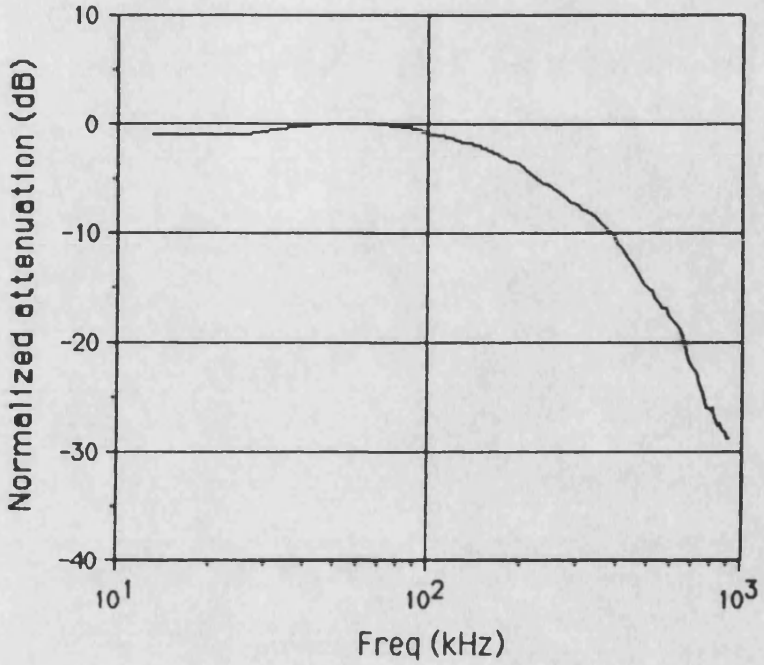

Figure (4.12): Normalized plot of transmission through acoustic filter.

CHAPTER 5

EXPERIMENTAL RESULTS

In this chapter, experimental data obtained from the experiments discussed in Chapter 4 are presented. Full discussion of the data, as well as comparison with the model, is deferred to Chapter 6.

5.1 Data Analysis System

Data analysis was performed using an Apple MacIntosh® computer. The data was transferred from the hp9825 to the MacIntosh, via an RS232 serial bus. The fast Fourier transform (FFT) was employed when converting time series data to the frequency domain. In the case of backscatter returns, the time series data was broken into 50μsec "chunks" (256 points) and combined with an additional 256 points of zero packing to improve resolution. The data presented is from the first 50μsec return.

5.2 The Calibration Data

Figures (5.1) to (5.3) contain a summary of the range dependence experiments for the parametric array. Conversion of measured voltage to absolute intensity level in dB re $1\mu Pa^2/Hz$, is based on the manufacturers specification for the receiving hydrophone, which is quoted to be accurate within ±2dB. The solid line is a visual best fit drawn for clarity. Note that here and elsewhere, we shall use the terminology 100kHz'a' to refer to data obtained with the 900kHz parametric array and 100kHz'b' to refer to data obtained with the 500kHz array. In Figure (5.1), the untruncated case, the peak in the data obtained using the 900kHz array occurs at a transducer-receiver separation of about 80cm.

This falls within the limits established by Inequality (4.6). The peak in the data obtained using the 500kHz array appears to occur at a separation of slighlty less than 50cm. This too, falls within the limits of Inequality (4.6). For the truncated array, the intensity falls rapidly past the point of truncation as expected. This is clearly shown in Figures (5.2) and (5.3).

A summary of the beam calibration experiments, both untruncated and truncated, are contained in Figures (5.4) to (5.7). The -3dB points, required in the definition of surface backscattering strength, can be obtained directly from the figures.

5.3 The Volume Backscatter Data

The ratio of backscattered to incident intensity (I_s/I_0) for the volume backscatter experiments is shown in Figure (5.8), plotted as a function of frequency. The figure contains data for grazing angles of 20°, 45°, and 90°. The dependence of I_s/I_0 on grazing angle, for the same experiment is contained in Figures (5.9) and (5.10). Figure (5.9) shows the data obtained at frequencies of 25, 50 and 100kHz'b' using the 500kHz parametric array. Figure (5.10) shows the data obtained at 100kHz'a' and 200kHz using the 900kHz parametric array. Repeated in Figure (5.10) are the 100kHz'b' results to permit comparison between both sets of 100kHz data.

5.4 The Surface Backscatter Data

The ratio I_s/I_0 for the surface backscatter experiments is shown in Figure (5.11), plotted as a function of frequency. The figure contains data for grazing angles of 65°, 75°, and 85°. The dependence of I_s/I_0 on grazing angle, for the experiment is

contained in Figure (5.12). Shown are data obtained at third octave frequencies from 100 to 200kHz using the 900kHz parametric array.

5.5 The Echosounder Data

The relationship between the Rayleigh reflection coefficient and concentration, formulated in Appendix C, was used to convert the echosounder data to a measure of concentration. The mean value of the concentration was then subtracted out. Performing an autocorrelation on the (now) concentration fluctuation data obtained a horizontal correlation length. Furthermore, the autocorrelation at zero lag provides an experimental estimate of the mean square value of the concentration fluctuations, which is required in the model in Chapter 3.

The autocorrelations of the concentration fluctuations for the four sweeps in the x direction, for the 40μsec pulse, are contained in Figure (5.13). (The x direction is shown in the backscatter geometry of Figure (3.1).) The corresponding data for the four sweeps in the y direction are shown in Figure (5.14). The autocorrelation data in the x and y directions for the 10μsec pulse are contained in Figures (5.15) and (5.16) respectively.

The average of the four data sets of Figure (5.13) is plotted in Figure (5.17). Two more sets of points are obtained by averaging the data of Figures (5.14) and (5.16) respectively. The fourth set of points in Figure (5.17) was obtained by averaging only three of the data sets of Figure (5.15). This was done because one data set in Figure (5.15) appeared to oscillate somewhat wildly and was omitted so as not to bias the average

too strongly. Each of the four data sets contained in Figure (5.17) was normalized with respect to its mean square value and replotted in Figure (5.18).

This concludes the preliminary inspection of the experimental results. We shall now proceed to examine the data in detail, placing particular emphasis on the agreement between the volume backscatter data, and the model derived in Chapter 3.

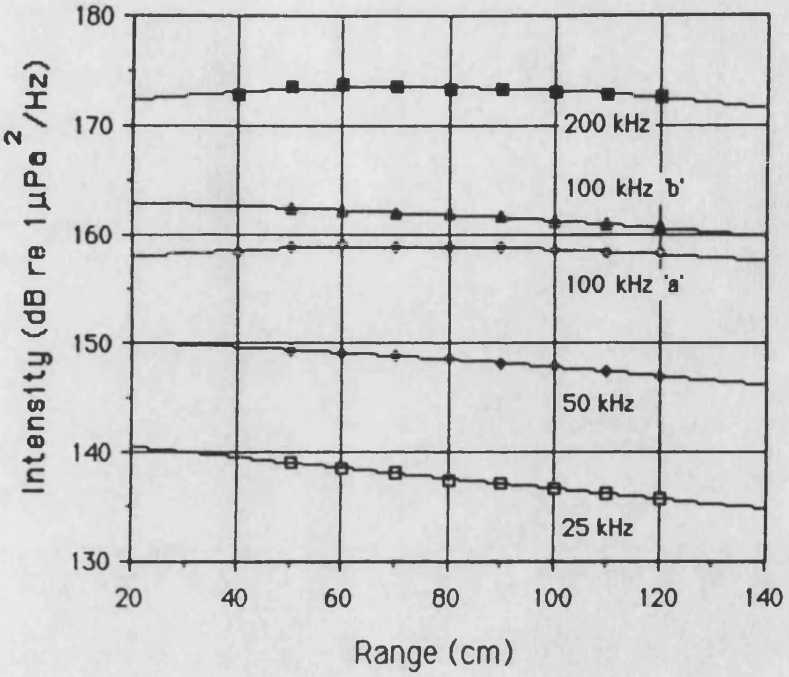

Figure (5.1): Axial range dependence of difference frequency for untruncated array.

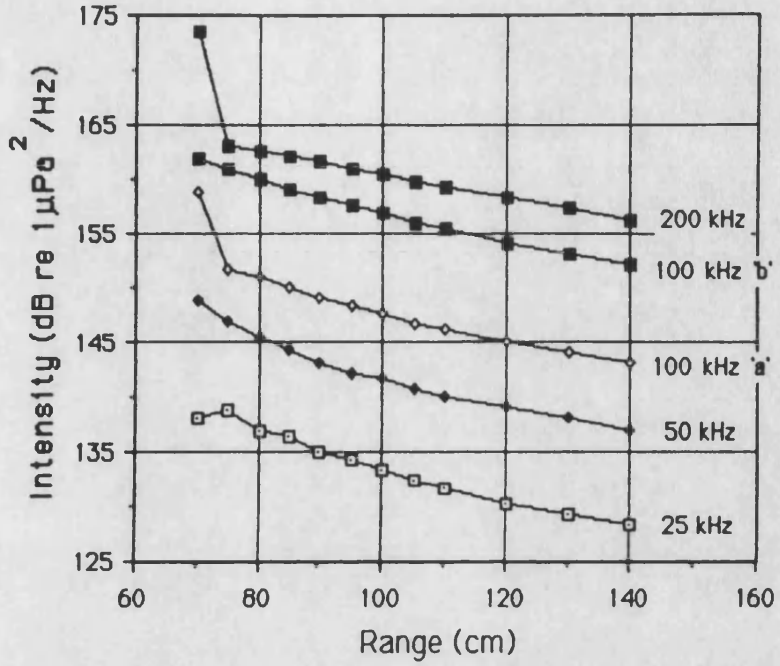

Figure (5.2): Axial range dependence of difference frequency for array truncated at a range of 70cm.

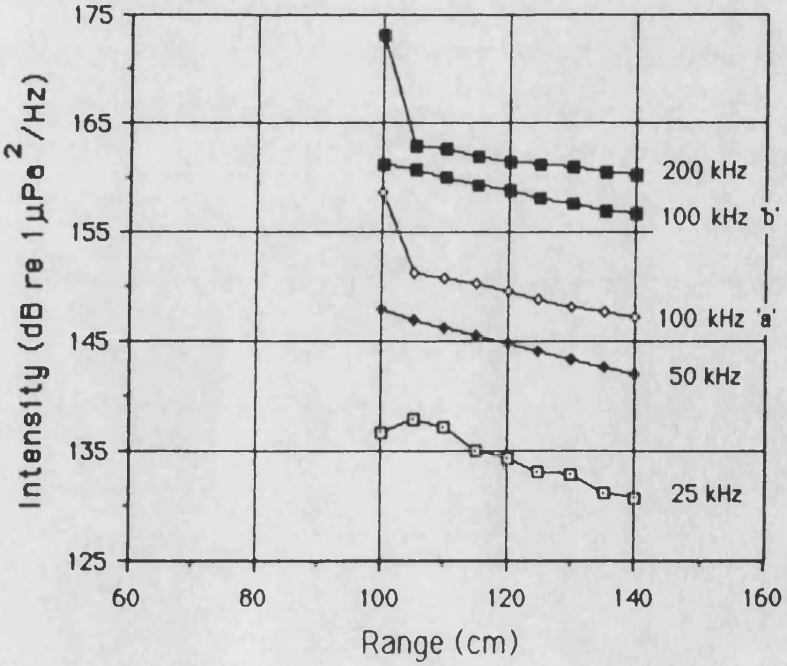

Figure (5.3): Axial range dependence of difference frequency for array truncated at a range of 100cm.

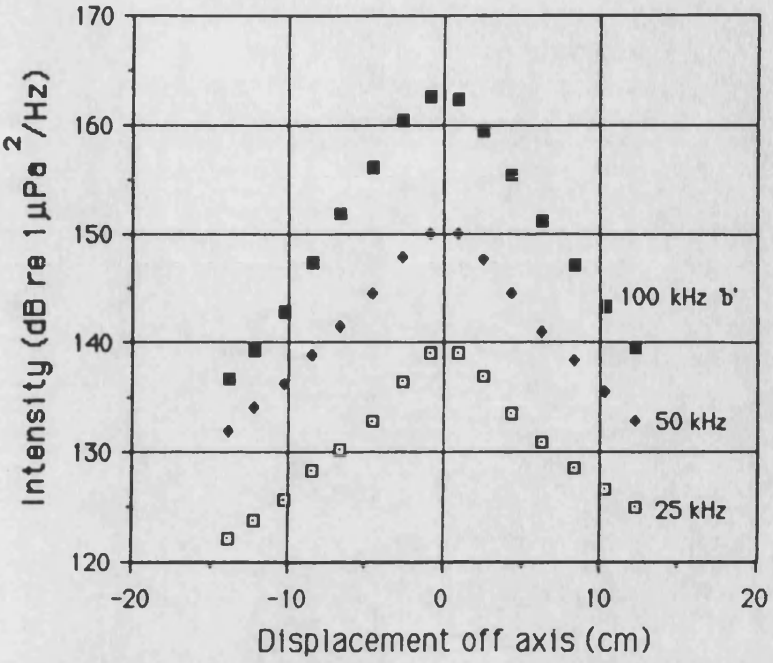

Figure (5.4a): Beam cross-section of difference frequency for untruncated array. Transducer-receiver separation=70cm.

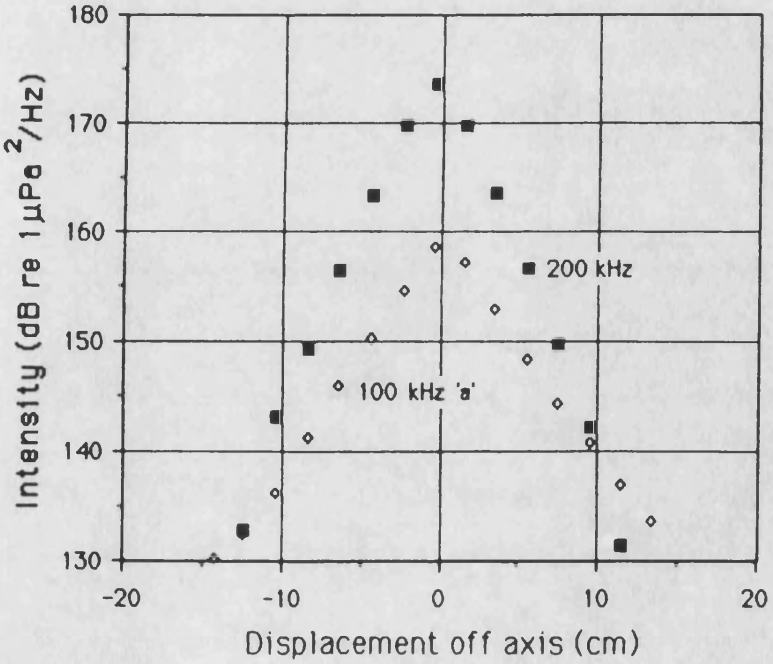

Figure (5.4b): Beam cross-section of difference frequency for untruncated array. Transducer-receiver separation=70cm.

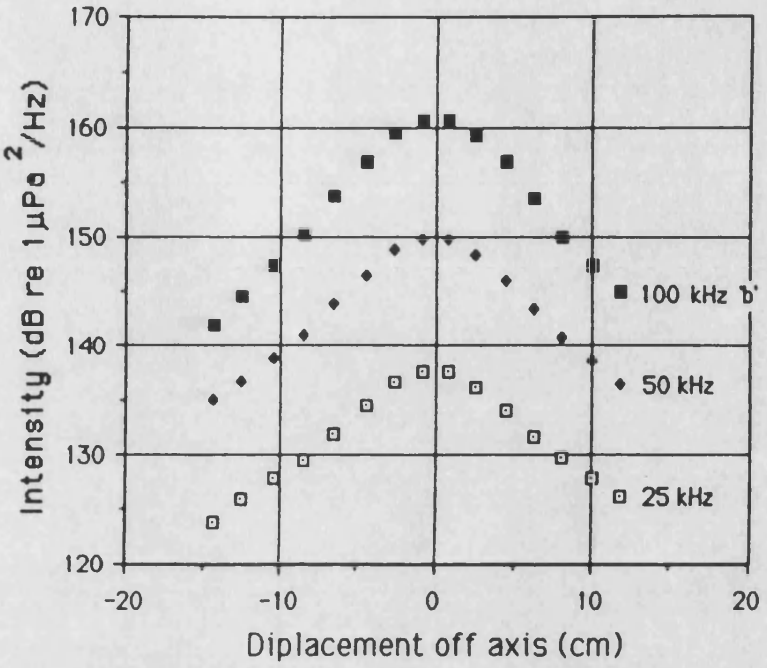

Figure (5.5a): Beam cross-section of difference frequency for untruncated array. Transducer-receiver separation=100cm.

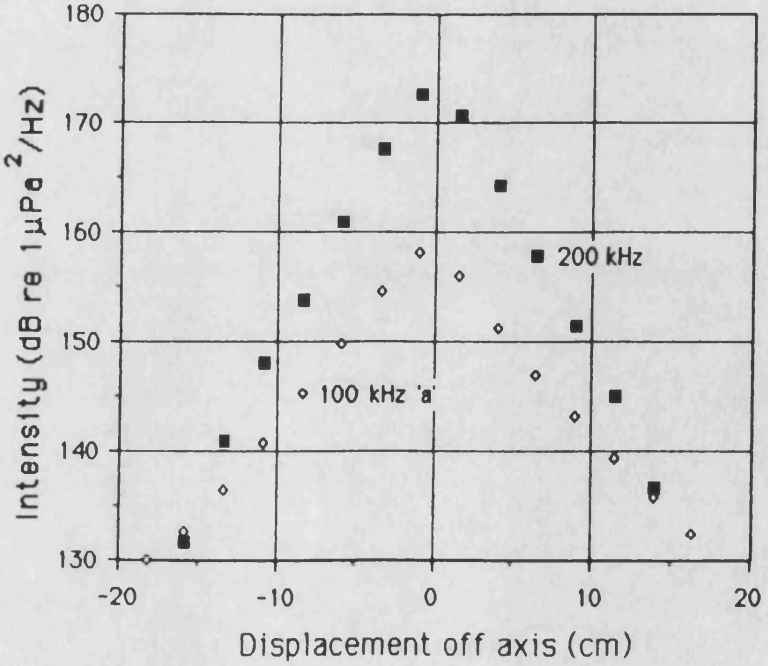

Figure (5.5b): Beam cross-section of difference frequency for untruncated array. Transducer-receiver separation=100cm.

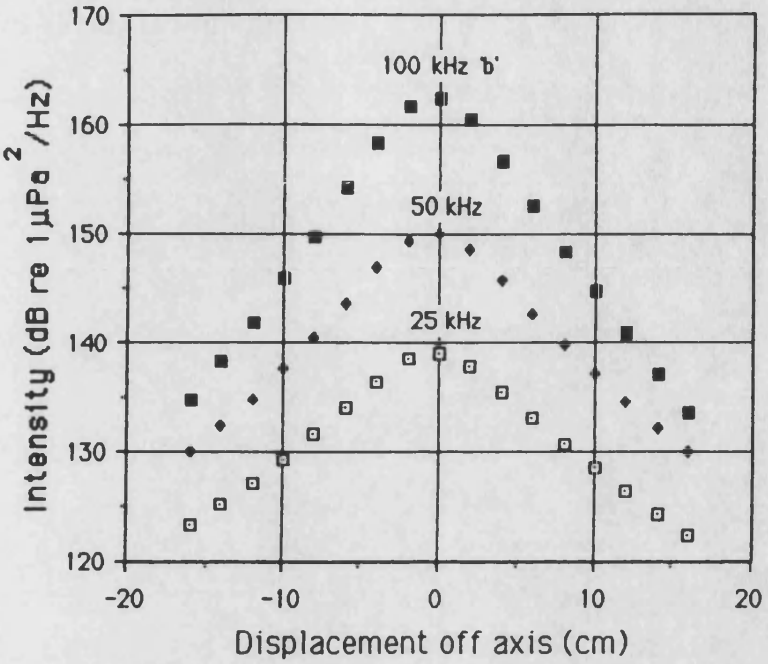

Figure (5.6a): Beam cross-section of difference frequency for truncated array. Transducer-receiver separation=70cm.

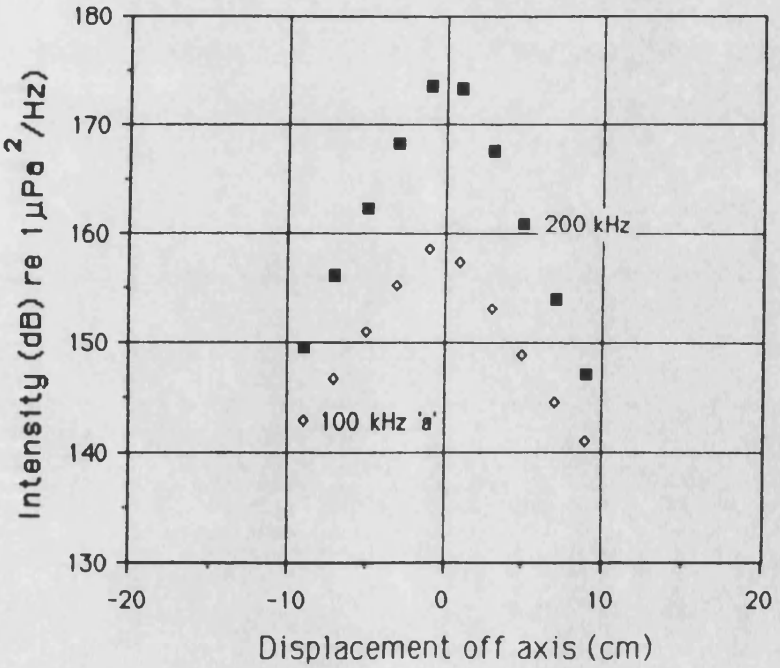

Figure (5.6b): Beam cross-section of difference frequency for truncated array. Transducer-receiver separation=70cm.

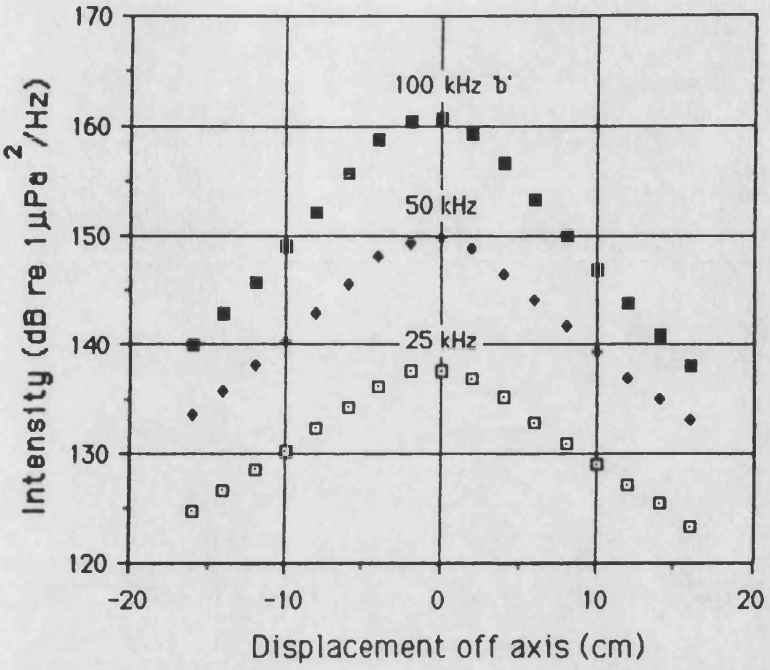

Figure (5.7a): Beam cross-section of difference frequency for truncated array. Transducer-receiver separation=100cm.

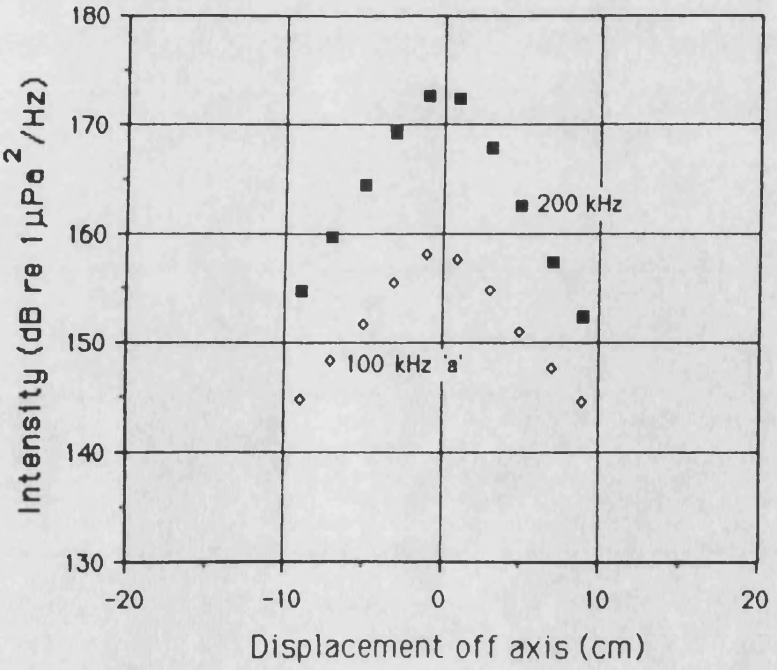

Figure (5.7b): Beam cross-section of difference frequency for truncated array. Transducer-receiver separation=100cm.

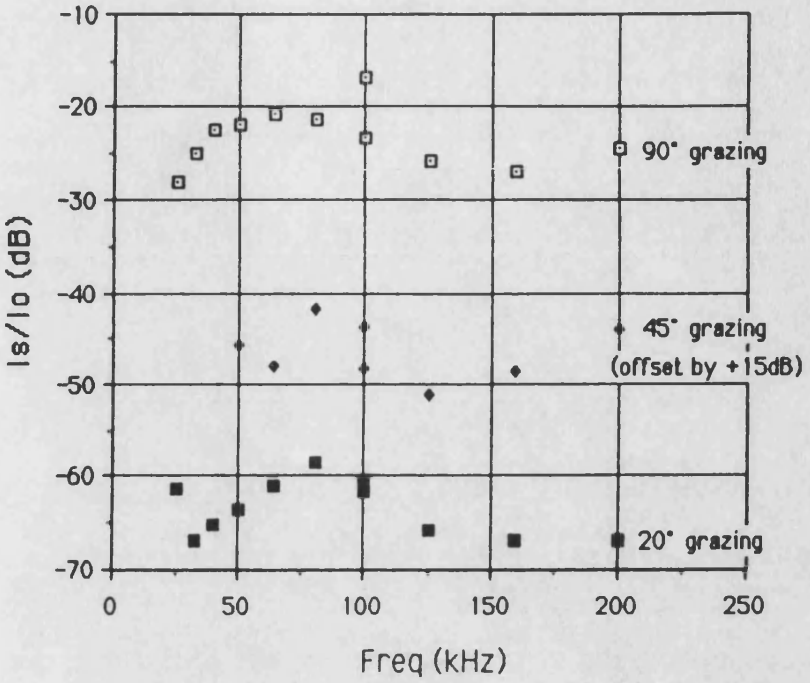

Figure (5.8): Intensity of volume backscattered wave measured at receiver and normalized by intensity incident at surface.

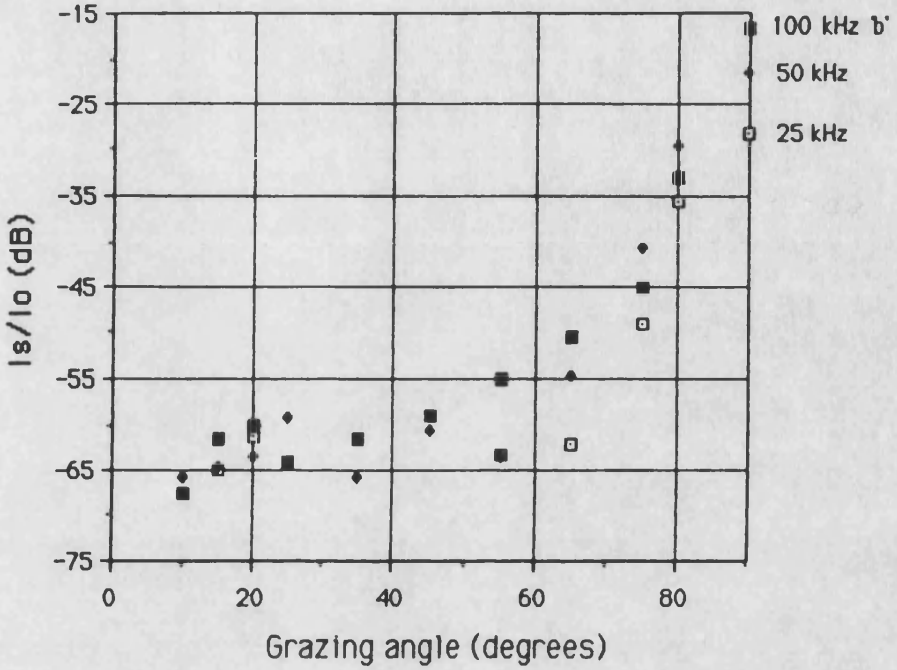

Figure (5.9): Intensity of volume backscattered wave measured at receiver and normalized by intensity incident at surface.

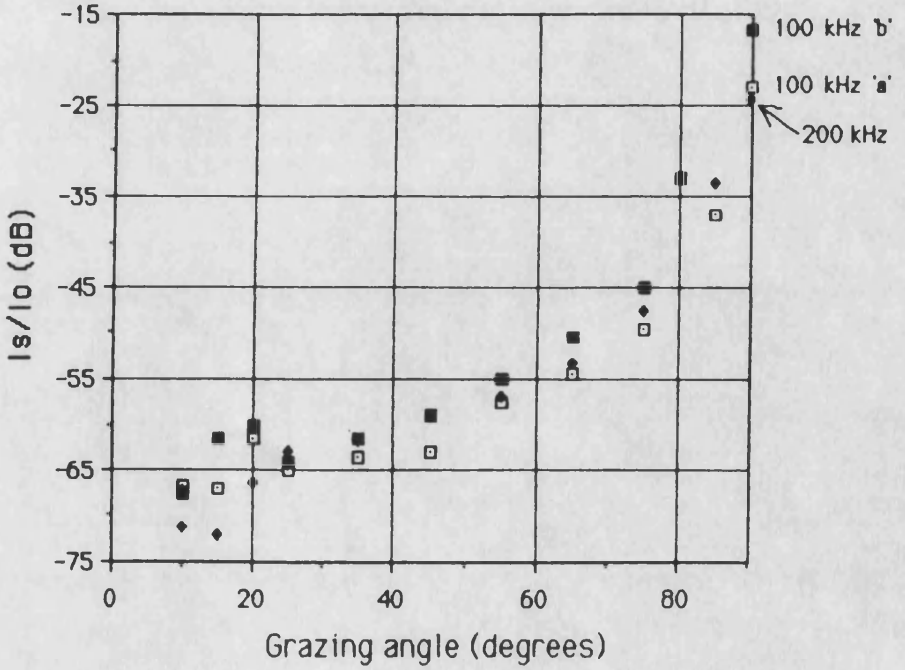

Figure (5.10): Intensity of volume backscattered wave measured at receiver and normalized by intensity incident at surface.

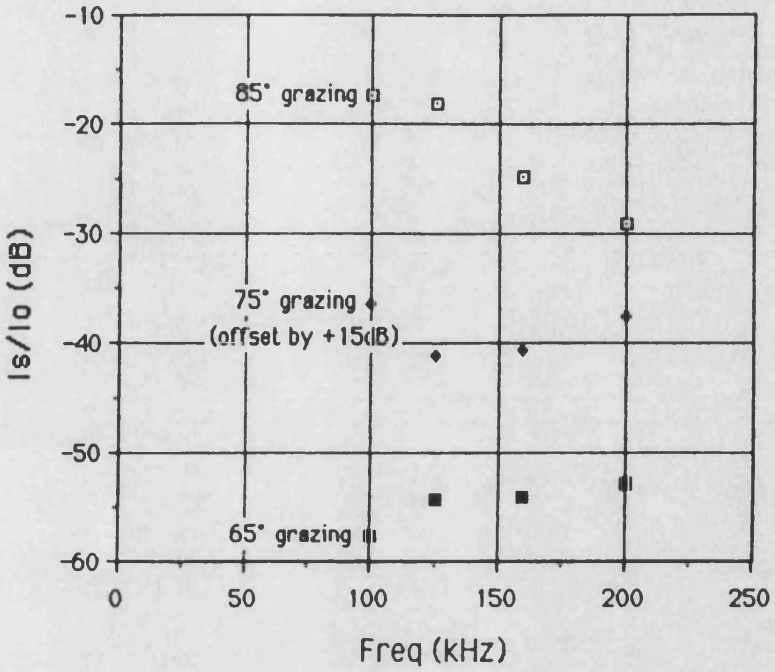

Figure (5.11): Intensity of surface backscattered wave measured at receiver and normalized by intensity incident at surface.

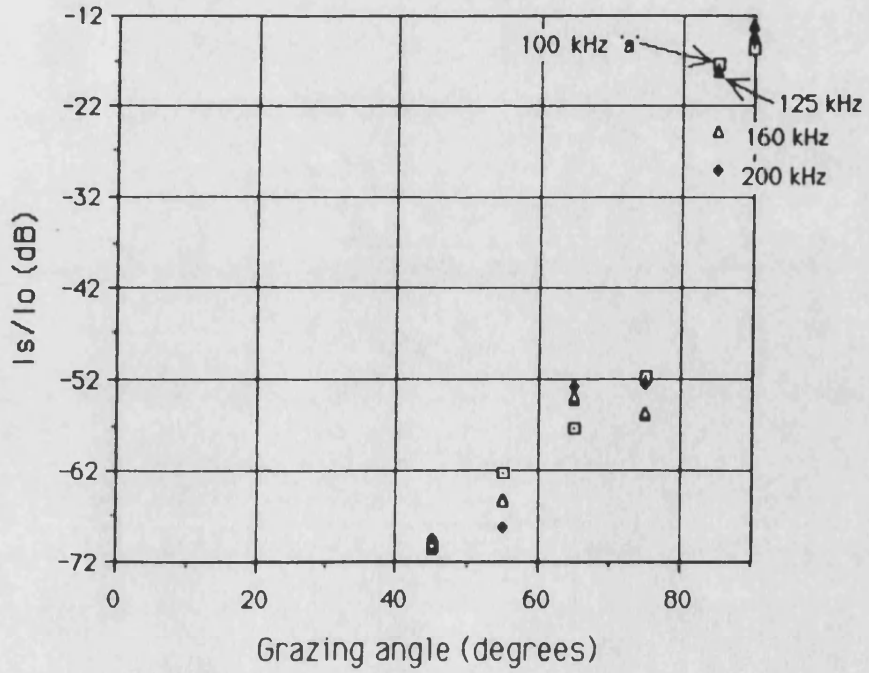

Figure (5.12): Intensity of surface backscattered wave measured at receiver and normalized by intensity incident at surface.

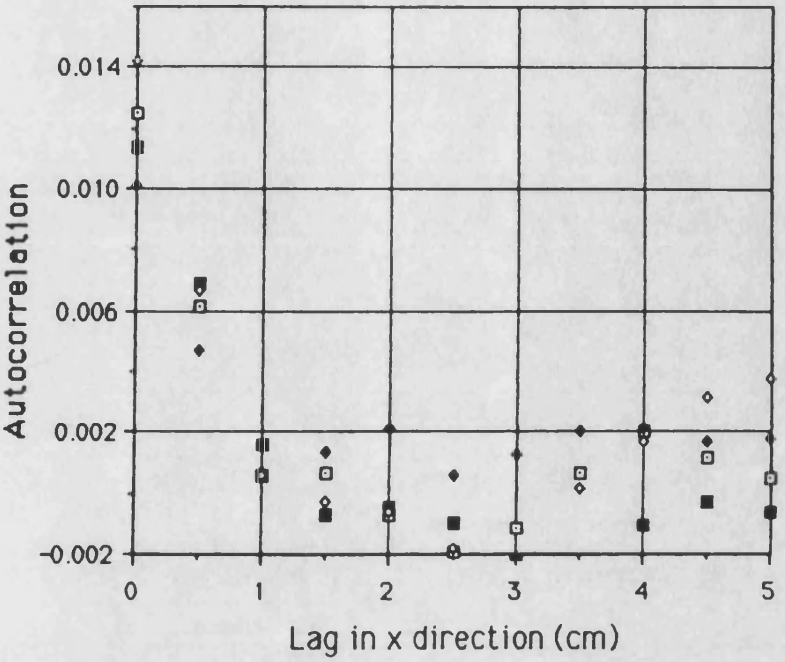

Figure (5.13): Autocorrelation data in x direction for 40μsec pulse. The four sets of points represent sweeps at four values of y.

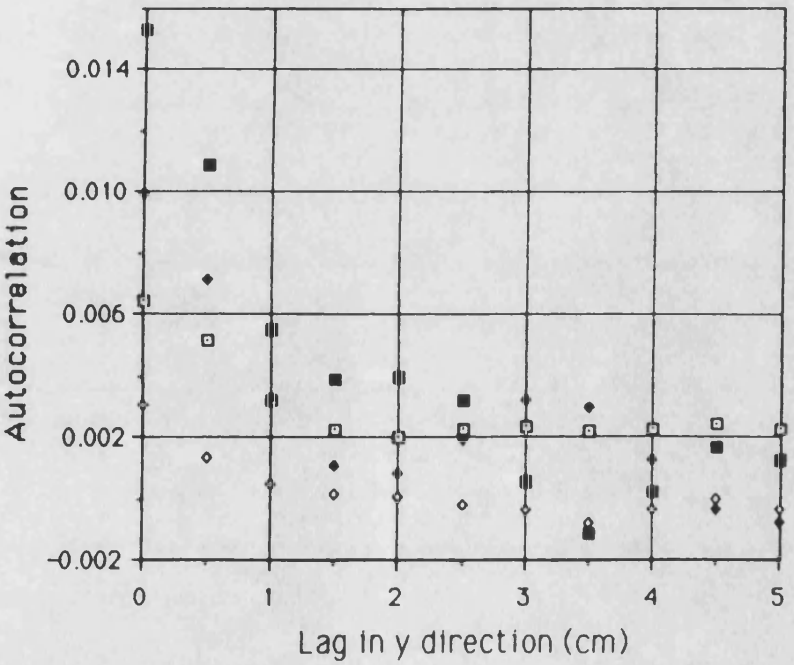

Figure (5.14): Autocorrelation data in y direction for 40μsec pulse. The four sets of points represent sweeps at four values of x.

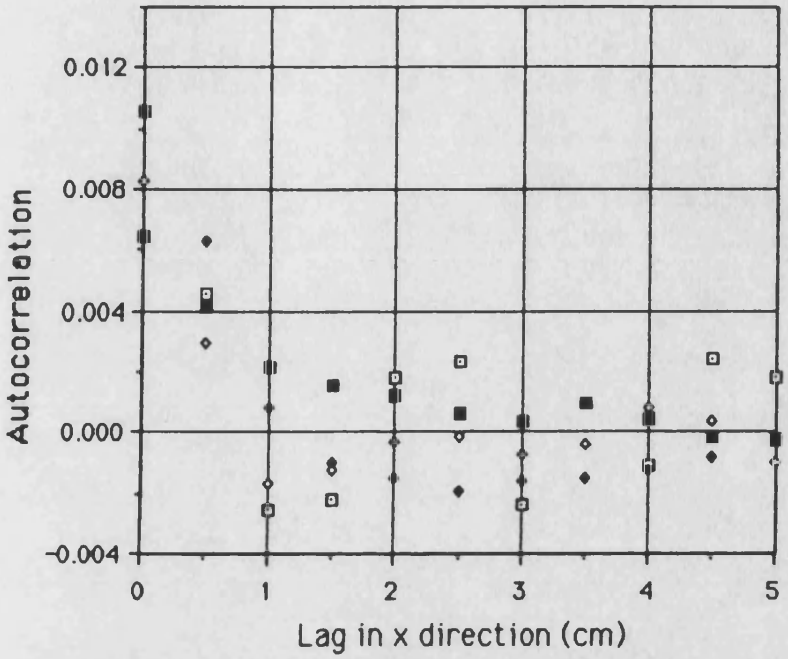

Figure (5.15): Autocorrelation data in x direction for 10μsec pulse. The four sets of points represent sweeps at four values of y.

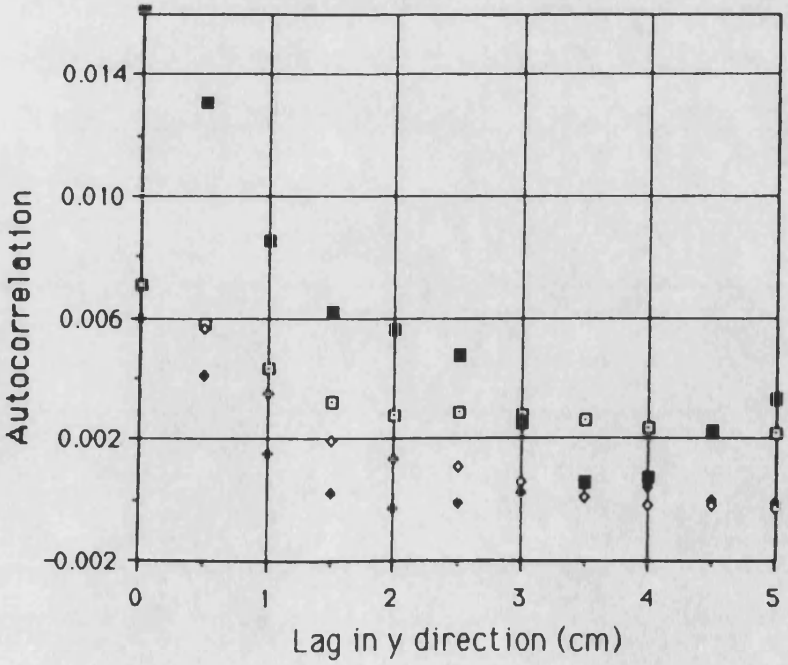

Figure (5.16): Autocorrelation data in y direction for 10μsec pulse. The four sets of points represent sweeps at four values of x.

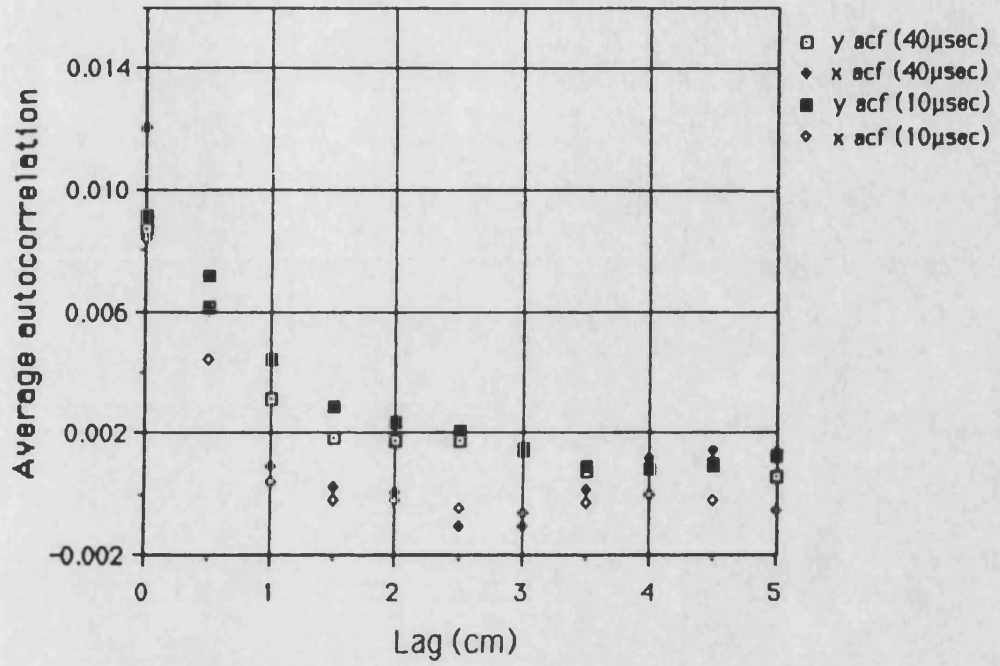

Figure (5.17): Autocorrelation (acf) data. Each set of points represents the average of the data taken for one pulselength and direction.

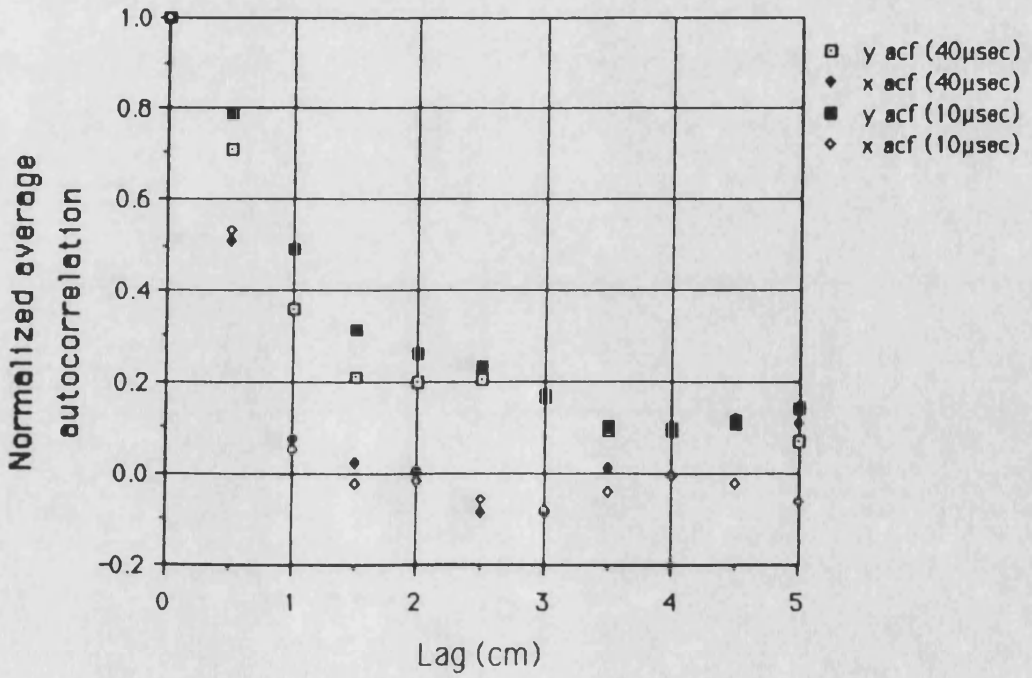

Figure (5.18): Normalized autocorrelation (acf) data. Each set of points represents the average of the data taken for one pulselength and direction.

CHAPTER 6

DISCUSSION: INCLUDING COMPARISON OF MODEL AND DATA

In this chapter, a detailed examination is made of the experimental data presented in Chapter 5. In particular, comparison is made between the volume backscatter data and the theoretical model derived in Chapter 3.

In this and subsequent chapters, backscatter data shall be plotted in terms of the surface backscattering strength, denoted BSS, and defined as:

$$BSS = 10 \cdot \log(\sigma_s) \qquad (6.1)$$

where σ_s, is the surface backscattering coefficient, defined in Equation (4.7). The definition is repeated here for convenience.

$$\sigma_s = I_s \cdot r^2 / I_0 \cdot A \qquad (4.7)$$

where 'A' is the area of the insonified patch of surface, (usually taken to the -3dB points) I_s is the intensity of the backscattered wave measured a distance 'r' from the surface, and I_0 is the intensity of the incident plane wave measured at the scattering patch. This may appear somewhat odd as the research has been directed at (bottom) *volume* backscatter. However, virtually all acoustic backscatter data contained in the literature is normalized using Equation (6.1), regardless of whether it is a surface or volume which is responsible for the scatter.

6.1 The Effect of Array Truncation on the Backscattering Strength

The definition of the surface backscattering coefficient given above, implies that a plane wave source has been used to insonify the scattering region. The model derived in Chapter 3 also assumes a plane wave source of insonification. In the experiments however, a truncated parametric array was employed which, unlike a conventional plane wave source, is characterized by a complicated spreading pattern. Note also that the size of the area insonified is affected by array truncation. Thus, before examining the backscatter data in terms of Equation (6.1), we must first correct for the effects of the truncated parametric array.

6.1.1 Spreading Loss and the Truncated Array

Figure (6.1) compares the axial range dependence of a pair of difference frequency signals; one transmitted from a parametric array truncated at 70cm and one transmitted from an untruncated parametric array. To avoid cluttering the figure, only the 25kHz and 100kHz data are plotted. It is obvious from the figure that there is a significant reduction in intensity past the point of truncation. This shall be referred to as the parametric array "truncation spreading loss"[1]. It is this which must be accounted for in the definition of BSS. Take as an example, the

---

[1] This is something of a misnomer as the drop in difference frequency intensity is only partially due to spreading. Truncation also reduces the array aperture which results in decreased intensity. However in the present context, "truncation spreading loss" will be used to encompass both effects.

25kHz data of Figure (6.1). At the exact point of truncation, the levels measured for the truncated and untruncated arrays are the same, within the limits of experimental error. At a range of 50cm past the truncation, the signal level from the truncated array is some 6dB lower than the signal from the untruncated array.

With the array truncated at 70cm, range calibration data taken at third octave frequencies in the band 25-200kHz, were used to obtain the truncation spreading loss, 70cm past the truncation. Figure (6.2) contains a plot of the truncation spreading loss data so obtained. The measured loss will be used to correct Equation (6.1), when estimating the BSS of the backscatter data taken at a range of 70cm from the scattering region.

The backscatter experiments performed at a range of 100cm from the scattering region must also be corrected for truncation spreading loss. In this case, the spreading loss at a range of 100cm past the truncation is required. Figure (6.3) contains a plot of the axial intensity of the difference frequency as a function of range, for an array truncated at 100cm. Also shown in the figure is the axial intensity range dependence of the differency frequency for the untruncated array. Once again, only the 25kHz and 100kHz data are plotted to avoid cluttering the figure. Due to space limitations in the calibration tank, measurements could only be made to a range of 40cm past the truncation point. (That is, a transducer-receiver separation of 140cm.) To obtain an estimate of the spreading loss 100cm past the truncation point we must first return to the data obtained with the 70cm truncation.

We begin by recasting the 70cm truncation data of Figure (6.1) in the following way. First, normalize the transducer-to-receiver range, R_{tr}, by the truncation distance, L. Next, normalize the signal intensity of both the 25kHz and 100kHz data so that the level at $R_{tr}/L=2$ (i.e. 140cm) is the same for both frequencies, say, 0dB. The result of this is shown in Figure (6.4). A simplified model of the parametric array[79], which assumes a line of sources, rather than a volume, predicts the fall off past truncation to follow a logarithmic decline of the form $\ln|R_{tr}/(R_{tr}-L)|$. The accuracy of this model improves at increased range from the truncation. The solid line in Figure (6.3) is a plot, in decibels, of the logarithmic fall off with the level adjusted to match the data obtained furthest from the truncation. Note that the range at which this approximation begins to be valid increases with frequency. The explanation for this may be found in Humphrey[78]: "...at high (difference) frequencies, the primary beam cross-section is not small compared with the difference frequency wavelength and the line array model breaks down."

Now returning to the data obtained with the 100cm truncation, and following the method outlined above, we recast the (truncation) data of Figure (6.3) in a manner similar to Figure (6.4). The result is shown in Figure (6.5). Included in the figure is the 200kHz data so that both lower and upper frequency limits are accounted for. The logarithmic model was matched to the experimental data at the point $R_{tr}/L=1.4$, to obtain an estimate of the spreading loss at $R_{tr}/L=2$. So long as the data has begun to follow the logarithmic decline at or before the range $R_{tr}/L=1.4$, the estimate will be good. Thus, in the present case the accuracy

is best at 25kHz and decreases with increasing frequency. However, even at 200kHz the estimate appears acceptable.

Range calibration data obtained with the array truncated at 100cm was matched to the logarithmic model in this way at third octave frequencies for the band 25 to 200kHz. The estimate of spreading loss thus obtained, is plotted in Figure (6.2). The loss estimate will be used to correct for the incident plane wave intensity contained in Equation (6.1), when plotting data from the backscatter experiments performed at the 100cm range.

6.1.2 Area Insonified and the Truncated Array

As well as accounting for spreading loss of the incident wave in the definition of BSS, we must also examine the area of insonification. A comparison of beam cross-sections for both the truncated and untruncated arrays, for a sample of difference frequencies, is contained in Figures (6.6) and (6.7). Figure (6.6) contains the beam cross-section data for a transmitter-receiver separation of 70cm. Figure (6.7) contains the beam cross-section data for a transmitter-receiver separation of 100cm. In both cases truncating the array had the anticipated effect of widening the beam cross-section. The widening however, was extremely slight. In determining the insonified area or "spot size", the truncated beam cross-section was always used.

Following the standard practice, the area within the -3dB region of insonification was used in the BSS definition. At normal incidence this was a circle, the diameter of which can be obtained from Figures (6.6) and (6.7). For the truncated array, the diameter ranged from approximately 10cm at 25kHz and 100cm range, down to 4.5cm at 200kHz and 70cm range.

Off normal incidence, but still at steep grazing, the area insonified becomes oblate and is given by:

$$A_{3dB} = A_n/\sin\varphi_g \qquad (6.2)$$

where A_n is the insonified area at normal incidence, and φ_g is the grazing angle. This expression continues to increase down to zero grazing where it reaches infinity. In reality however, the pulselength imposes an upper limit on Equation (6.2). That is, at shallow grazing the instantaneous return is confined to a scattering patch with length, X_{3dB}, given by:

$$X_{3dB}=c_w\tau/2\cdot\cos\varphi_g \qquad (6.3)$$

where τ is the pulse length and c_w is the acoustic wave speed in water. The width, Y_{3dB}, is obtained from Figures (6.6) and (6.7). Thus at shallow grazing, the area insonified approximates a rectangle so that

$$A_{3dB} = X_{3dB}\cdot Y_{3dB}. \qquad (6.4)$$

The angle at which the transformation from Equation (6.2) to (6.4) occurs, is determined by the broadness of the beam and the length of the pulse. For the present experiments it occured at approximately 45° grazing. The sketch contained in Figure (6.8) depicts the various spot sizes for the situations outlined above.

6.2 Normal Incidence Specular Reflection

It would be useful to check the validity of the correction to spreading loss in the backscatter definition. To this end, we shall

examine the volume backscatter data obtained at normal incidence. Actually, this would be more accurately termed the specular reflection at normal incidence. The advantage of testing the correction against this data is that specular reflection from a planar boundary is well understood so that any deviations from the expected result should be fairly obvious.

Take the simplest case of a plane wave reflecting from the interface at normal incidence. The intensity at the receiver, I_s, should be:

$$I_s = |\mathcal{R}|^2 \cdot I_0 \qquad (6.5)$$

where $\mathcal{R}$ is the Rayleigh pressure reflection coefficient and I_0 is the intensity incident at the surface. In the present experiments, $|\mathcal{R}|^2 \approx 0.14$ or -8.5dB. Looking back to Figure (5.8), the ratio I_s/I_0 for the normal incidence data was in the range of -20 to -25dB, i.e. about 12 to 17dB lower than the plane wave result. This is expected since the plane wave result assumes that both the incident and reflected waves are of infinite extent and thus doesn't account for any spreading loss. We can use the data for truncation spreading loss at 70cm given in Figure (6.2), to negate the effect of spreading in the normal incidence data of Figure (5.8). This in effect, "corrects" the experimental data to permit a meaningful comparison with the plane wave result of -8.5dB. The "corrected" experimental data and the plane wave result are shown in Figure (6.9). (Note that the ±3dB error bars on the experimental data are not rigorous but serve as a reasonable guideline for the present experiments.)

The agreement between the experimental data and plane wave result is quite good except at the lowest frequencies. The explanation for the deviation at low frequency can be found in the effect of the truncation. Recall from Figures (6.4) and (6.5) that the data begins to follow the logarithmic model closer to the truncation at low frequency than at high frequency. To put it another way, there is a sharper decrease in signal penetration immediately below the interface at low frequency than at high frequency. This means that there is less signal available to reflect back at low frequency, causing the experimental data to take on lower values than that of the plane wave estimate.

It appears then, that the correction to the BSS definition for truncation spreading loss is acceptable, although at low frequency we may expect the experimental data to be a few decibels lower than the estimate obtained using a plane wave model. Before proceeding, a final point should be made. The experiments to measure intensity past truncation were performed with the array truncated perpendicular to the beam direction. During the backscatter experiments, the sand interface truncated the array perpendicular to the beam only for the normal incidence measurements. Off normal incidence the truncation was oblique which would alter the spreading loss somewhat. Thus, the truncation spreading loss correction will be approximate for most of the backscatter data.

6.3 Surface Backscatter vs. Volume Backscatter

Intuitively, the author feels quite confident that at shallow grazing, the data collected in the volume backscatter experiments resulted from backscatter from the bottom volume and not the

bottom surface. The minuteness of the 130μm sand particles comprising the surface layer and the considerable effort made to smooth it provide reasonable justification for this. The question remains however, at what grazing angle does scatter from the surface begin to dominate the measurements? To answer this, data obtained from the surface backscatter experiment is plotted alongside volume backscatter data in Figure (6.10). The data shown are from the frequency band 100kHz to 200kHz. As is clear from the figure, at grazing angles less than about 55°, the backscatter is due almost entirely to scattering from the bottom volume.

Plotting the surface backscatter data as a function of frequency provides insight into the situation at frequencies less than 100kHz. As an example of this, the frequency dependence of the BSS is plotted for three grazing angles in Figure (6.11). First, at steep grazing such as 85°, the measured BSS increases with decreasing frequency. In this case, the measured signal actually results because the non-zero beamwidth of the incident signal leads to significant specular reflection at normal incidence. Since the beamwidth is inversely related to frequency, the level increases as frequency is decreased. At shallower grazing however, such as 65°, the BSS decreases significantly as frequency is decreased. Bearing in mind the particulate nature of the sand, this result is not surprising as Rayleigh scattering is the likely mechanism for surface backscatter. Finally, at an interim grazing angle such as 75° the backscatter is due to a mix of the two sources of backscatter so that no clear frequency dependence exists.

It appears then, that the BSS decreases with decreasing frequency at shallow grazing. Thus it seems reasonable that the contribution to backscatter resulting from surface roughness will be even less significant at lower frequency, at least for shallow grazing angles. This conclusion is reinforced further when one considers that the surface will appear even smoother relative to the acoustic wavelength at successively lower frequencies. Thus, comparison of the volume backscatter data with the theoretical model shall be confined to grazing angles less than 55°, but shall include the entire frequency band 25-200kHz.

6.4 Quantitative Examination of the Concentration Fluctuations

Values of physical constants such as density and acoustic wave speed for the experimental bottom are contained in Appendix F. It still remains however, to select an appropriate correlation function to describe the concentration fluctuations within the bottom, and to estimate the mean square value of these fluctuations. These terms are denoted N_c and $\overline{(\Delta S)^2}$, respectively. With values for N_c and $\overline{(\Delta S)^2}$, and the physical constants in Appendix F, we may obtain numerical estimates from the model in Chapter 3 to compare to the volume backscatter data. We begin with an estimate of $\overline{(\Delta S)^2}$.

6.4.1 Mean Square Value of Concentration Fluctuations

An experimental estimate of $\overline{(\Delta S)^2}$ can be obtained from the autocorrelation data of Figure (5.17) where the averaged data from the echosounder experiment is presented. The mean square value is, of course, given by the autocorrelation at zero lag. The four points in the figure at zero lag represent averaged mean

square estimates in the x and y directions for 10μsec and 40μsec pulses. All four estimates fall in the range:

$$\overline{(\Delta S)^2} = 0.010 \pm .002 \ . \qquad (6.6a)$$

To compare with the experimental value of $\overline{(\Delta S)^2}$, a theoretical estimate may be obtained in the following way. We begin by converting the tabulated values of mean particle size in Table (4.1), to values of concentration using the relationship derived in Appendix C. The results of the conversion are contained in Table (6.1).

The mean square value of the concentration fluctuations is defined as:

$$\overline{(\Delta S)^2} = \frac{1}{N} \sum_{i=1}^{N} (x_i - \mu)^2 \qquad (6.6b)$$

where μ is the mean value of the series, and x_i is the "ith" term and N the number of terms in the series[2]. From Table (6.1) we obtain a value of:

$$\overline{(\Delta S)^2} = 0.010 \qquad (6.6c)$$

---

[2] Of course, $\overline{(\Delta S)^2}$ is more commonly referred to as the variance but the expression "mean square value of the concentration fluctuations" is used to remain consistant with the terminology of Chapter 3.

which is in excellent agreement with the experimental value given by Equation (6.6a). We now turn our attention to obtaining an expression for N_c.

Table (6.1)

Layer #	Mean particle dimeter (μm)	Concentration
1	250	0.260
2	600	0.191
3	50	0.458
4	600	0.191
5	130	0.327
6	600	0.191
7	250	0.260
8	600	0.191
9	130	0.327
10	250	0.260
11	50	0.458
12	130	0.327
13	600	0.191
14	50	0.458
15	250	0.260
16	130	0.327

6.4.2 Exponentially Decaying Autocorrelation Function

Figure (5.18) contains a plot of the normalized autocorrelation data of the concentration fluctuations obtained from the echosounder experiment. Several features in the data are worth noting. The first of these is that the correlation length of the concentration fluctuations is significantly longer in the y

direction than in the x direction. This can be understood as follows. When constructing the scattering volume, the PVC tray holding the sand was pulled from the Sandlayer in the x direction by the gantry. While attempting to keep the speed of withdrawal constant, slight tremors and variations in speed were unavoidable. This caused varying amounts of sand to be deposited at different x positions. However, the amount being deposited would be approximately the same across the whole width of the tray. Since variations in layer thickness are akin to variations in concentration, this led to significantly shorter correlation lengths in x than in y.

Another feature of Figure (5.18) is the reduction in the autocorrelation function for the data obtained using the 40μsec pulse, relative to that obtained using the 10μsec pulse. The shorter pulse measured the autocorrelation of only the top layer. The longer pulse measured the correlation length, depth averaged over several layers. The result isn't surprising, if one considers the care taken in smoothing the top layer of sand to reduce fluctuations in layer thickness, thereby reducing fluctuations in concentration.

The autocorrelation data from Figure (5.18) are replotted in Figure (6.12). The solid lines in Figure (6.12) are exponentially decaying functions. For both lines, the 1/e point (chosen rather arbitrarily to be the correlation length) has been selected to provide a visual best fit to the data. From Figure (6.12) we obtain for the horizontal correlation lengths:

x_0=0.5cm; y_0=1.5cm (6.6d)

If we assume that the correlation in the z direction also takes the form of an exponential decay and that the z correlation length is the order of the layer thickness, we obtain an expression for N_c, the correlation function of the concentration fluctuations. This can be written as:

$$N_c = \exp-\left\{\frac{x}{0.5}+\frac{y}{1.5}+\frac{z}{0.7}\right\} \qquad (6.7)$$

where the correlation lengths are in centimetres. With the physical constants obtained from Appendix F, the correlation function given by Equation (6.7), and the mean square value given by Equation (6.6c) we are at last ready to compare the theoretical model to the volume backscatter data.

6.5 Comparison of Theoretical Model to Volume Backscatter Data

The correlation function for the concentration fluctuations given by Equation (6.7) is of the same form as Equation (3.41). In this case, performing the integrations in Equations (3.42) and (3.43) and summing the results, obtains a theoretical estimate of the volume backscatter intensity. As noted in Chapter 3, the author has been unsuccessful in his attempt to perform the integrations analytically. Instead a Monte Carlo integration has been used, the details of which are contained in Appendix E.

Figure (6.13) contains a comparison of the volume backscatter data obtained in the present study with the model results given by the sum of Equations (3.42) and (3.43). The data and model are plotted as a function of frequency for grazing angles of 45° and 20°. Both data and model have been plotted in

terms of the BSS defined in Equation (6.1). The error bars on the data represent the ±3dB limits. The agreement (within the limits of experimental error) of the 100kHz'a' and 100kHz'b' data points suggests that the measurements were not biased by the choice of transducer used in the parametric array.

The first thing to note is that no arbitrary adjustment has been necessary to match the level of the model to that of the data. The agreement of absolute levels between model and data is real. Furthermore, the general trend of the data, i.e. a fairly steep increase in backscatter level from 25 to 50kHz, above which the level becomes fairly constant, is predicted by the model. (As anticipated, at low frequency the plane wave model predicts slightly higher levels of backscatter than those measured. The reason for this has been outlined in section (6.3).) Given the error limits of the experimental data, it is overoptimistic to comment further on any agreement between the actual shape of the model curve and the data.

Figures (6.14) and (6.15) contain data from the volume backscatter experiment plotted in terms of the BSS as a function of grazing angle. Only data obtained at grazing angles of 55° or less are included to avoid contributions from surface backscatter. Once again no arbitrary adjustment has been necessary to match the level of the model to that of the data. Of particular note is the agreement between model and data at sub-critical grazing.[3] This is of particular interest, given the inability of previous

---

[3] The reader will recall that developing a volume backscatter model valid at shallow grazing is a major aim of the present study.

models to predict backscatter levels at shallow grazing. At 25, 50 and 100kHz the general trend of the data is predicted by the model. That is, a fairly steep increase in backscatter level from 10° to 25°, a sharp dip near 30° and finally a levelling off above about 35°. The 200kHz data however, continues to rise above 30° in disagreement with the model. One reason for this might be contamination of the data by Rayleigh scatter from the surface. Given that Rayleigh scattering is proportional to the fourth power of frequency, it is possible that the high frequency data was contaminated by surface scatter down to lower grazing angles than was the low frequency data. (This might also explain why the level of the 200kHz data point at 45° grazing in Figure (6.13) is so high.)

The model predicts a peak in the backscatter level at approximately 25°. Mathematically, this results from including the effect of attenuation when solving for the transmission of a plane wave into the bottom. This method of obtaining sub-critical penetration of a plane wave was first published by MacKenzie[80]. The experimental data clearly indicates the presence of this peak at sub-critical grazing, although in the 100kHz data it appears to be nearer 20°.

6.6 Alternative Correlation Functions for the Volume Inhomogeneities and Their Effect on the Model

Reasonable agreement between the volume backscatter data and the theoretical model has been achieved by using an exponentially decaying function to describe N_c, the correlation of the concentration fluctuations. The question remains however, can the agreement be improved by employing some other

expression in the model to describe N_c? To answer this, we examine two alternative expressions for N_c next.

6.6.1 The Gaussian Form for the Concentration Fluctuations

Maintaining agreement with the data of Figure (6.12) somewhat limits the choice of correlation function. One obvious possibility is a Gaussian function.

Figure (6.16) replots the autocorrelation data of Figure (6.12). The Gaussian functions, given by the solid lines in Figure (6.16), have been visually fit to provide a reasonable match to the data. From Figure (6.12) we obtain for the horizontal correlation lengths:

$$x_0=0.67\text{cm};\ y_0=1.0\text{cm}. \tag{6.8}$$

If we assume that the correlation in the z direction also takes the form of a Gaussian and that the z correlation length is the order of the layer thickness, we obtain an expression for N_c of:

$$N_c = \exp-\left\{\left(\frac{x}{0.67}\right)^2+\left(\frac{y}{1.0}\right)^2+\left(\frac{z}{0.7}\right)^2\right\} \tag{6.9}$$

where the correlation lengths are in centimetres.

The correlation function for the concentration fluctuations given by Equation (6.9) is of the same form as Equation (3.48). To obtain a theoretical estimate of the volume backscatter for this correlation function, we integrate Equations (3.49) and (3.50) and sum the result. (As before, a Monte Carlo integration was performed.)

Figure (6.17) compares a sample of the volume backscatter data obtained in the present study with the model results given by the sum of Equations (3.49) and (3.50). The data and model, given in terms of the BSS, are plotted as a function of frequency for a grazing angle of 20°. The lack of agreement between model and data above 50kHz is clearly evident. Agreement between the data and the model as a function of frequency is also poor. This can be seen in Figure (6.18) for the 100kHz case. The level of the data is some 10 to 20dB higher than predicted by the model. Furthermore, the model overestimates the rate of increase in BSS as a function of grazing angle.

6.6.2 The Uncorrelated Form for the Concentration Fluctuations

Many previous attempts to estimate BSS, have assumed that the bottom consists of a large number of independent scatterers; each scatterer being uncorrelated with its neighbouring ones[73]. This possibility is handled in the present model by assuming that N_c takes the value of unity within some small correlated volume, and is zero outside that volume. As this type of scattering model is fairly crude, the simplest case shall be examined; that of a spherically symmetric correlation volume.

Applying this model to the present experiment, it is reasonable to assume that the correlation length would be less than the layer thickness. Otherwise, the layers would effect the correlation thereby altering it from unity. To obtain a lower limit on the correlation length we consider that the length scale of the concentration fluctuations will be at least several sand particle diameters. This puts a lower limit on the correlation length of, say 2mm. This leads to the inequality:

$$0.2\text{cm} \leq r_0 \leq 0.7\text{cm} \tag{6.10}$$

where r_0 is the correlation length given by $r_0=(x_0^2+y_0^2+z_0^2)^{1/2}$. Choosing a correlation length approximately midway between the limits will provide a numerical example against which to compare the experimental volume backscatter data. Letting $r_0=0.5$cm results in the following expression for the correlation function:

$$N_c = \begin{cases} 1; & \rho \leq 0.25\text{cm} \\ 0; & \rho > 0.25\text{cm} \end{cases} \tag{6.11}$$

where due to the spherical symmetry, the correlation *radius* a_0, rather than the correlation *length* r_0, has been employed and $r_0=2 \cdot a_0$.

The correlation function for the concentration fluctuations given by Equation (6.11) is of the same form as Equation (3.51). To obtain a theoretical estimate of the volume backscatter for this form of correlation, we integrate Equations (3.53) and (3.54) and sum the result. (As before, a Monte Carlo integration was performed.)

The model result given by the sum of Equations (3.53) and (3.54), for $a_0=0.25$cm is compared to a sample of the present data in Figures (6.17) and (6.18). We turn first to Figure (6.17) and examine the frequency dependence at 20° grazing. The model underestimates the level of BSS; especially below 100kHz. Above 150kHz, the decrease in level predicted by the model is not evident in the data. The grazing angle dependence for 100kHz is

shown in Figure (6.18). The sharp drop in level at sub-critical grazing puts the model estimate some 10dB below the data at 15°. The agreement between data and model above 30° is most likely coincidence.

The lack of agreement between the model and data for this last choice of correlation function is not surprising. The data in Figure (6.12) clearly indicates a more complicated form for the correlation of the concentration fluctuations than that proposed in Equation (6.11).

6.7 The Refracted and Lateral Components of Backscattered Intensity

One of the significant features of the theoretical model derived in Chapter 3 was the inclusion of the lateral wave contribution to the backscattered intensity, in addition to the backscattered refracted wave. It would be useful to examine the contribution to the backscattered intensity of each of these terms separately. The best fit to the volume backscatter data was obtained when N_c was approximated in the model by an exponentially decaying function -Equation (6.7). Hence, this solution shall be used when examining the separate lateral and refracted terms in the model. The refracted term will be obtained from Equation (3.42); the lateral term from Equation (3.43). As before, a Monte Carlo integration was employed with the physical constants obtained from Appendix F.

Figure (6.19) contains a plot of the two volume backscatter terms as a function of frequency at 20° grazing. Below 75kHz the contribution from each term is about the same. However, at frequencies greater than 75kHz, the lateral term continues to

rise in level, while the refracted term begins to decrease. At 200kHz the lateral term is nearly 10dB higher than the refracted term.

Figure (6.20) contains a plot of the two volume backscatter terms as a function of grazing angle at 100kHz. Note that the lateral wave only exists at sub-critical grazing. (The reason for this is discussed in Appendix B where the nature of the lateral wave is examined more closely.) From the figure it is clear that the lateral wave contributes significantly to volume backscatter at sub-critical grazing. In fact, at very shallow grazing, below 20°, it dominates the volume backscatter.

This concludes the comparison of the model to the present data. In the following chapter, the model shall be tested against data contained in the literature to see if better agreement is achieved with it than with previous models.

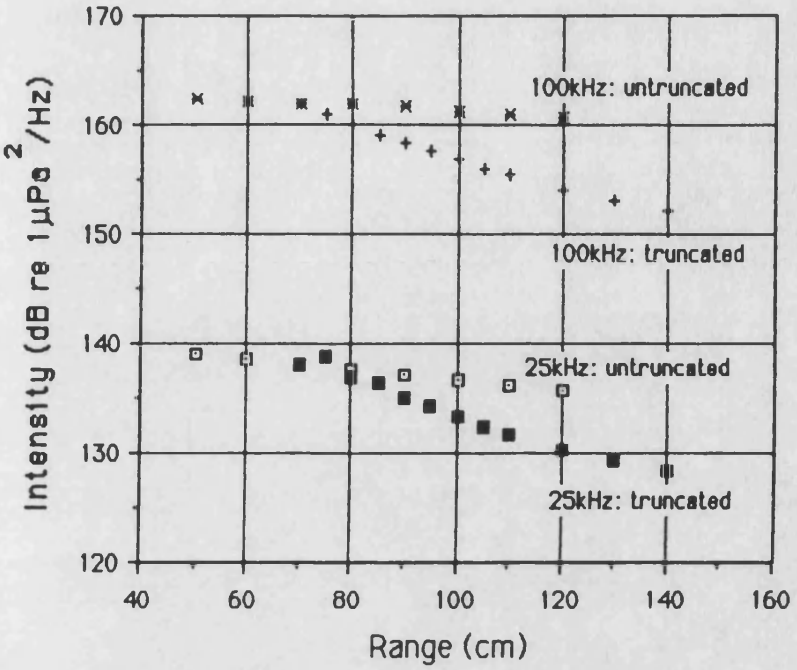

Figure (6.1): Range dependence for difference frequency signal for an untruncated parametric array and one truncated at 70cm.

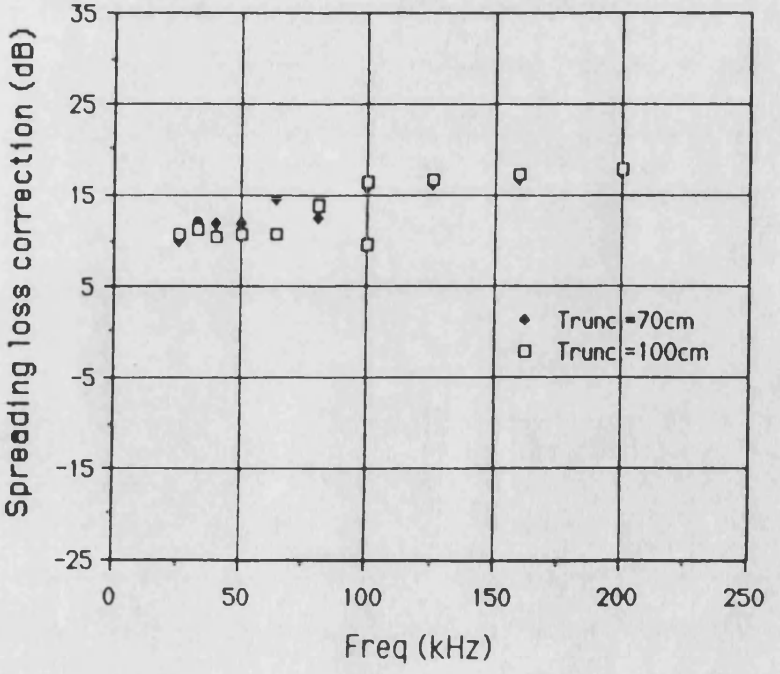

Figure (6.2): Spreading loss correction to parametric array data to enable comparison with plane wave model.

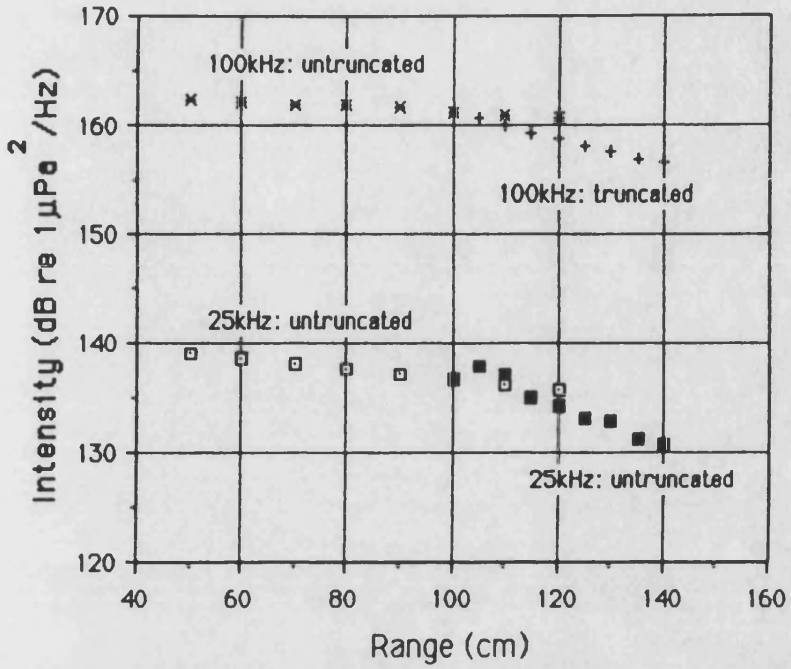

Figure (6.3): Range dependence for difference frequency signal for an untruncated parametric array and one truncated at 100cm.

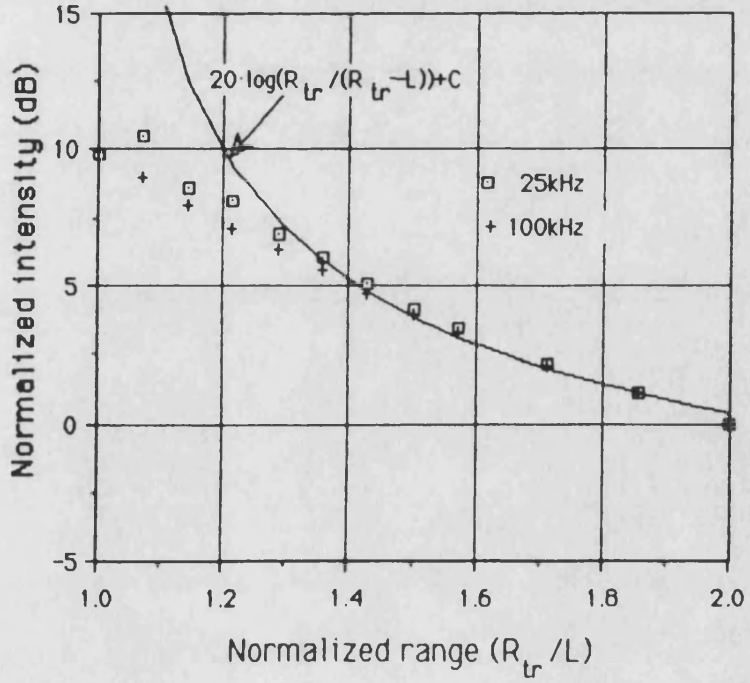

Figure (6.4): Intensity as a function of normalized range past truncation. Array truncation occurs at 70cm.

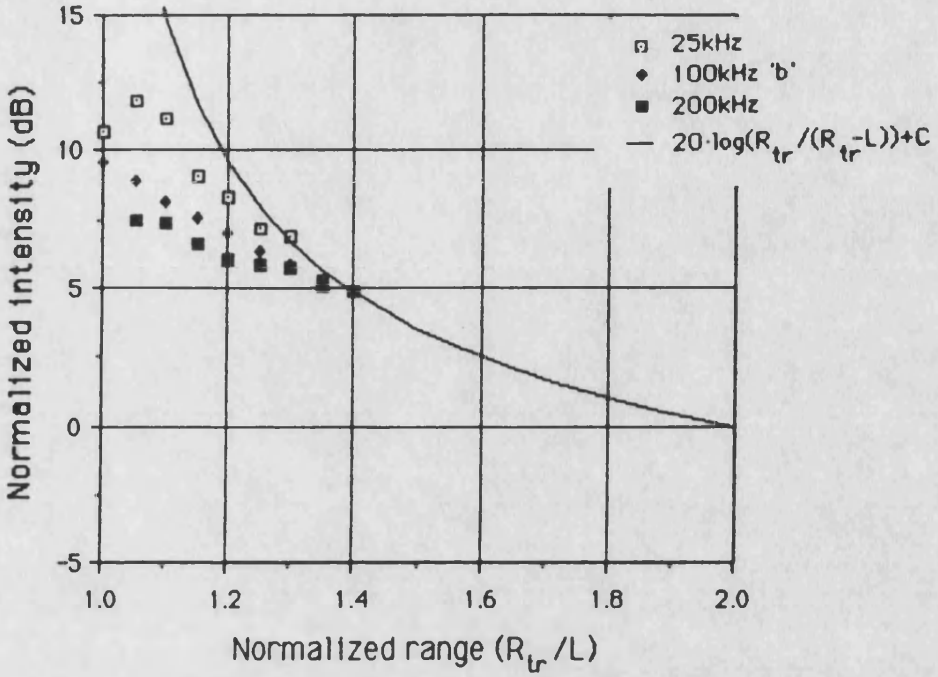

Figure (6.5): Intensity as a function of normalized range past truncation. Array truncation occurs at 100cm.

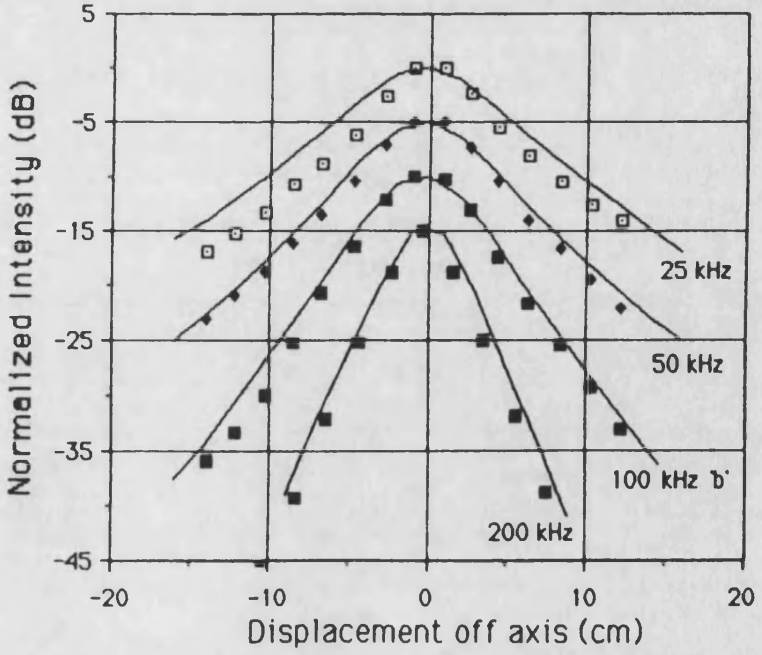

Figure (6.6): Difference frequency beam cross-section for a transducer-receiver separation of 70cm. Points represent the untruncated array, solid lines the truncated array.

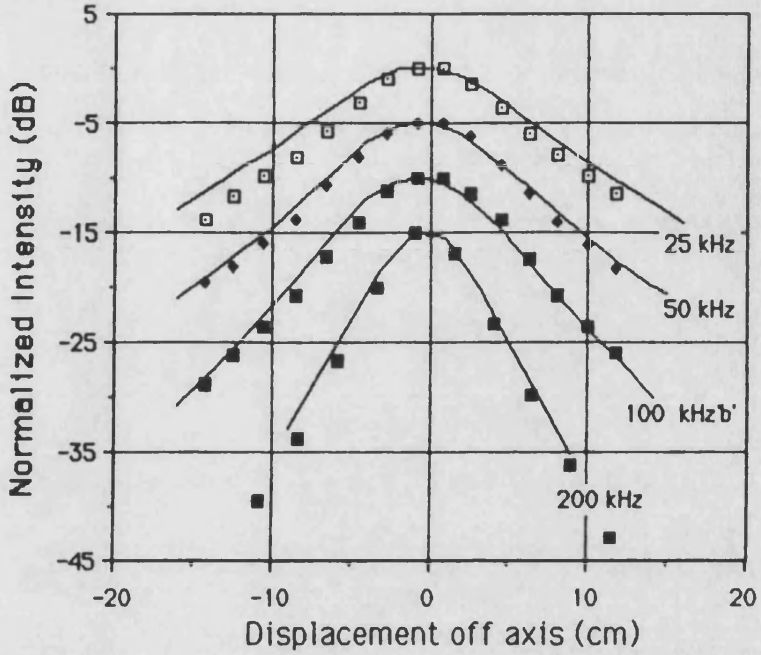

Figure (6.7): Difference frequency beam cross-section for a transducer-receiver separation of 100cm. Points represent the untruncated array, solid lines the truncated array.

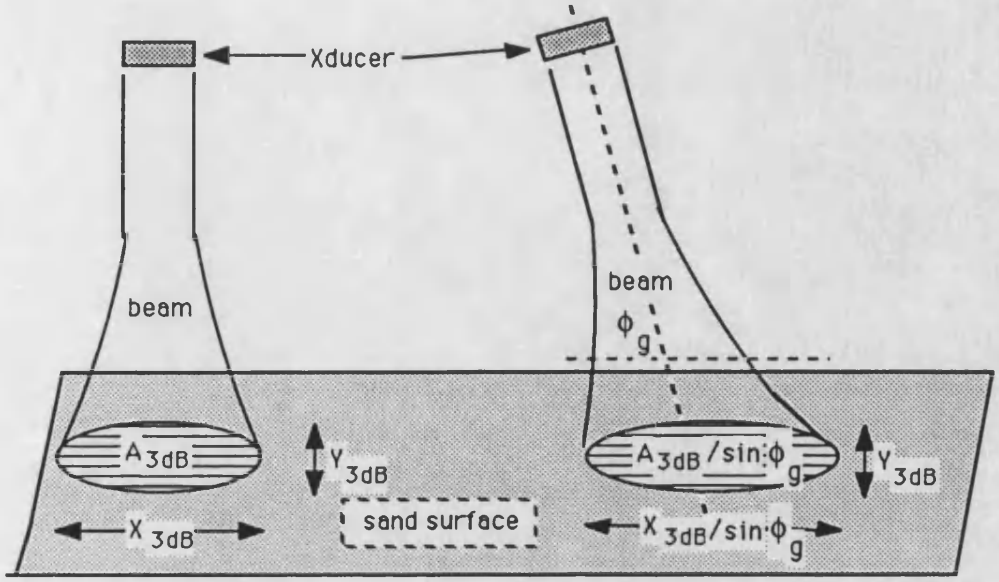

(a) Normal incidence (b) Steep grazing

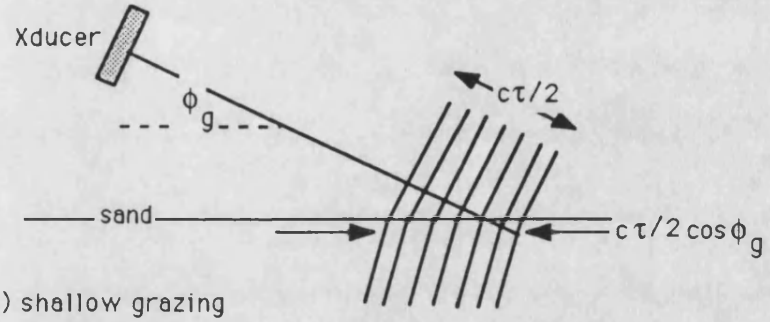

(c) shallow grazing
(cross-section)

Figure (6.8): Area insonified for various grazing angles.

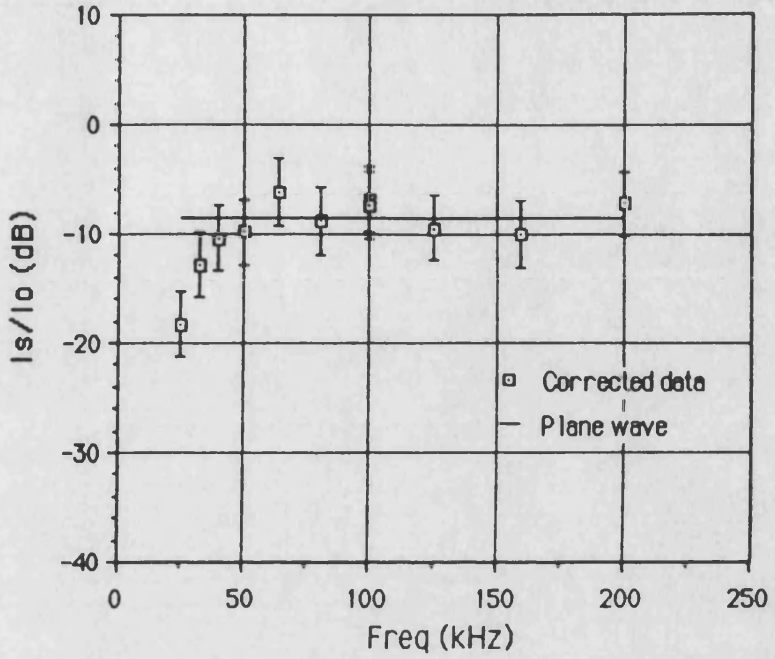

Figure (6.9): Comparison of normal incidence plane wave reflection loss with parametric array data taken at normal incidence and corrected for truncation spreading loss.

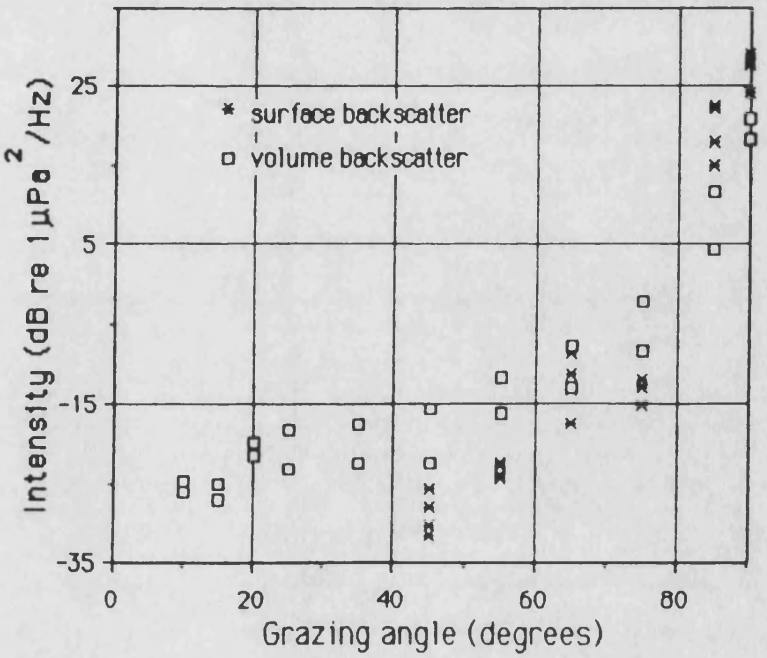

Figure (6.10): Comparison of data obtained from volume backscatter experiment and surface backscatter experiment. The data is from the frequency band 100-200kHz.

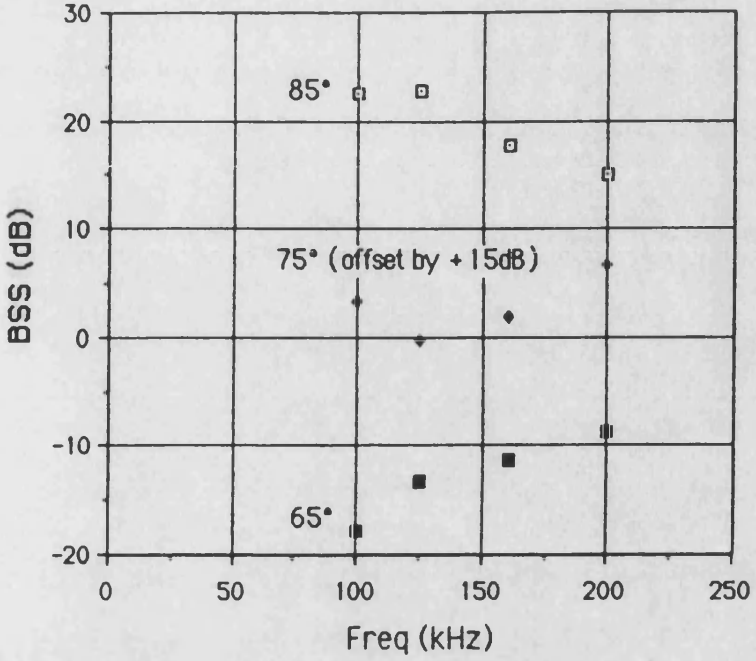

Figure (6.11): Backscattering strength of data obtained from surface backscatter experiment.

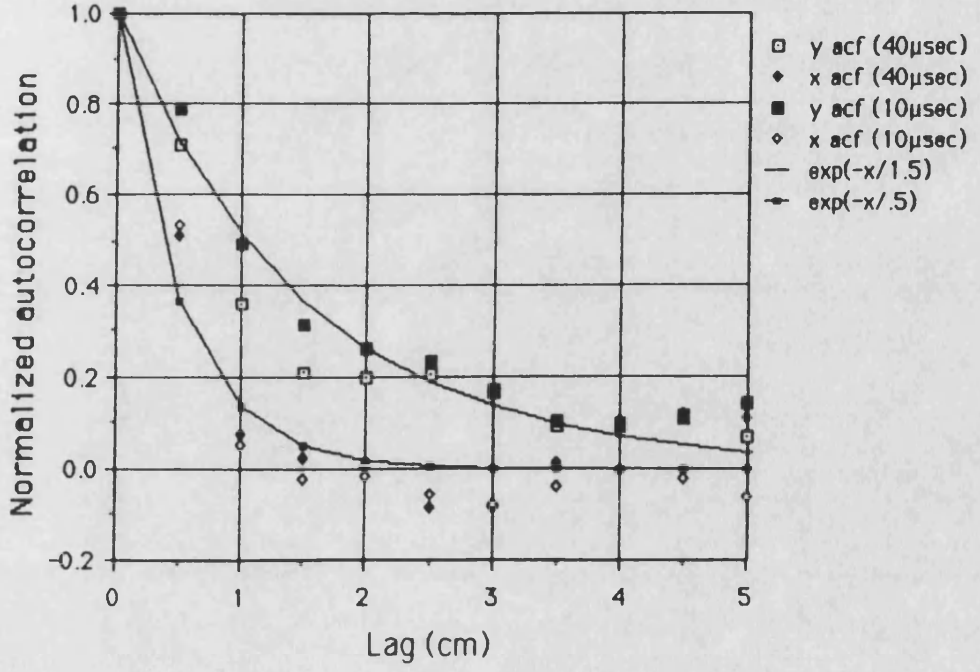

Figure (6.12): Autocorrelation (acf) data from echosounder experiment. Solid lines are exponential decay functions visually fit to the data.

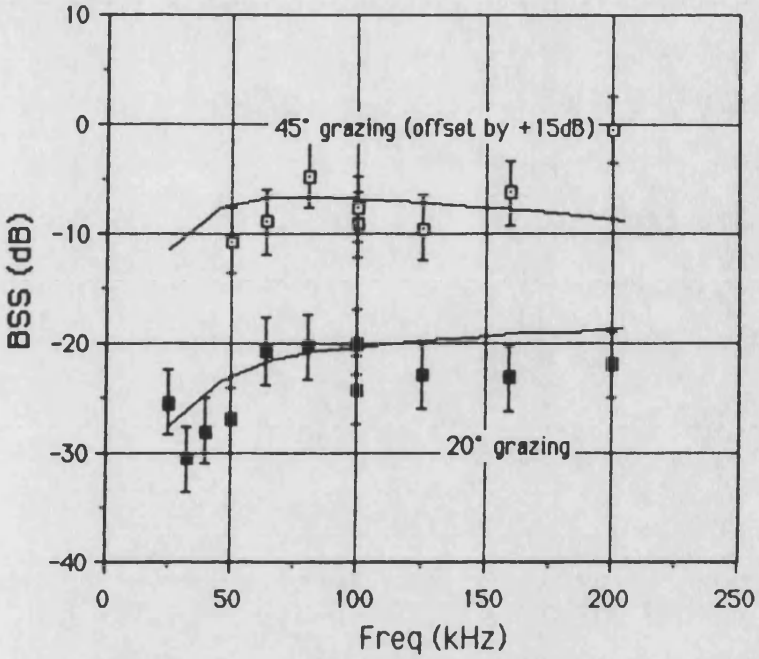

Figure (6.13): Comparison of volume backscatter data (points) to model with exponentially decaying autocorrelation of concentration fluctuations (lines).

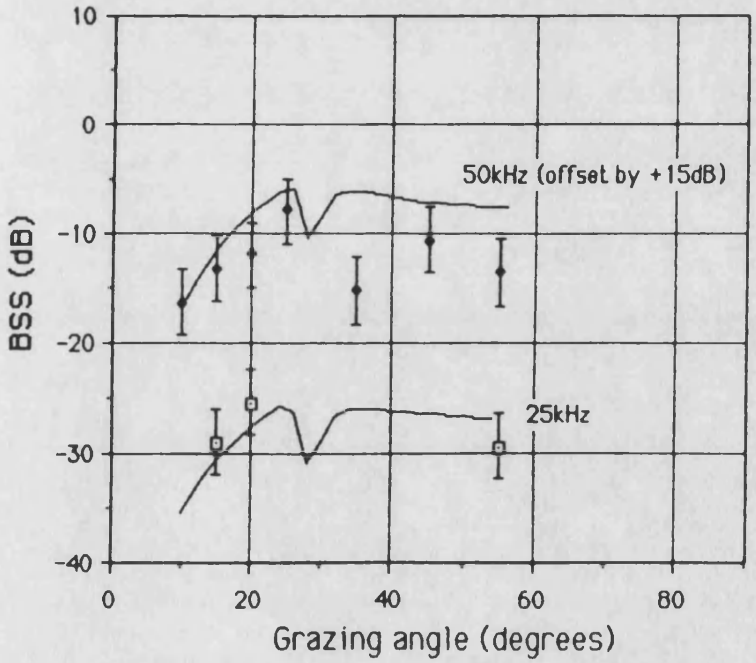

Figure (6.14): Comparison of volume backscatter data (points) to model with exponentially decaying autocorrelation of concentration fluctuations (lines).

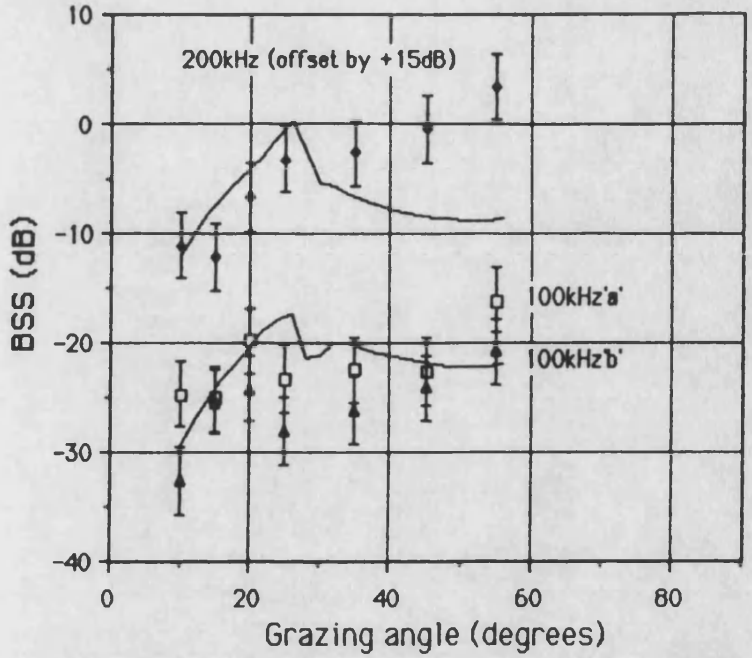

Figure (6.15): Comparison of volume backscatter data (points) to model with exponentially decaying autocorrelation of concentration fluctuations (lines).

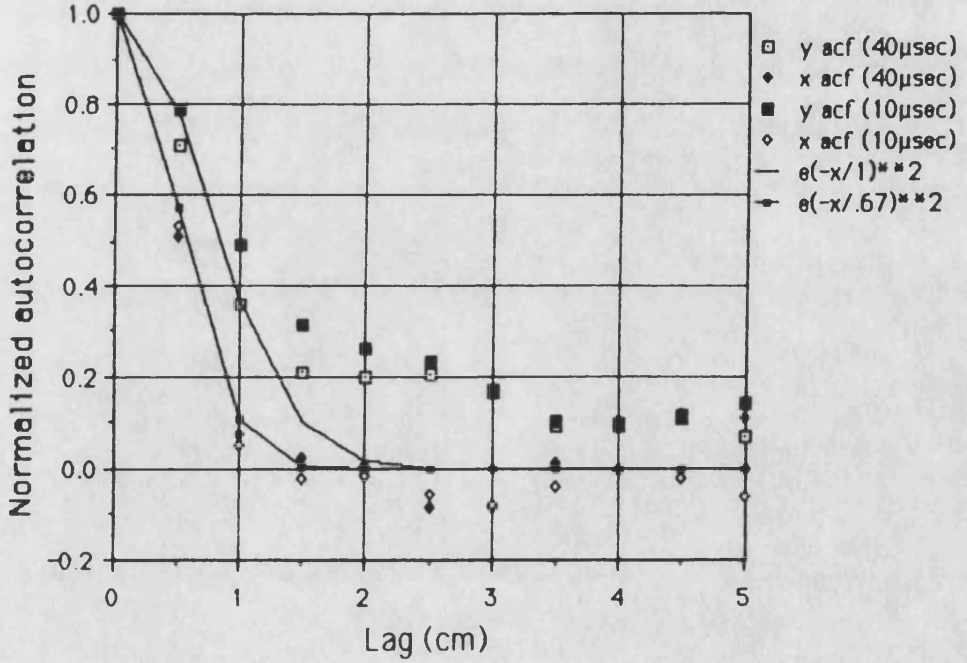

Figure (6.16): Autocorrelation data from echosounder experiment. Solid lines represent Gaussian functions visually fit to the data.

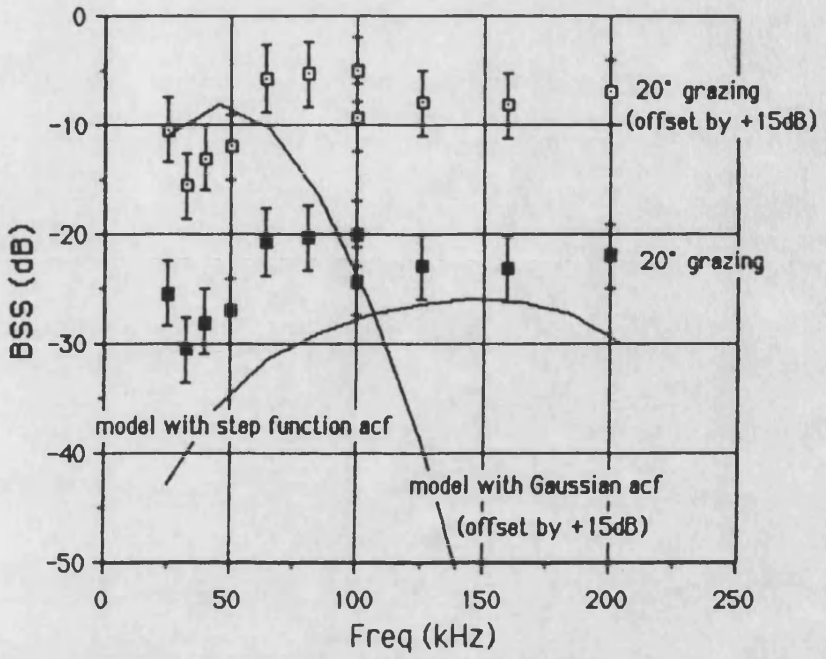

Figure (6.17): Comparison of volume backscatter data (points) to models with Gaussian and step function autocorrelations of concentration fluctuations (lines). See text.

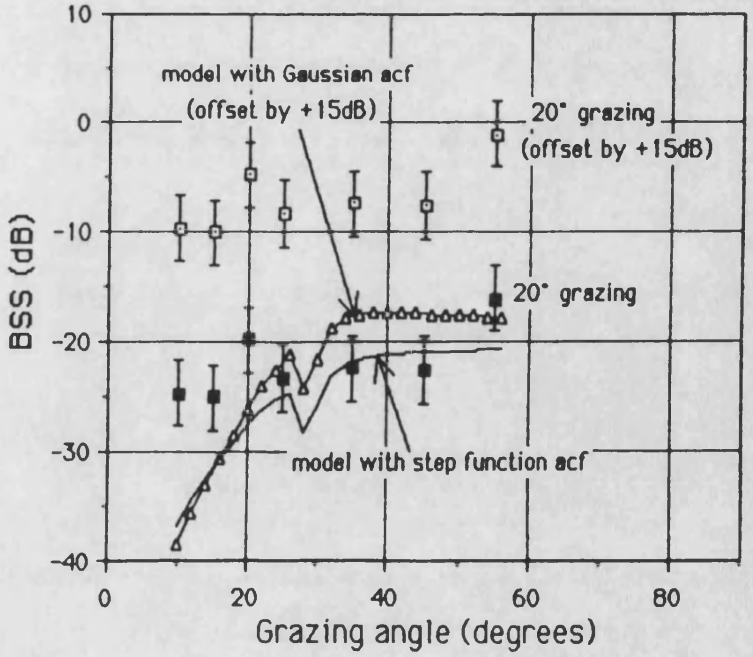

Figure (6.18): Comparison of volume backscatter data (points) to models with Gaussian and step function autocorrelations of concentration fluctuations (lines). See text.

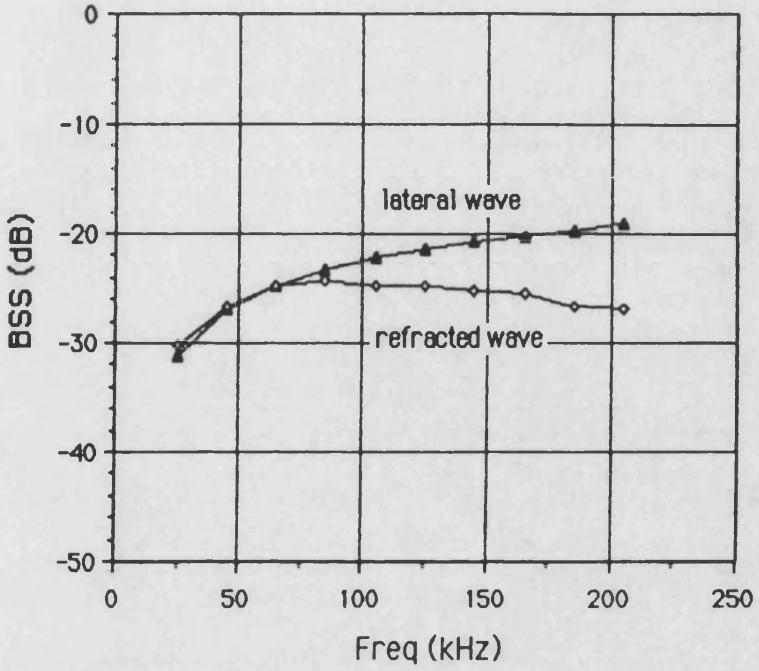

Figure (6.19): Separate contributions of refracted and lateral wave components at 20° grazing.

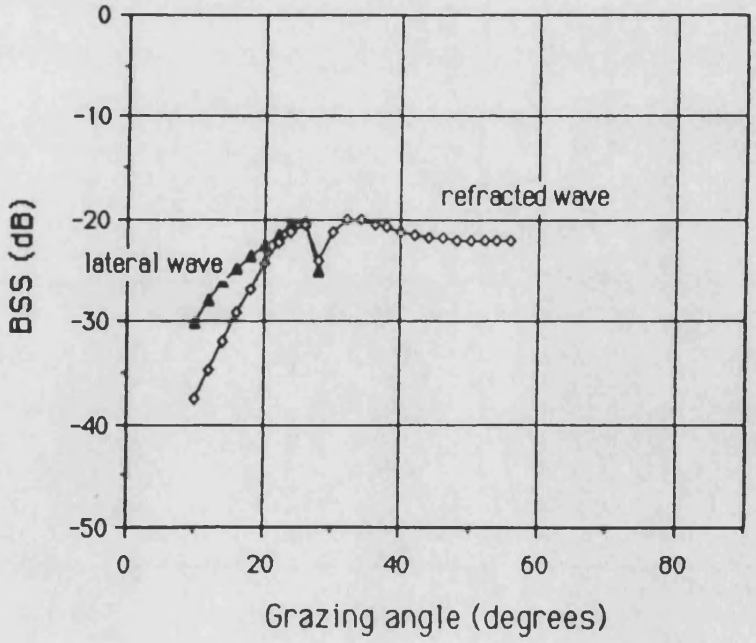

Figure (6.20): Separate contributions of refracted and lateral wave components at 100kHz.

CHAPTER 7

COMPARISON OF THE MODEL WITH PUBLISHED DATA

The agreement between the volume backscatter model and the laboratory data presented in the previous chapter is quite encouraging. It appears that the model derived in Chapter 3 provides a reasonable description of volume backscatter phenomena. However, parameter variations in the backscatter experiments were somewhat confined. For example only one bottom type was used, the frequency band was limited to 25-200kHz, and grazing angles were restricted to greater than 10°. To be useful, the model must be robust enough to provide backscatter estimates over a wide range of parameters. The aim of this chapter is to test the robustness of the model. To do this it shall be compared to experimental data published in the literature. The data is taken from both laboratory and ocean experiments for which many of the parameters were different than those of the present study.

Before commencing we note the following point. In most of the literature examined below, information about pulse length, area insonified, and source range from the scattering region was not supplied. When evaluating the model, values for these parameters have been chosen to meet the following criteria: (a) That the dimensions of the area insonified are much greater than the correlation length of the bottom inhomogeneities. (b) That the acoustic source is in the far field relative to the area insonified.

7.1 Volume Backscatter Model Compared to Nolle et alia

Nolle et alia[8] provide an excellent starting point for our comparison. They too made laboratory measurements of acoustic

backscatter from a smoothed sand volume. However, their experiments were performed at 500kHz and 1000kHz, and in each experiment the sand was composed of a single grade.

Figure (7.1) contains a plot of their backscatter data from a volume comprised of sand particles corresponding to sieve mesh numbers BS120-140. This is equivalent to a mean particle diameter of approximately 115μm. The physical constants for 115μm sand have values very similar to those of the 150μm sand used in the present study. Since the values of the constants have been investigated for the 150μm sand [81], they shall be employed in the backscatter model. They are contained in Appendix F.

The two sets of points shown in Figure (7.1) correspond to two separate trials by Nolle et alia using the same experimental setup. Each point shown is the backscatter averaged from 20 patches of sand. The data is for a frequency of 500kHz. To compare the present model to this data we must first estimate N_c, the correlation function of the concentration fluctuations for the sand volume. We must also estimate $\overline{(\Delta S)^2}$, the mean square value of the concentration fluctuations, to determine the magnitude of the volume backscatter.

Recall that an exponentially decaying function provided a good fit to the autocorrelation data of N_c for the sand volume used in the present experiments. This was true of the measurements made on a single sand layer as well as several layers averaged, in both x and y directions. Based on this, we shall assume an exponentially decaying function for N_c for Nolle et alia's sand volume. Note however, that in their experiment,

concentration fluctuations result primarily from fluctuations in particle size about the mean diameter.[1] These fluctuations will likely occur over a length scale the order of several particle diameters. For 115μm sand this should result in a correlation length on the order of 1mm in any direction.

The concentration at any depth will be affected slightly by the weight of sand above. This is particularly true near the surface, where the packing density may decrease marginally as one approaches the interface. For this reason, we shall assume radial symmetry in the horizontal plane rather than in three dimensions. (In fact this does not significantly alter the result.) This leads to the following estimate for N_c:

$$N_c = \exp-\left\{\frac{r}{0.1}+\frac{z}{0.1}\right\} \qquad (7.1)$$

where $r=(x^2+y^2)^{1/2}$ and the correlation lengths are given in centimetres. An estimate is also required for $\overline{(\Delta S)^2}$. This is obtained next.

Nolle et alia include in their paper a graph of the percentage weight distribution of the 115μm sand as a function of particle diameter. This is reproduced in Figure (7.2). (Note that the ordinate axis has been normalized so that the maximum value is unity.) Using the relationship between particle size and concentration obtained in Appendix C, the data of Figure (7.2) has been replotted with the abscissa converted to concentration. This is shown in Figure (7.3). Also drawn in Figure (7.3) is a

---

[1] The reader will recall that these fluctuations were considered a second order effect in our own experiments and ignored.

normalized Gaussian distribution which fits the data reasonably well. The Gaussian function g(S), is given by:

$$g(S) = \exp-\left\{\frac{(S-\mu)^2}{2\cdot\overline{(\Delta S)^2}}\right\} \qquad (7.2)$$

where 'S' is the concentration, 'μ' is the mean value of the concentration, and $\overline{(\Delta S)^2}$, as has been previously noted, is the mean square value of the concentration fluctuations or variance. From the figure we obtain:

$$\mu = 0.35;\ \overline{(\Delta S)^2} = 0.0010\ . \qquad (7.3)$$

Using the autocorrelation function given by Equation (7.1), the mean square value given by Equation (7.3) and the physical constants contained in Appendix F for 150μm sand, we can obtain a numerical estimate of volume backscatter for the experimental setup of Nolle et alia.

The correlation function given by Equation (7.1) is of the same form as Equation (3.35). In this case, performing Monte Carlo integrations on Equations (3.39) and (3.40) and summing the results, obtains a theoretical estimate of the volume backscatter intensity.

Figure (7.4) contains a comparison of the model result given by the sum of Equations (3.39) and (3.40) with the volume backscatter data obtained by Nolle et alia. As usual, the figures are in terms of the backscattering strength (BSS). It is clear from the figure that the agreement is excellent. Also plotted in the figure is the Nolle et alia model. Their model decreases in level

too quickly at shallow grazing. Furthermore, it does not predict absolute levels; they simply adjusted the curve vertically to provide a visual best fit to the data.

In obtaining a numerical estimate with their model, Nolle et alia assumed that the correlation distance is the order of the particle size. This represents only a fraction of a wavelength at 500kHz. Hence it is roughly equivalent to assuming that the volume is comprised of a large number of uncorrelated scattering centres. It would be reasonable then, to compare the Nolle et alia model with the present model solved for the case of uncorrelated scattering centres. We choose a correlation length of a_0=100μm, the approximate particle size, to remain consistant with Nolle et alia. The model estimate is obtained by integrating Equations (3.53) and (3.54) and summing the result. Figure (7.5) contains a plot of the data and model of Nolle et alia compared to an estimate obtained from Equations (3.53) and (3.54). The shape of the curve obtained with this form of the present model still matches the data reasonably well although it appears to drop below the data near 20°. More significant is the fact that this time the level of the model had to be *raised* 14dB to fit. Thus the exponentially decaying correlation of Equation (7.1) combined with Equations (3.39) and (3.40) still provides the best fit to the data of Nolle et alia.

7.2 Volume Backscatter Model Compared to Jackson et alia

Jackson et alia[72] performed backscatter measurements at several ocean sites. Bottom type information is included in the paper, making it particularly useful for the present comparison. We shall examine their data from the location they termed "Puget

Sound site 1". The sediment there was fairly smooth minimizing the effects of bottom roughness on the measured backscatter. The site consisted of silty sand with mean grain size 35μm. Buried in the sediment were numerous shell fragments of which they state that less than 2.5% were of a length scale greater than 6.4mm. The physical constants they list for the area are contained in Appendix F. These shall be used when obtaining numerical results from the present model.

As usual, we require expressions for the correlation function N_c (particularly the correlation length) and the mean square value $\overline{(\Delta S)^2}$ if we are to obtain numerical results from the model. Unfortunately, this information is not provided in their paper. However, we can make estimates of these parameters in the following way. First we note that the size distribution of particles at Puget Sound site 1 range from 35μm to a few millimetres. The particle size distribution used during the present experiments ranged from 50μm to approximately 1mm. Thus the mean square value of the concentration fluctuations calculated for the present experiments should provide a reasonable approximation for Puget Sound site 1. Extending the analogy between Puget Sound site 1 and the present experiments, we choose an exponentially decaying correlation function for N_c. Recall that the x,y correlation lengths for the present experiments were both in the range 1.0±0.5cm, even though the mechanisms determining the correlation length in each direction were fairly different. Based on this, we shall assume the correlation length at Puget Sound site 1 to be the order of 1cm. Jackson et alia state that neither photographs nor television

scans of the bottom relief indicated any anisotropy. Thus we shall assume radial symmetry in the horizontal plane. This leads to a correlation function for the concentration fluctuations of:

$$N_c = \exp-\left\{\frac{r}{1.0}+\frac{z}{1.0}\right\} \tag{7.4}$$

where the correlation lengths are given in centimetres. Combining Equation (7.4) with a mean square value of $\overline{(\Delta S)^2}=0.010$ (calculated in section 6.4) and Jackson et alia's physical constants from Appendix F, permits evaluation of the model.

Performing Monte Carlo integrations on Equations (3.39) and (3.40) and summing the results, obtains a theoretical estimate of the volume backscatter intensity for the Puget Sound site. The solid line in Figure (7.6) is a plot of the BSS of the model evaluated at 50kHz. The two sets of points represent the upper and lower limits of data taken at frequencies from 40 to 50kHz by Jackson et alia at Puget Sound site 1. The match in absolute level between model and data is quite good, although one admits that in light of the cavalier estimates of $\overline{(\Delta S)^2}$, r_0, and z_0, further evidence of this is required.

More significant at this stage is the similarity of the shape of the model curve and the data, since the shape of the curve as a function of grazing angle isn't heavily dependent on correlation length. This can best be shown with the aid of a figure. In Figure (7.7), the model is evaluated for the correlation function given by Equation (7.4) for two quite different choices of correlation length. Curve 1 has r_0=1cm, z_0=1cm; Curve 2 has r_0=10cm, z_0=1cm. In both cases, the model was evaluated for a frequency of

50kHz with $\overline{(\Delta S)^2}$=0.010. Examining only the grazing angle data, we might conclude that the longer horizontal correlation length is correct and the estimate of $\overline{(\Delta S)^2}$ based on the present experiments is 10dB too low for the Jackson et alia data. In either case the model matches the curve quite well at low grazing. One should note that at grazing angles greater than 40° there may be contributions from bottom roughness scatter, so the lack of agreement between model and data may not be the fault of the model.

To determine which combination of correlation length and mean square value of concentration fluctuations is correct, we must compare the frequency information of the model with that contained in the data of Jackson et alia. No curves of the dependence of the BSS on frequency are actually given in their paper. Instead, they present a tabulated list of the frequency dependence of the BSS at 20° grazing, for the various sites at which they gathered data. For the Puget Sound site 1, they list the BSS dependence on frequency as +1.4dB/octave in the band 20-85kHz. The standard deviation of this slope is given as 0.8dB. The straight line shown in Figure (7.8) represents the frequency dependence of their BSS data at Puget Sound site 1. The vertical bars represent the uncertainty in their estimate of the slope based on their standard deviation calculation. The absolute level of the straight line was obtained from their curve of the BSS dependence on grazing angle at 50kHz and 20° grazing. Also contained in Figure (7.8) is the frequency dependence of the model at 20° grazing for the two pairs of correlation lengths discussed above. For Curve 1: r_0=1cm, z_0=1cm; and for Curve 2: r_0=10cm,

z_0=1cm. In both cases $\overline{(\Delta S)^2}$=0.010. The curve obtained with the former set of correlation lengths agrees with the data in both absolute level and slope. Contrast this, with the curve obtained using the latter set of correlation lengths. Increasing the value of $\overline{(\Delta S)^2}$ by about 10dB would result in matching the absolute levels of the curve and the data, but not their slopes. Thus it does appear that the original choices for the correlation lengths and the mean square value of concentration fluctuations were justified.

7.3 Volume Backscatter Model Compared to McKinney and Anderson

A comparison of the model with published data would not be complete without including the results of McKinney and Anderson[69]. While being one of the earliest papers on the subject, it still forms one of the most complete sets of bottom backscattering data available. Figure (7.9) reproduces their curve for the BSS at 100kHz averaged over several sand bottoms. The mean particle size for the various bottoms ranged from approximately 10μm to 400μm. For comparison, their data points for a sample bottom with mean particle size 100μm are also given. These too are for a frequency of 100kHz.

The only indication given in their paper as to the magnitude of the fluctuations about the mean size at any one location is their statement that "for the coarser sands...the size was usually very homogeneous and concentrated near the mean value. For the finer sands...there were significant amounts (35%-75%) with diameters in the range of 0.1mm." There is no information on the function N_c. Hence, we are again forced to estimate expressions for N_c, and $\overline{(\Delta S)^2}$ in order to evaluate the model. Since we are

dealing with sand bottoms with particle sizes in the range of those used in the present experimental work, we shall use Equation (7.4) for N_c and set $\overline{(\Delta S)^2}=0.010$. For the physical constants, we shall use the averaged values of the various sands employed in the present experiments. The resulting curve, once again obtained by integrating Equations (3.39) and (3.40) and summing the results, is shown alongside McKinney and Anderson's data in Figure (7.9). The agreement of data and model in both level and shape is quite acceptable, especially from 10°-30° grazing.

7.4 Volume Backscatter Model Compared to Patterson

The final data we shall examine is taken from Patterson[68]. No information on the bottom type is provided in the paper; only the refractive index and the ratio of bottom-to-water density are given. (These values are contained in Appendix F.) For this reason the model and data shall be compared in only a general sense. The two sets of points in Figure (7.10) represent the upper and lower limits of Patterson's bottom backscatter data, obtained from transmitted pulses of 10msec to 300msec at a frequency of 2.5kHz. The solid line in the figure was obtained by evaluating the model using Patterson's values for the wave speed and density[2] and a correlation function for N_c given by:

---

[2] Evaluation of the model actually requires the attenuation coefficient for the bottom which was not supplied. However, at 2.5kHz, attenuation would be negligible for the volumes insonified in the experiment. Therefore, when evaluating the model, attenuation in the bottom was ignored.

$$N_c = \exp-\left\{\frac{r}{10.0}+\frac{z}{10.0}\right\} \qquad (7.5)$$

where the correlation lengths are given in centimetres.

The choice of Equation (7.5) was based purely on heuristic arguments. Whatever the cause of decorrelation within the bottom, it seems unlikely that the dominant correlation length at such a low frequency would be as small as that which we have been previously employing. For this reason the correlation length has been increased by an order of magnitude since the acoustic wavelength in Patterson's experiment is about an order of magnitude greater than that of the other experiments examined. As was already mentioned, there was no way to estimate $\overline{(\Delta S)^2}$ so the absolute level of the model has been adjusted to match the data. The agreement in the shape of the curve with the data is quite good. Of particular note is the minimum which both data and curve exhibit at 25°.

This concludes the comparison of the model with the literature data. The model has been used quite successfully to estimate bottom volume backscattering for a relatively wide set of parameters. However, to obtain the most value from the model predictions, a knowledge of the mean square value and correlation function of the concentration fluctuations is required.

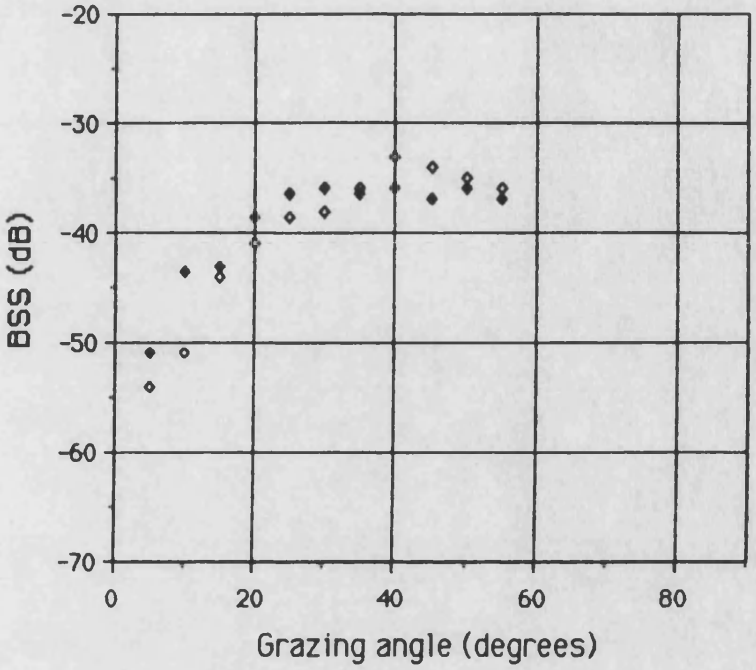

Figure (7.1): Acoustic backscatter from a smoothed sand volume. Data from Nolle et alia[8] at a frequency of 500kHz.

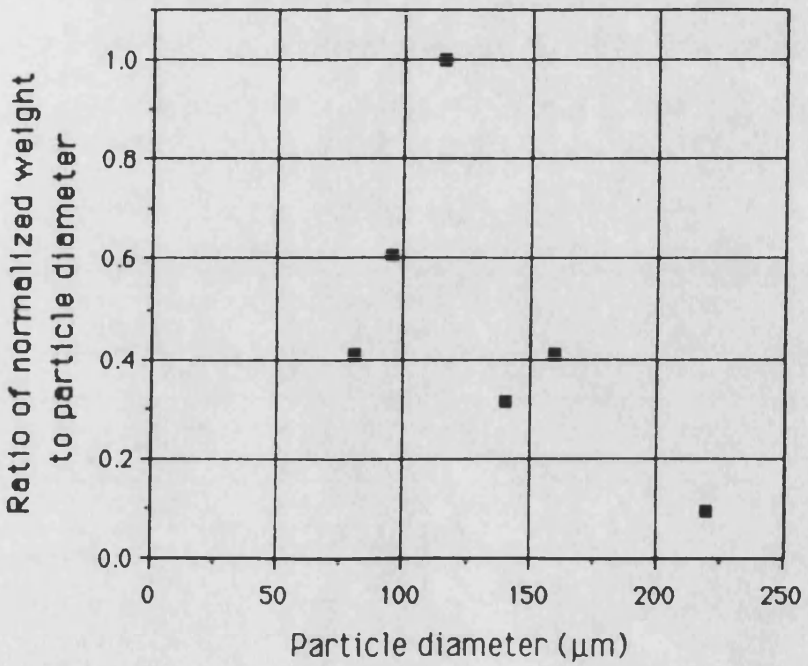

Figure (7.2): Normalized weight distribution as a function of particle diameter for one of the sand volumes used by Nolle et alia[8].

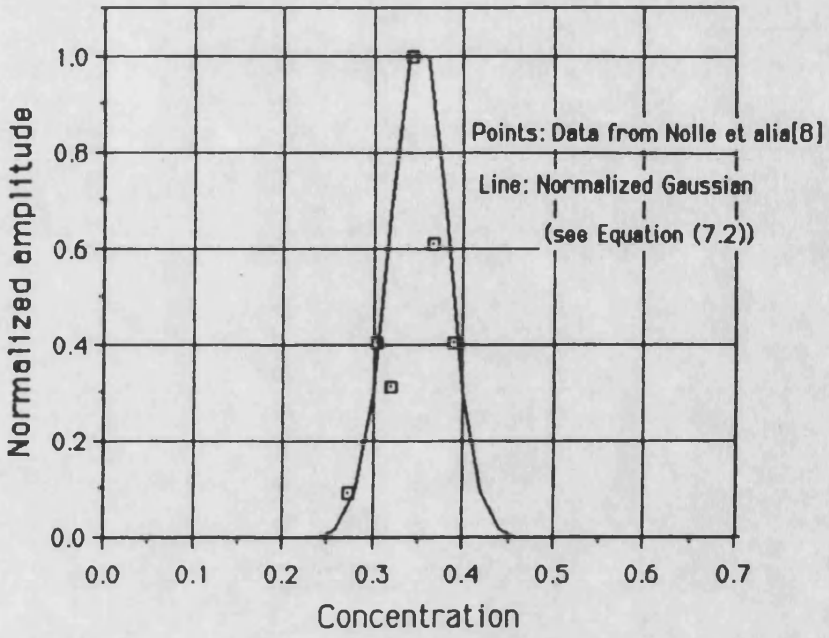

Figure (7.3): Normalized weight distribution as a function of concentration for one of the sand volumes used by Nolle et alia. The Gaussian has been visually fit to the data.

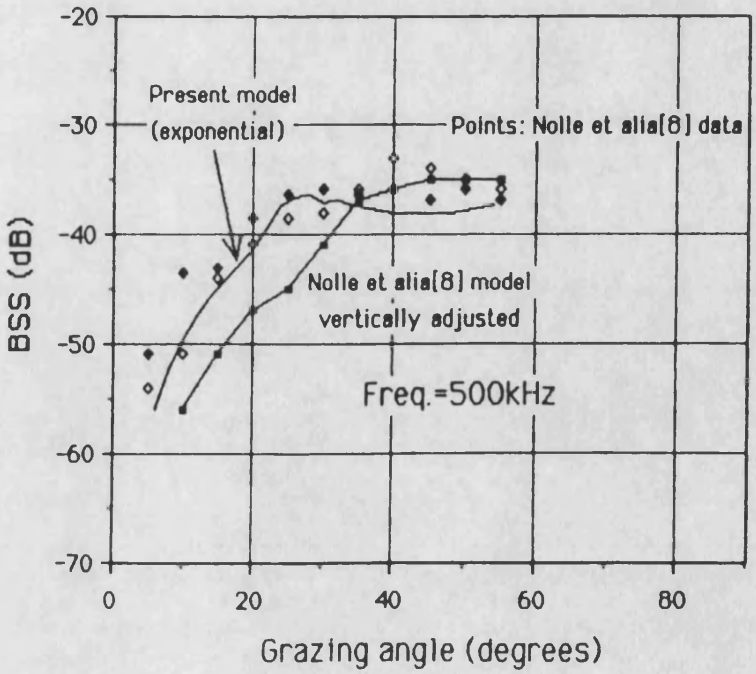

Figure (7.4): Comparison of model and data of Nolle et alia with present model using an exponentially decaying function for N_c.

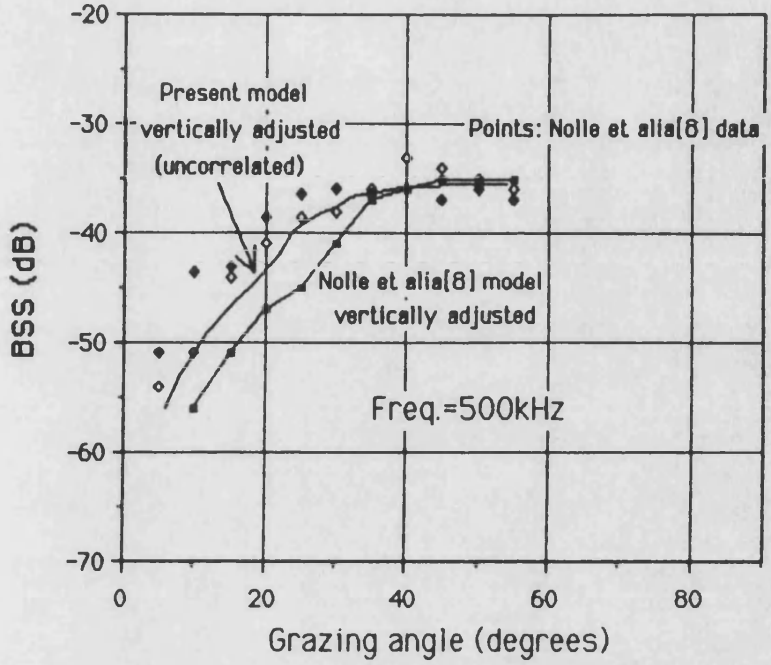

Figure (7.5): Comparison of model and data of Nolle et alia with present model assuming a collection of uncorrelated point scatters for Nc.

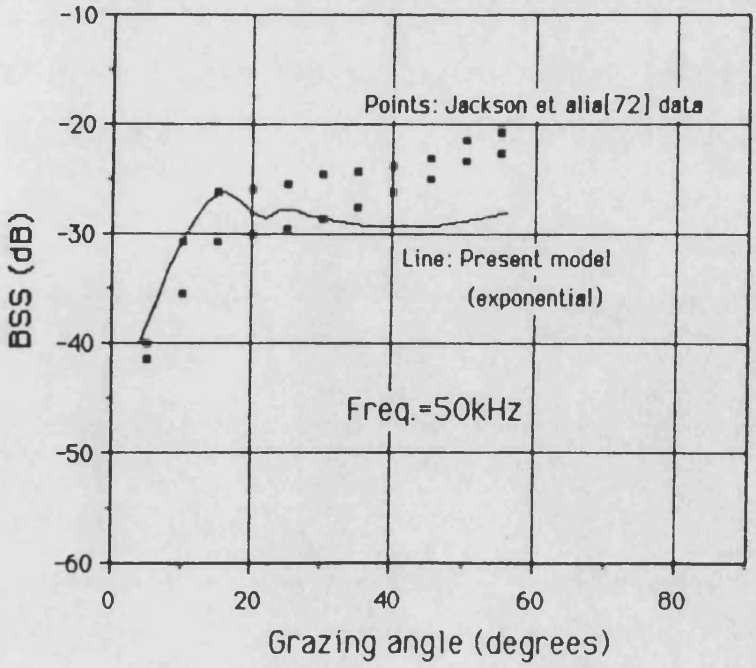

Figure (7.6): Comparison of Jackson et alia data with present model using an exponentially decaying function for Nc.

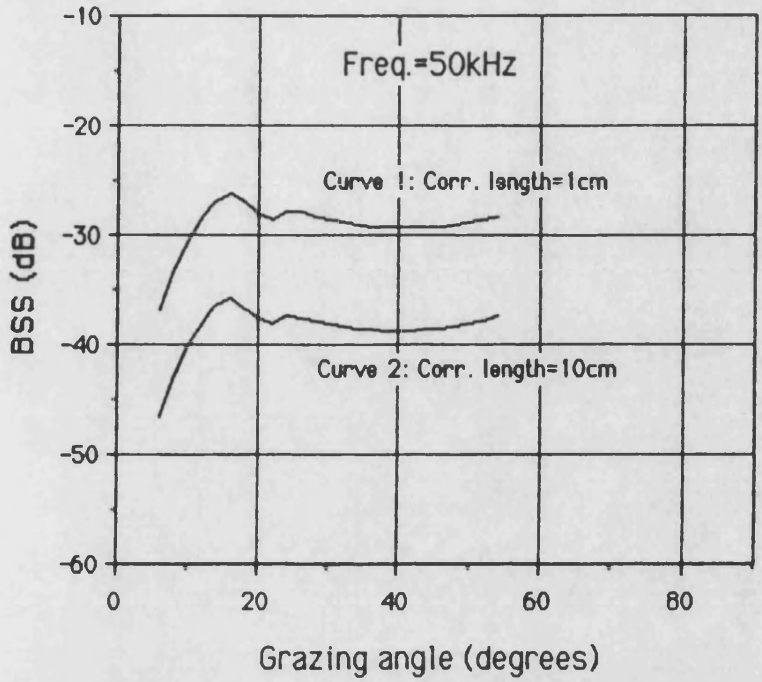

Figure (7.7): The present model evaluated using an exponentially decaying function for Nc with two possible choices for the correlation length.

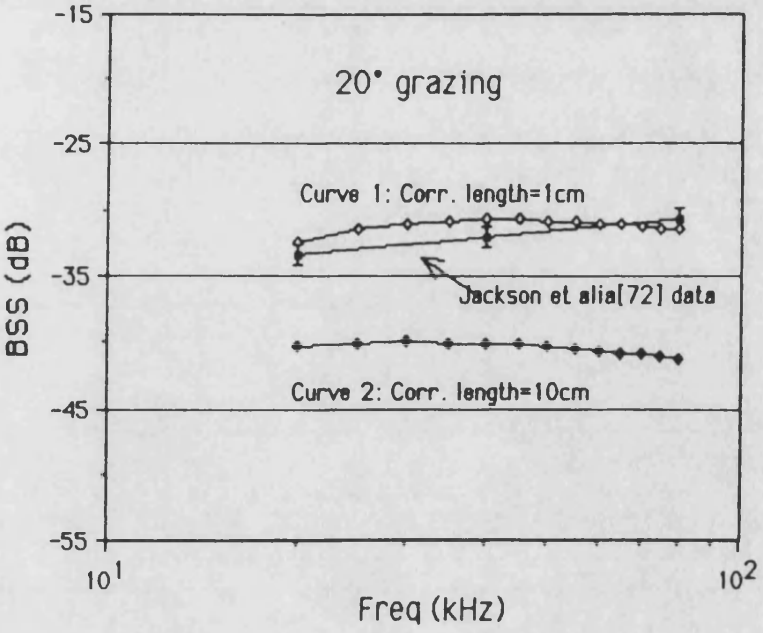

Figure (7.8): Comparison of Jackson et alia data with the present model evaluated using an exponentially decaying function for Nc with two possibile choices for the correlation length.

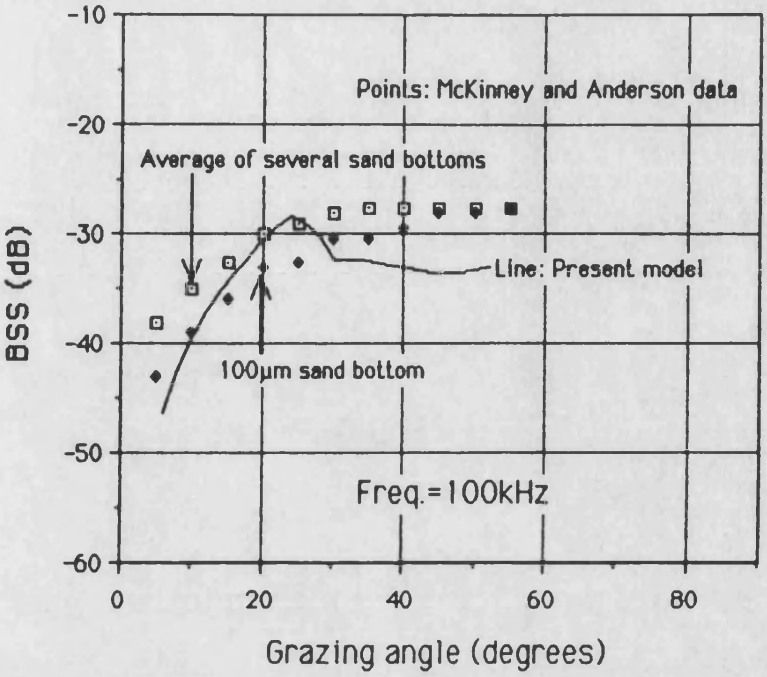

Figure (7.9): Comparison of McKinney and Anderson data with present model evaluated using an exponentially decaying function for Nc.

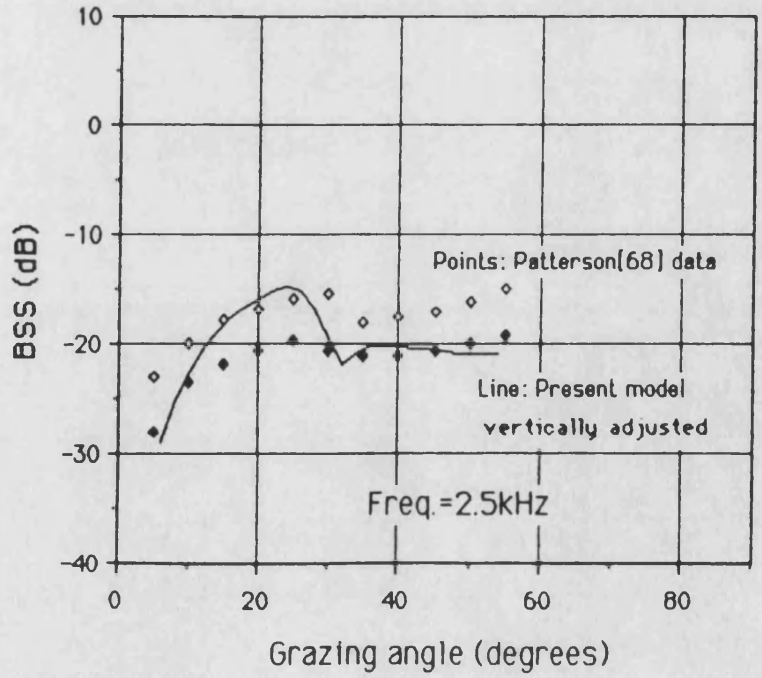

Figure (7.10): Comparison of Patterson data with the present model evaluated using an exponentially decaying function for Nc.

CHAPTER 8

SUMMARY AND CONCLUSIONS

8.1 Summary

In summary, a theoretical model was derived to describe acoustic backscattering of a plane wave incident from water, from the inhomgeneous volume beneath a smooth water/bottom interface. The model was based on an application of the method of small perturbations, in which small variations in the density and acoustic wave speed within the bottom result in acoustic scattering. The variations resulted from fluctuations in concentration; concentration being defined as the ratio of water to sediment in the bottom. A knowledge of both the correlation function and the mean square value of the concentration fluctuations is required to obtain numerical estimates from the model.

There are two particularly important features of the model. First, it accounts for transmission of the incident wave into the bottom at sub-critical grazing angles. This is accomplished by allowing the acoustic wavenumber in the bottom to be complex and then satisfying the usual boundary conditions of continuity of pressure and normal component of velocity. Secondly, it accounts for the re-transmission of scattered *spherical* waves into the water through the *planar* interface. This is accomplished by performing a plane wave decomposition of the spherical wave and approximating it by the sum of a refracted wave and a lateral (or evenescent) wave.

To test the model, an inhomogeneous volume consisting of water-saturated sand was constructed in the laboratory and

placed in a water filled tank. The water/sand interface was made as smooth as possible, to minimize scattering from the interface itself. Measurements of acoustic backscatter from the volume were taken. The correlation function and mean square value of the concentration fluctuations of the bottom were measured and estimates of volume backscatter were obtained from the model. These were compared to the backscatter data. Finally, the model's robustness was examined by comparing model estimates, with a wide range of acoustic backscatter data published in the literature.

8.2 Conclusions

Backscatter data were collected at grazing angles in the range 10° to 90° for the frequency band 25kHz to 200kHz. Across the entire frequency band, volume backscatter resulting from concentration fluctuations in the bottom, dominated the returns at grazing angles less than about 55°. Above 55°, there was evidence that Rayleigh scattering from interface roughness began to contribute increasingly to the backscatter returns, finally dominating the measured backscatter above about 65°.

In the backscatter experiments, a parametric array truncated by the interface was used as the acoustic source, whereas in the model the source was assumed to be a plane wave. Correcting the data for the logarithmic decrease in intensity due to spreading of the parametric beam past truncation, permitted comparison of model and data. Once this correction was made, the model and experimental results were in good agreement at grazing angles less than about 55° for all frequencies examined. At grazing angles greater than 55°, the model was no longer

adequate since the backscatter data was increasingly dominated by scatter from the interface.

A noteworthy feature of the model, is that it predicted *absolute* levels of volume backscatter in accordance with the measured data. Further evidence of the validity of the model is that the peak in the backscatter which it predicted at sub-critical grazing angles was in fact, visible in the data.

The robustness of the model, that is to say, its ability to predict backscatter levels for a range of experimental situations, was tested by comparing it to experimental data in the literature. In all cases model predictions agreed with the data quite well. However to obtain these predictions, it was necessary to estimate both the mean square value and the correlation function of the concentration fluctuations, as no direct information about these parameters was provided in the literature examined.

In conclusion, the theoretical model developed herein provides an accurate description of acoustic backscattering from an inhomogeneous volume beneath a smooth interface. Direct evidence of this is provided by model estimates which agree with backscatter data collected by the author, as well as backscatter data contained in the literature.

APPENDIX A

VALIDITY OF THE FLUID BOTTOM ASSUMPTION

In this appendix, we examine the validity of the fluid bottom assumption employed in the volume backscattering model derived in Chapter 3. The significance of the assumption is that since a fluid cannot support shear waves, one need only consider compressional waves, thereby simplifying the model development. In determining the validity of the assumption, one must examine how much of the transmitted wave is converted to shear waves and how much remains as compressional waves. If shear waves make up only "a small amount" of the transmitted pressure amplitude, then the assumption is reasonable. For the purpose of the present study, less than 10% of the amplitude of the transmitted compressional wave shall be considered "a small amount".

The development contained in Ewing et alia[82] for the transmission of a compressional wave from fluid, into an elastic solid was followed. However, some of the notation they use was altered in order to remain consistant with the present work. Where equations have been taken directly from [82], their equation numbers are given in square brackets. Since only an estimate of the ratio of shear wave to compressional wave pressure is required, bottom inhomogeneities and attenuation shall not be considered.

Figure (A.1) contains a sketch of the problem. A compressional wave incident from water is transmitted into the bottom. Part of the energy is converted into shear waves while part remains in the form of compressional waves. The densities

of the water and sediment bottom are denoted ρ_w and ρ_b respectively. The compressional wave speed in water and the compressional and shear wave speeds in the bottom are denoted c_{wc}, c_{bc}, and c_{bs} respectively.

The pressure ratio of the transmitted *compressional* wave to the incident *compressional* wave, and the pressure ratio of the transmitted *shear* wave to the incident *compressional* wave are given in [82] as:

$$\frac{A_{TC}}{A_{IC}} = \frac{2\rho_w a_w c_{av}^2 (c_{av}^2/c_{bs}^2 - 2)}{\rho_w a_b c_{av}^4/c_{bs}^2 + \mu_b a_w \left[(c_{av}^2/c_{bs}^2 - 2)^2 + 4 a_b b_b \right]} \quad [3\text{-}25] \qquad (A.1)$$

$$\frac{A_{TS}}{A_{IC}} = \frac{-\rho_w a_w a_b c_{av}^2}{\rho_w a_b c_{av}^4/c_{bs}^2 + \mu_b a_w \left[(c_{av}^2/c_{bs}^2 - 2)^2 + 4 a_b b_b \right]} \quad [3\text{-}26] \qquad (A.2)$$

respectively. A_{IC}, A_{TC}, and A_{TS} are the pressure amplitudes of the incident compressional wave, the transmitted compressional wave and the transmitted shear wave respectively and $\mu_b=(c_{bs})^2\rho_b$. The parameter c_{av} is an "apparent velocity along the (interface)" which is related to the various wave speeds via the following set of equations.

$$c_{av} = \frac{c_{wc}}{\cos(\varphi_{IC})} = \frac{c_{bc}}{\cos(\varphi_{TC})} = \frac{c_{bs}}{\cos(\varphi_{TS})} \quad [3\text{-}9] \qquad (A.3)$$

where the grazing angles φ, are depicted in Figure (A.1). Finally, the constants a_w, a_b, and b_b are given by:

$$a_w = \sqrt{\frac{c_{av}^2}{c_{wc}^2} - 1} \; ; c_{av} > c_{wc}$$

$$a_b = \sqrt{\frac{c_{av}^2}{c_{bc}^2} - 1} \; ; c_{av} > c_{bc}$$

$$a_b = -i \cdot \sqrt{1 - \frac{c_{av}^2}{c_{bc}^2}} \; ; c_{av} < c_{bc}$$

$$b_b = \sqrt{\frac{c_{av}^2}{c_{bs}^2} - 1} \; ; c_{av} > c_{bs}$$

$$b_b = -i \cdot \sqrt{1 - \frac{c_{av}^2}{c_{bs}^2}} \; ; c_{av} < c_{bs}$$

[3-10] (A.4)

Dividing Equation (A.2) by (A.1) leads to the following expression for the ratio of the transmitted shear wave pressure to the transmitted compressional wave pressure:

$$\frac{A_{TS}}{A_{TC}} = \frac{2 \cdot a_b}{(c_{av}^2/c_{bs}^2 - 2)} \qquad (A.5)$$

Typical values of compressional and shear wave speeds for a sediment bottom are contained in Hamilton[83]. Using the values he lists for a water-saturated bottom consisting of sand-silt-clay, one obtains $c_{bc} \approx 1600$m/sec, $c_{bs} \approx 400$m/sec. Substituting these values into Equation (A.5), along with an acoustic wave speed in water of $c_{wc} = 1500$m/sec, and the appropriate expressions from Equatons (A.3) and (A.4), permit evaluation of Equation (A.5).

The magnitude in decibels, of the ratio of shear wave to compressional wave pressure for the sand-silt-clay example is plotted in Figure (A.2). From the figure, one can see that even at its peak, the transmitted shear wave pressure is about 25dB lower than the transmitted compressional wave. Thus the

magnitude of the shear wave is only about 5% of the magnitude of the compressional wave and can be ignored for typical water-saturated sediment bottoms.

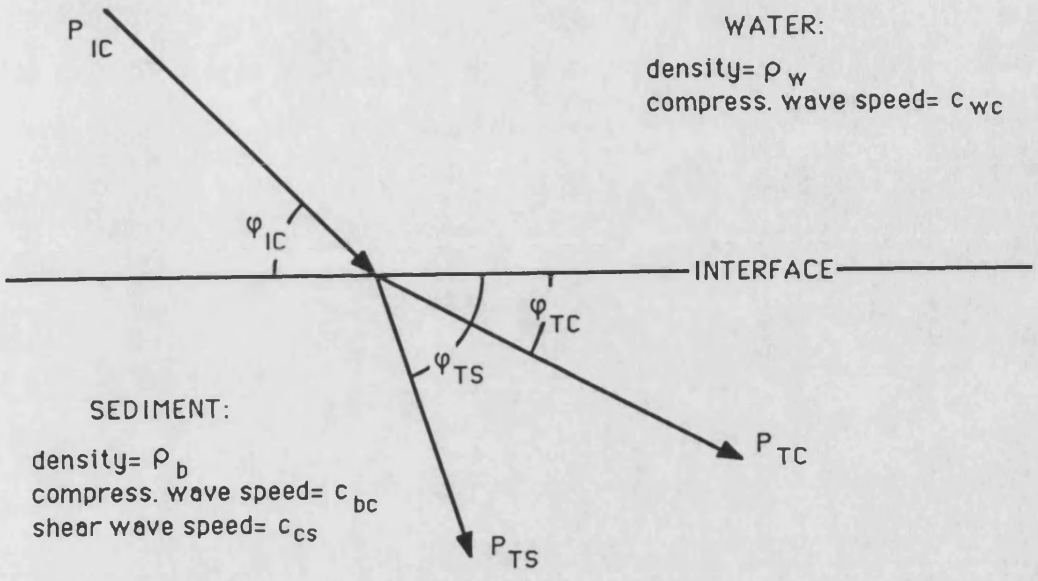

Figure (A.1): Sketch showing compressional wave P_{IC} incident from water, being transmitted into sediment in the form of a compressional wave P_{TC} and a shear wave P_{TS}.

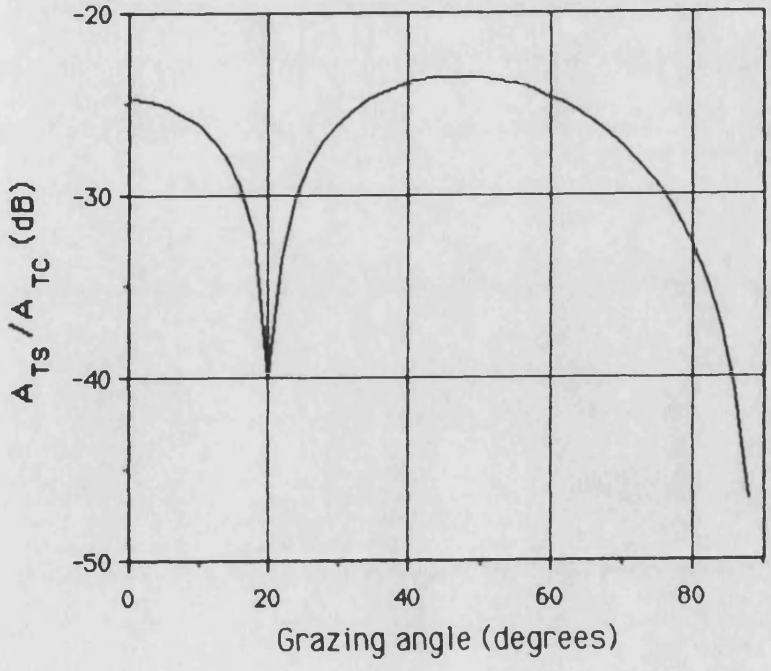

Figure (A.2): Magnitude of shear wave pressure to compressional wave pressure in sediment. The abscissa is the incident grazing angle.

APPENDIX B

PENETRATION OF A SPHERICAL WAVE THROUGH A PLANAR INTERFACE

In this appendix, the penetration of a spherical wave through a planar interface is examined. The wave is assumed to travel from a medium of higher acoustic wave speed (water-saturated sediment) to one of lower acoustic wave speed (water). The procedure followed is to represent the spherical wave as an integral over a plane wave spectrum. Each plane wave is multiplied by the plane wave transmission coefficient to account for penetration through the interface. An approximate solution to the integral is then sought using the method of steepest descents. The solution is first obtained for the case of no attenuation in either medium. The result is then extended to account for attenuation in the sediment.

B.1 Integral Over the Plane Wave Spectrum

Figure (B.1) depicts the geometry of the problem. The interface lies along the line z=0. The receiver R is located on the z axis at height z_w. A source P, located at depth z_s produces the spherical wave. The variables Θ and ψ represent complex angles of incidence and refraction in the plane wave decomposition of the spherical wave. More shall be said about the angle β later.

As stated above, the spherical wave may be represented in the form of an integral over a plane wave spectrum. (See for example Brekhovskikh[84].) Doing this obtains:

$$\frac{e^{i\vec{k}\vec{r}}}{r} = \frac{ik}{2\pi}\int_{0,0}^{\frac{\pi}{2}-i\infty,2\pi} e^{i(k_x x+k_y y+k_z z)} \sin\theta d\theta\, d\varphi \qquad (B.1)$$

where (θ,φ) represent angles in the spherical polar coordinate system and the arrows over k and r represent vector quantities whose magnitudes are k, r. The phase term $i(k_x x+k_y y+k_z z)$ can be obtained from the segment PQR in Figure (B.1).

$$PQR=k_s\{x_T\sin\theta\cos\varphi+y_T\sin\theta\sin\varphi-z_s\cos\theta+z_w(n_{sw}^2-\sin^2\theta)^{1/2}\} \qquad (B.2)$$

where $r_T^2=x_T^2+y_T^2$ and $z_s < 0$ because the point P is below the interface. In order to obtain the pressure at R, the effect of the interface must be included. This is achieved by multiplying each plane wave component by the plane wave transmission coefficient $T_{sw}(\theta)$. This obtains for p_t, the transmitted pressure at R:

$$p_t = \frac{i k_s}{2\pi}\int_{0,0}^{\frac{\pi}{2}-i\infty,2\pi} e^{ik_s(x_T\sin\theta\cos\varphi + y_T\sin\theta\sin\varphi + z_w\sqrt{n_{sw}^2-\sin^2\theta} - z_s\cos\theta)} \cdot T_{sw}(\theta)\sin\theta d\theta d\varphi\,. \qquad (B.3)$$

The integral over $d\varphi$ can easily done to obtain:

$$p_t = i k_s\int_0^{\frac{\pi}{2}-i\infty} J_0(u) e^{ik_s(z_w\sqrt{n_{sw}^2-\sin^2\theta} - z_s\cos\theta)} \cdot T_{sw}(\theta)\sin\theta d\theta \qquad (B.4)$$

where $J_0(u)$ is a Bessel function of order zero and $u=k_s r_T\sin\theta$. Writing the Bessel function as:

$$J_0(u) = [H_0^{(1)}(u) + H_0^{(2)}(u)]/2 \qquad (B.5)$$

where $H_0^{(1)}$, $H_0^{(2)}$ are Hankel functions of the first and second kind, respectively, and noting that $H_0^{(2)}(e^{-i\pi}u)=-H_0^{(1)}(u)$, and $T_{sw}(\theta)=T_{sw}(-\theta)$, allows us to rewrite Equation (B.4) as:

$$p_t = \frac{ik_s}{2}\int_{-\frac{\pi}{2}+i\infty}^{\frac{\pi}{2}-i\infty} e^{ik_s(z_w\sqrt{n_{sw}^2-\sin^2\theta}\ -z_s\cos\theta)}\cdot T_{sw}(\theta)\, H_0^{(1)}(u)\sin\theta d\theta\,. \qquad (B.6)$$

Finally, performing a Taylor expansion on $H_0^{(1)}$ retaining only the leading term results in:

$$p_t \approx e^{i\frac{\pi}{4}}\sqrt{\frac{k_s}{2\pi r_T}}\cdot\int_{-\frac{\pi}{2}+i\infty}^{\frac{\pi}{2}-i\infty} e^{ik_s(r_T\sin\theta\ +z_w\sqrt{n_{ws}^2-\sin^2\theta}\ -z_s\cos\theta)}\cdot$$

$$T_{sw}(\theta)\sqrt{\sin\theta}\, d\theta\,. \qquad (B.7)$$

We may obtain an approximate solution to Equation (B.7) by employing the method of steepest descents (MSD). A discussion of the MSD can be found in almost any text on advanced mathematical methods for physics. (See for example Brekhovskikh[84] or Jefferies and Jefferies[85].) However, in an attempt to keep this appendix self-contained, an overview of the method will be provided before applying it to Equation (B.7).

B.2 The Method of Steepest Descents (MSD)

In the MSD, the contour along which an integral is to be solved may be deformed within certain limits without changing the result. With this in mind, the contour is altered so that the major contribution to the integral occurs in the vicinity of a small number of points known as stationary points. The stationary points can be located as follows:

Given an integral of the form:

$$p_t = {}_c\int e^{\sigma f(\theta)} F(\theta) d\theta \,, \tag{B.8}$$

a new contour is chosen so that the real part of $f(\theta)$ has (at least) one maximum on it, and falls off rapidly away from the location of the maximum. (This contour is a line of steepest descent.) The imaginary and real parts of $f(\theta)$ (assumed analytic) are such that the lines of steepest descent of one are the lines of constant phase of the other. Since we require the line of steepest descent for $\mathcal{Re}\{f(\theta)\}$ this shall be a line of constant phase for $\mathcal{Im}\{f(\theta)\}$. This means that the stationary points are given by the expression:

$$\left.\frac{d[\mathcal{Re}\{f(\theta)\}]}{d\theta}\right|_{\theta=\theta_s} = \left.\frac{d[\mathcal{Im}\{f(\theta)\}]}{d\theta}\right|_{\theta=\theta_s} = 0 \tag{B.9}$$

or more simply:

$$f'(\theta)\Big|_{\theta=\theta_s} = 0. \tag{B.10}$$

A first order approximation to Equation (B.8) is then given by:

$$p_t \approx \sqrt{\frac{\pi}{\sigma}} \sum_{i=1}^{N} e^{\sigma f(\theta_{si})} \Phi(0) \; ; \qquad (B.11)$$

$$\Phi(0) = \sqrt{\frac{-2}{f''(\theta_{si})}} \cdot F(\theta_{si})$$

where θ_{si} represents the ith of N stationary points on the new contour. To apply Equation (B.11) to the present problem, it is necessary to find the path of steepest descent for Equation (B.7) and the stationary points on this path. This is done next.

B.3 The Transmitted Wave: Zero Attenuation

We shall first examine the case for zero attenuation. In this circumstance the acoustic wavenumbers in sand and water are both real. The results for zero attenuation are then extended to obtain a solution when attenuation is present in the sand. Much of what follows is based on unpublished work by H.O. Berktay for a spherical wave travelling from water to sediment through a planar interface. The reverse situation, of interest here, follows fairly directly from his work.

B.3.1 The Stationary Points: Zero Attenuation

To obtain the stationary points, we must solve the equation:

$$\frac{d(f(\theta))}{d\theta} = \frac{d}{d\theta}\left\{ i(r_T \sin\theta + z_w \sqrt{n_{sw}^2 - \sin^2\theta} - z_s \cos\theta) \right\} = 0. \qquad (B.12)$$

Experience has shown that the solution to Equation (B.12) will be made somewhat easier if it is rewritten in terms of ψ, the incident angle in water rather than θ, the incident angle in the sand. Doing this obtains:

$$\frac{d(f(\psi))}{d\psi} = \frac{d}{d\psi}\left\{ i(r_T \sin\psi + z_w \cos\psi - z_s\sqrt{n_{ws}^2 - \sin^2\psi}\ ) \right\} = 0 \qquad \text{(B.13a)}$$

which results in:

$$f'(\psi) = i(r_T \cos\psi - z_w \sin\psi + \frac{z_s(\sin\psi)(\cos\psi)}{\sqrt{n_{ws}^2 - \sin^2\psi}}\ ) = 0. \qquad \text{(B.13b)}$$

One solution to Equation (B.13b) is given by $\psi = \psi_r$, where ψ_r is the (purely real) angle of refraction given by Snells law. That this is so can be shown by noting:

$$\tan\psi_r = r_w/z_w;\ \tan\theta_r = -r_s/z_s; \qquad \text{(B.14a)}$$

$$\sin\theta_r = n_{ws}\sin\psi_r;\ \cos\theta_r = (1 - n_{sw}\sin^2\psi_r)^{1/2} \qquad \text{(B.14b)}$$

and substituting Equations (B.14) into (B.13b). Note that $n_{sw} \equiv 1/n_{ws}$. The value of ψ_r for a given set of parameters is best found numerically.

It is possible to find a second solution to Equation (B.13b) for a complex angle ψ_1. We begin by noting that the first two terms in Equation (B.13b) sum to zero for $r_T\cos\psi = z_w\sin\psi$. This corresponds to the angle β in Figure (B.1) and it is defined as:

$$\beta = \tan^{-1}(r_T/z_w)\ . \qquad \text{(B.15)}$$

We search for a second stationary point of the form:

$$\psi_1 = \beta + \delta_1 \qquad \text{(B.16)}$$

with δ_1 complex and $|\delta_1| << \beta$. Performing a Taylor expansion of the function $f'(\psi_1) = 0$, around β obtains:

$$f'(\psi_1) = f'(\beta+\delta_1) = f'(\beta) + \delta_1 f''(\beta) = 0$$

or (B.17)

$$\delta_1 = -f'(\beta)/f''(\beta).$$

This second stationary point corresponds to the angle of transmission of the lateral wave. To understand when the lateral wave contribution must be included in the solution, it is necessary to examine the steepest descent contour.

B.3.2 The Steepest Descent Contour

Before plotting the contour, we note that $T_{sw}(\psi)$ is double valued by virtue of the term $(1-n_{sw}^2\sin\psi^2)^{1/2}$ in its denominator. This will result in branch lines in the complex ψ plane. When performing the integration along the contour we must insure that it begins and ends on the same Riemann surface. Thus, we shall plot the branch lines as well as the contour to check this.

The branch lines are given by:

$$1-n_{sw}^2\sin^2\psi = q^2;\ 0 \le q \le \infty \quad (B.18)$$

or

$$\sin\psi = (1-q^2/n_{sw}^2)^{1/2} \quad (B.19)$$

where q is real. Rewriting $\sin\psi$ in terms of its real and imaginary parts obtains:

$$\sin\psi = \sin(\psi')\cosh(\psi'') + i\cdot\cos(\psi')\sinh(\psi'') \quad (B.20)$$

where $\psi = \psi' + i\psi''$ and ψ', ψ'' are real. For $q>1$, Equation (B.19) becomes:

$$\sin\psi = \pm i\gamma; \quad \gamma \text{ real.} \tag{B.21}$$

This can only be true if $\psi' = 0$. In the limit of $q=\infty$, we obtain $(\psi',\psi'') = (0,\pm\infty)$. For $q=1$, Equation (B.19) becomes:

$$\sin\psi = 0 \tag{B.22}$$

which is only satisfied if $(\psi',\psi'')=(0,0)$. Finally, for $q=0$, Equation (B.19) becomes:

$$\sin\psi = \pm 1/n_{sw} \tag{B.23}$$

for which we obtain $(\psi',\psi'')=(\pm\psi_c,0)$ where $\psi_c \equiv \sin^{-1}(1/n_{sw})$. Using the information inherent in Equations (B.21) to (B.23) allows a plot of the branch lines to be made. These are represented in Figure (B.2) by the jagged lines along the axes.

To obtain the steepest descent contour, we must solve $\mathfrak{Im}\{f(\psi)\}$ = constant which is equivalent to:

$$\mathfrak{Re}\left\{r_T\sin\psi + z_w\cos\psi - z_s\sqrt{n_{ws}^2-\sin^2\psi}\right\} = \text{constant} \tag{B.24}$$

and plot ψ'' as a function of ψ', taking note of the Riemann surface on which the contour lies. (By convention, the "upper" surface is defined by $(1-n_{sw}^2\sin^2\psi)^{1/2} > 0$ and the "lower" surface by $(1-n_{sw}^2\sin^2\psi)^{1/2} < 0$.) To begin, we shall examine the behaviour of

Equation (B.24) at the limit of ψ'' approaching $\pm\infty$. As ψ approaches $+\infty$, we obtain for Equation (B.24):

$$r_T\sin\psi + z_w\cos\psi - z_s\mathcal{Re}\{\pm i\cdot\sin\psi\} = \text{constant} \qquad (B.25)$$

where we choose $-i\cdot\sin\psi$ for the upper Riemann surface and $+i\cdot\sin\psi$ for the lower Riemann surface. Employing Equation (B.20) and:

$$\cos\psi = \cos\psi'\cosh\psi'' - i\cdot\sin\psi'\sinh\psi'' \qquad (B.26)$$

we rewrite Equation (B.25) as:

$$(r_T\sin\psi' + z_w\cos\psi')\cosh\psi'' + z_s(\pm\cos\psi')\sinh\psi'' = \text{constant}. \qquad (B.27)$$

As ψ'' approaches $+\infty$, $\cosh\psi'' \approx \sinh\psi'' \approx e^{\psi''}/2$. To prevent Equation (B.27) from blowing up, we require the coefficients of $\cosh\psi''$ and $\sinh\psi''$ to sum to zero resulting in:

$$r_T\sin\psi' + z_w\cos\psi' \pm z_s\cos\psi' = 0. \qquad (B.28)$$

This obtains finally, for $\psi''=+\infty$; $\psi'=-\tan^{-1}\{(z_w-z_s)/r_T\}$ on the upper surface and $\psi'=-\tan^{-1}\{(z_w+z_s)/r_T\}$ on the lower surface. Using a similar argument for $\psi''=-\infty$, we obtain $\psi'=\pi-\tan^{-1}\{(z_w-z_s)/r_T\}$ on the upper surface and $\psi'=\pi-\tan^{-1}\{(z_w+z_s)/r_T\}$ on the lower surface. The π enters the expression because the contour approaches $\psi''=-\infty$ in the quadrant $\pi/2 \le \psi' \le \pi$.

Using the expressions developed above for the limits of the (ψ',ψ'') contour, and results obtained employing a digital computer, Equation (B.24) can be plotted. Figure (B.2) depicts the

results for the case $\beta<\psi_c$. The contour begins on the upper Riemann surface, at $(\psi',\psi'')=(-\tan^{-1}\{(z_w-z_s)/r_T\},\infty)$. At $\psi'=0$, it crosses the branch line and enters the lower Riemann surface. (Passage on the lower Riemann surface is denoted by a dashed line.) Continuing on, it crosses the branch line at $\psi''=0$ back unto the upper surface and goes through the stationary point ψ_r. From here the contour continues along on the upper surface to $(\psi',\psi'')=(\pi-\tan^{-1}\{(z_w-z_s)/r_T\},-\infty)$. Thus for $\beta<\psi_c$, the second stationary point does not contribute to the result.

The contour for $\beta>\psi_c$, depicted in Figure (B.3), is somewhat more complicated. Beginning at $(\psi',\psi'')=(-\tan^{-1}\{(z_w-z_s)/r_T\},\infty)$, the contour again procedes along the upper surface to the ψ'' axis where it passes onto the lower surface. Continuing on, it crosses the branch line at $\psi''=0$ back unto the upper surface and goes through the stationary point ψ_r. This time however, the contour curves back on itself, recrosses the ψ' axis and heads back toward the ψ'' axis. It then crosses the ψ'' axis unto the lower surface, whereupon it heads toward the point $(\psi',\psi'')=(-\tan^{-1}\{(z_w+z_s)/r_T\},\infty)$ *still on the lower surface*. By the rules of complex analysis, the contour must begin and end on the same Riemann surface. To accomplish this, a second contour is added. This contour *begins* at the point $(\psi',\psi'')=(-\tan^{-1}\{(z_w+z_s)/r_T\},\infty)$ on the lower surface. It procedes along the lower surface to the ψ'' axis where it crosses unto the upper surface. It then goes through the stationary point ψ_1. Following that, the contour crosses the ψ' axis but this time it remains on the upper surface because the crossing occurs to the right of the branch point at ψ_c. From here,

the contour heads off to the point $(\psi',\psi'')=(\pi-\tan^{-1}((z_w-z_s)/r_T),-\infty)$.

Thus we see that for $\beta<\psi_c$ we must include only the contribution from the refractive stationary point, whereas for $\beta>\psi_c$, the lateral stationary point must be included as well.

B.3.3 The Effects of Attenuation in the Sand on the Result

As discussed in the main body of the text, attenuation is accounted for by making k_s, the acoustic wavenumber in the sand, complex. This in turn, forces n_{ws} to be complex. Doing this modifies the branch lines. Instead of Equation (B.18), we have:

$$|n_{ws}|^2(1+iA)^2 - \sin^2\psi = q^2 \qquad \text{(B.29)}$$

where $n_{ws}\approx|n_{ws}|(1+iA)$ and $A<<1$. Equation (B.29) leads to the following expressions for the real and imaginary parts:

$$|n_{ws}|^2 - (\sin\psi')^2(\cosh\psi'')^2 + (\cos\psi')^2(\sinh\psi'')^2 = q^2 \qquad \text{(B.30a)}$$

and

$$(\sin2\psi')(\sinh\psi'') = 4A\cdot|n_{ws}|^2 . \qquad \text{(B.30b)}$$

The branch lines defined by Equations (B.30) are depicted in Figure (B.4).

The stationary points ψ_r and ψ_l are modified slightly as well. In fact, ψ_r becomes complex and we shall denote it ψ_r.To obtain ψ_r we note that for $A<<1$, we may write:

$$\psi_r = \psi_r + \delta_r;\ |\delta_r| << \psi_r. \qquad \text{(B.31)}$$

Performing a Taylor expansion of the function $f'(\psi_r)=0$ around ψ_r obtains:

$$f'(\psi_r) = f'(\psi_r+\delta_r) = f'(\psi_r) + \delta_r f''(\psi_r) = 0$$

or (B.32)

$$\delta_r = -f'(\psi_r)/f''(\psi_r) .$$

To obtain the modified value of ψ_1, we simply allow n_{ws} to be complex (i.e. n_{ws}) wherever it occurs in Equation (B.17).

Modifications to the contour which result from allowing for attenuation in the sediment are only slight. The contour is still found by the procedure outlined in section B.3.2 except that n_{ws} is made complex wherever necessary. Figure (B.4) contains a plot of the contour for n_{ws} complex and $\beta<|\psi_c|$. The shape of the contour is similar to that of Figure (B.2). This time however, neither the branch lines nor the stationary point ψ_r lie on the coordinate axis.

B.4 Solution of the Transmitted Pressure Integral

Using the procedure outlined above to obtain the stationary points ψ_r and ψ_1, it remains to employ the formuae in section B.2 to secure an expression for $p_t=p_r+p_1$. Comparing Equations (B.7) and (B.8) we have:

$$f(\theta) = i(r_T\sin\theta + z_w\sqrt{n_{sw}^2-\sin^2\theta} - z_s\cos\theta) ,$$

(B.33)

$$F(\theta) = T_{sw}(\theta)\sqrt{\sin\theta} , \quad \text{and} \quad \sigma \approx |k_s| .$$

Performing the required algebra and differentiation, eventually obtains:

$$p_r \approx M_r \exp\left\{ik_s\left(x_T \sin\theta_t + z_w\sqrt{n_{sw}^2 - \sin\theta_t^2} - z_s\cos\theta_t\right)\right\} \qquad (B.34)$$

$$M_r \approx \frac{T_{sw}(\theta_t)\sqrt{\sin\theta_t}}{\sqrt{x_T}\left[x_T\sin\theta_t - z_s\cos\theta_t + z_w\left\{\frac{\cos(2\theta_t)}{\sqrt{n_{sw}^2-\sin^2\theta_t}} + \frac{\sin^2(2\theta_t)}{4(n_{sw}^2-\sin^2\theta_t)^{3/2}}\right\}\right]^{1/2}}$$

$$p_1 \approx M_1 \exp\left\{ik_w\left(x_T\sin\beta + z_w\cos\beta - z_s\sqrt{n_{ws}^2-\sin^2\beta}\right)\right\} \qquad (B.35)$$

$$M_1 \approx \frac{n_{sw}T_{sw}(\beta)\sqrt{\sin\beta}\cos\beta \Big/ \sqrt{1-n_{sw}^2\sin^2\beta}}{\sqrt{x_T}\left[x_T\sin\beta + z_w\cos\beta - z_s\left\{\frac{\cos(2\beta)}{\sqrt{n_{ws}^2-\sin^2\beta}} + \frac{\sin^2(2\beta)}{4(n_{ws}^2-\sin^2\beta)^{3/2}}\right\}\right]^{1/2}}$$

where θ_t is the angle of refraction of the wave in the bottom i.e. $\sin\theta_t = n_{sw}\sin\psi_r$ and the notation $\beta \equiv \psi_1 = \beta + \delta_1$ has been employed to coincide with the main text.

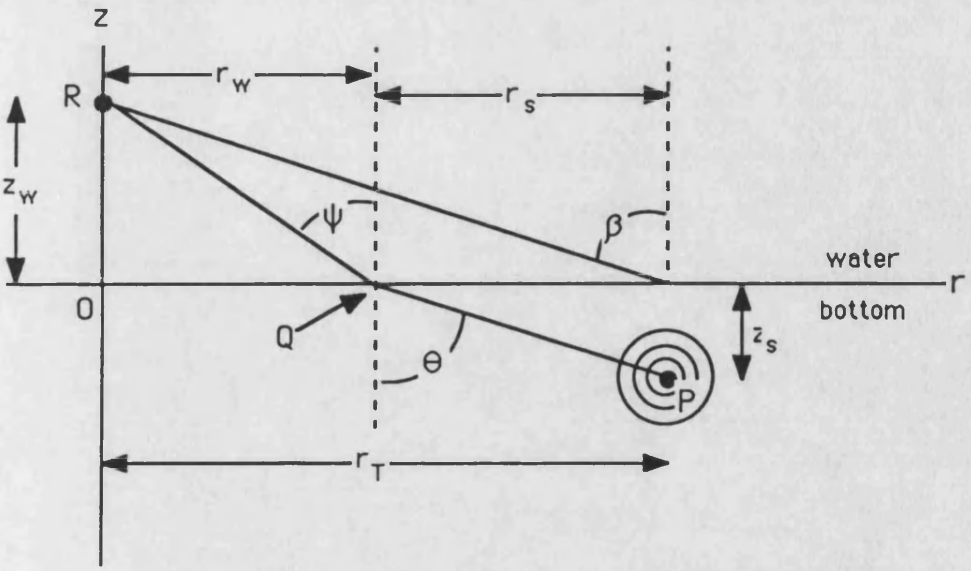

Figure (B.1): Geometry for the problem of a spherical wave penetrating a planar surface.

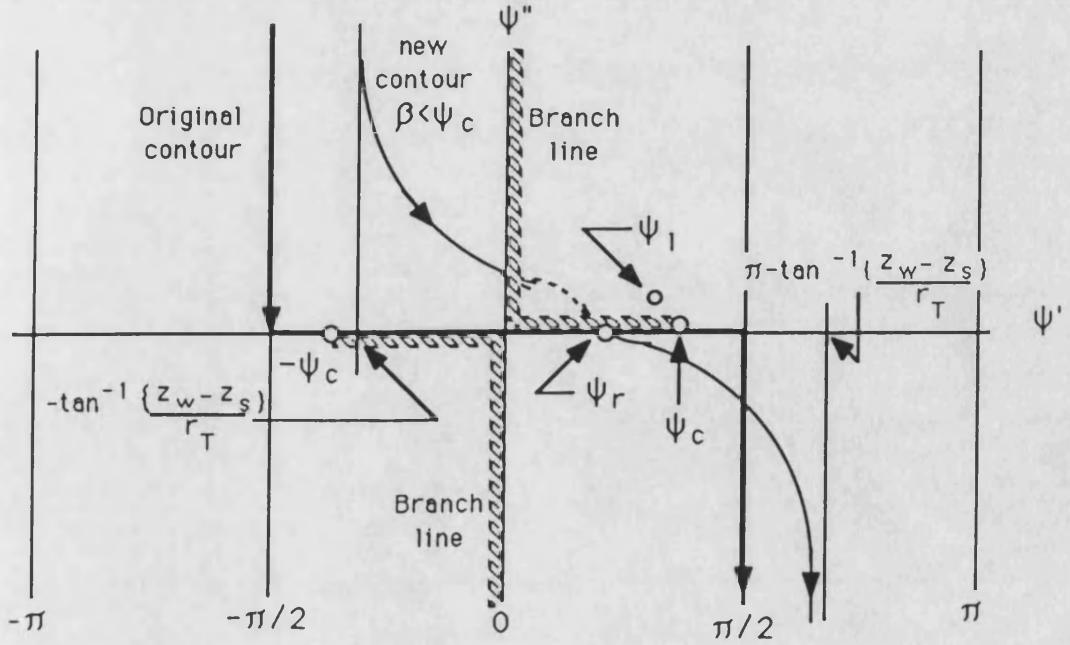

Figure (B.2): Deformed contour for $\beta < \psi_c$. No attenuation.

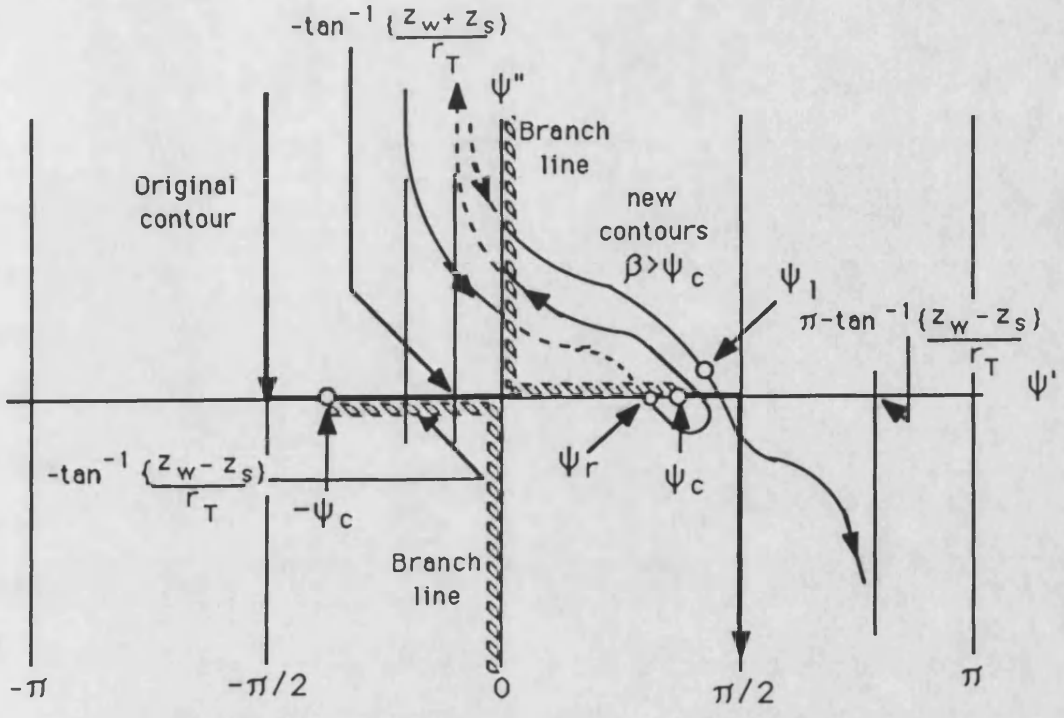

Figure (B.3): Deformed contour for $\beta > \psi_c$. No attenuation.

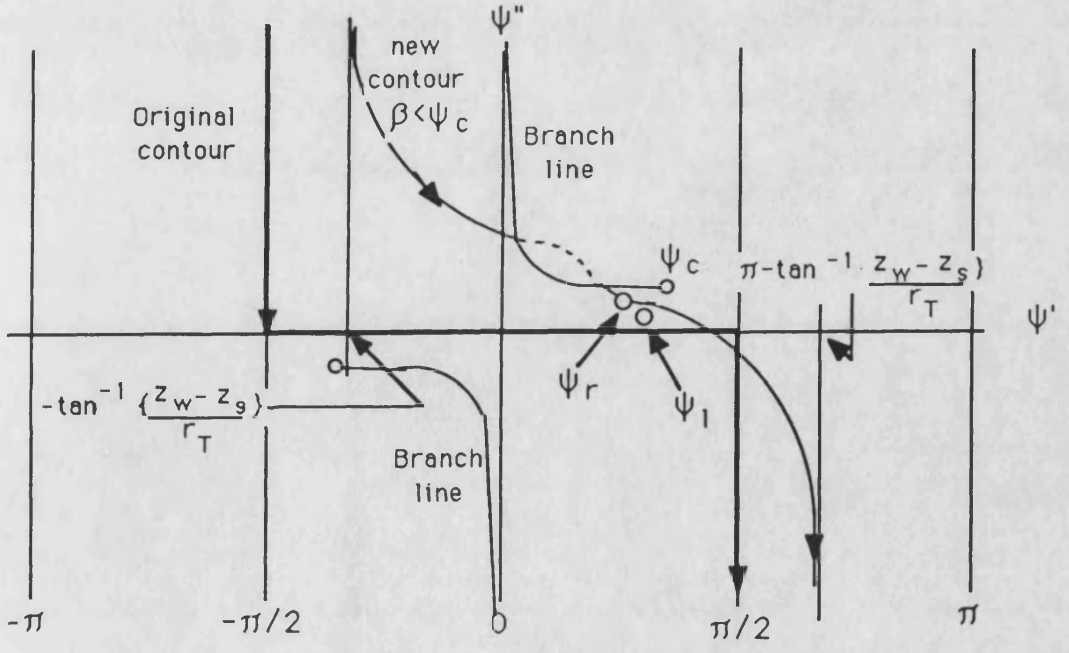

Figure (B.4): Deformed contour for $\beta < \psi_c$. With attenuation in the bottom.

APPENDIX C

POROSITY, CONCENTRATION AND THE RAYLEIGH REFLECTION COEFFICIENT

The purpose of this appendix is three-fold. First, the definitions of porosity and concentration are reviewed and the relationship between them examined. Second, a method is derived which permits estimation of concentration fluctuations in a sand bottom, using measurements of the Rayleigh reflection coefficient. Finally, an empirical formula relating particle size to concentration is obtained enabling estimates to be made of $(\Delta S)^2$, based on the particle size distribution in a sand bottom.

C.1 Relationship Between Porosity and Concentration

Concentration and porosity are closely related. For the case of a water-saturated sediment bottom, they merely represent two different methods of describing the percentages of water and sediment in the bottom. Porosity P, is defined as the ratio of water volume to total volume in a water-saturated bottom; that is:

$$P = V_w/V_b \qquad (C.1)$$

where V_w is the water volume and V_b is the total volume.

Concentration S, is defined as the ratio of the dissolved component (solute) to the component in which it is dissolved (solvent). Considering sediment as the solvent, denoted ρ_{sd}, and water as the solute, denoted ρ_{w*}, we write:

$$S = \rho_{w*}/\rho_{sd}\,. \qquad (C.2)$$

ρ_{sd} is the density of the dry sediment comprising the bottom. By dry sediment we refer to the density of loosely packed sediment (i.e. including gaps between particles) *not* the density of a single particle. This is equivalent to writing:

$$\rho_{sd} = \rho_{ss}\cdot(1-P) \qquad (C.3)$$

where ρ_{ss} *is* the density of the particles. ρ_{w*} is the density of water *as a solute*. That is to say, the density of water corrected for the amount of volume it occupies out of the total volume. This is equivalent to writing:

$$\rho_{w*} = \rho_{w}\cdot P \qquad (C.4)$$

where ρ_w is the density of water. Finally, combining Equations (C2) to (C4) obtains the relationship between porosity and concentration:

$$S = \rho_w\cdot P/\rho_{ss}\cdot(1-P) \text{ or } P = \rho_{ss}\cdot S/(\rho_{ss}\cdot S + \rho_w)\,. \qquad (C.5)$$

C.2 Estimate of Concentration Using Rayleigh Reflection Coefficient

As discussed in Chapter 5, Rayleigh reflection coefficient (RRC) data from the echosounder experiment was used to estimate the concentration fluctuations in the water-saturated sand bottom. In this section, a relationship between the RRC and concentration is obtained, and the method used to convert the RRC data to an estimate of concentration is discussed. In estimating

the concentration from the RRC, the following assumptions are made.

1. Medium 2, the water-saturated sand comprising the bottom, is fluid. ie. it will not support shear waves.
2. The water/bottom interface is smooth.
3. Variations in density and sound speed in medium 1, the water, are negligible.

Kinsler et alia[86] define the RRC as follows:

$$\mathcal{R} = \frac{\frac{\rho_2 c_2}{\rho_1 c_1} - \frac{\cos(\theta_t)}{\cos(\theta_i)}}{\frac{\rho_2 c_2}{\rho_1 c_1} + \frac{\cos(\theta_t)}{\cos(\theta_i)}} \qquad \text{(C.6)}$$

where θ_i is the incident angle, θ_t is the transmission angle, and ρ_1, ρ_2, c_1, and c_2 are the density and sound speeds in medium 1 and 2, respectively. For plane waves originating in water, normally incident on a water-saturated sand bottom, Equation (C.6) reduces to:

$$\mathcal{R} = \frac{\frac{\rho_b c_b}{\rho_w c_w} - 1}{\frac{\rho_b c_b}{\rho_w c_w} + 1} \qquad \text{(C.7)}$$

where the subscripts b and w, refer to the bottom and water respectively.

The acoustic wave speed in the bottom is related to the density of the bottom, according to Clay and Medwin[35] by:

$$c_b = \left[\frac{E_b + \frac{4}{3}G_b}{\rho_b} \right]^{1/2} \qquad (C.8)$$

where E_b and G_b are respectively, the bulk moduli of elasticity and rigidity, of the bottom. For a sand bottom, the ratio $E_b/G_b > 10$; (Hamilton[83]), so that we make the approximation:

$$c_b = (E_b/\rho_b)^{1/2} \qquad (C.9)$$

The density of the bottom, water-saturated sand, is given by:

$$\rho_b = \rho_{ss}(1 - P) + \rho_w P \qquad (C.10)$$

where the various terms have been defined previously. The bulk modulus of elasticity of the bottom consists of three contributing terms:

E_s - the modulus of the sand particles.

E_w - the modulus of the water.

E_f - the modulus of the "frame" formed by the water/sand mixture.

Clay and Medwin[35], derive the total bulk modulus of the bottom, E_b, eventually obtaining the expression:

$$E_b = E_s \cdot (E_f + F)/(E_s + F) \qquad (C.11)$$
$$F = E_w \cdot (E_s - E_f)/(P \cdot (E_s - E_w))$$

Expressions for the three components of E_b are obtained as follows:

$$E_W = \rho_W c_W^2 \qquad (C.12a)$$

by definition. (Values of ρ_W and c_W for the experiment were taken to be 1000kg/m^3 and 1450m/s respectively.) An approximate value of E_F can be obtained from curves by Hamilton[83] contained in Clay and Medwin[35]:

$$E_f = 5{\cdot}10^{10}.e^{-9.5P}\ N/m^2 \qquad (C.12b)$$

where P in the exponent is porosity. Finally Clay and Medwin[35], quote a value from Hamilton[83] for E_s for medium grain sand of:

$$E_s = 5.1{\cdot}10^9\ N/m^2 \qquad (C.12c)$$

Hamilton obtains this value using the "Reuss-Voigt-Hill average for the bulk modulus of the aggregate of mineral grains".

Next, substituting the value for c_b from Equation (C.9) into Equation (C.7), $\mathcal{R}$ is expressed as:

$$\mathcal{R} = \frac{\frac{(\rho_b E_b)^{1/2}}{\rho_W c_W} - 1}{\frac{(\rho_b E_b)^{1/2}}{\rho_W c_W} + 1} \qquad (C.13)$$

Employing Equations (C.10), (C.11) and (C.12) to relate ρ_b and E_b in Equation (C.13) to porosity, and Equation (C.5) to relate porosity to concentration, we obtain the following expression for the relationship of the RRC to concentration:

$$\mathcal{R} = \frac{\left[5.1\cdot10^{9}\cdot(\rho_{ss}(1-P)+\rho_{w}P)\cdot(5\cdot10^{10}\cdot e^{-9.5P}+F)\right]^{1/2} - \rho_{w}c_{w}(5.1\cdot10^{9}+F)^{1/2}}{\left[5.1\cdot10^{9}\cdot(\rho_{ss}(1-P)+\rho_{w}P)\cdot(5\cdot10^{10}\cdot e^{-9.5P}+F)\right]^{1/2} + \rho_{w}c_{w}(5.1\cdot10^{9}+F)^{1/2}}$$

$$F = 0.7\cdot(5.1\cdot10^{9} - 5\cdot10^{10}\cdot e^{-9.5P})/P \; ; \; P = \frac{\rho_{ss}\cdot S}{\rho_{ss}\cdot S + \rho_{w}} \; . \qquad \text{(C.14)}$$

The RRC data collected in the echosounder experiment can be used in Equation (C.14) to obtain corresponding values of concentration. However, the relationship between $\mathcal{R}$ and S given in Equation (C.14), is fairly complicated, and obtaining S explicitly may not even be possible. Instead, a bisection routine was written on a digital computer to solve the equation for each value of the RRC measured. Subtracting out the mean value of S obtained the concentration fluctuations. An autocorrelation was then performed on the concentration fluctuation data to obtain the points plotted in Figures (5.13) to (5.18).

C.3 Relationship Between Particle Size and Concentration

An estimate is required of the concentration fluctuations in a volume of water-saturated sand, based on the size of the sand particles. Data is presented in Thomas and Pace[81] relating the porosity to particle size for five sand grades ranging from 50μm to 500μm. Using Equation (C.5) to relate concentration to porosity, a plot of concentration as a function of particle size was obtained. This is contained in Figure (C.1). The data is in the form of a "log-log" plot to remove any possibility of concentration or particle size becoming negative. The straight line fit to the data in the figure is given by:

$$S = 1.821/D^{0.353} \qquad (C.15)$$

where 'D' is the particle diameter in μm. Equation (C.15) was employed to convert particle diameter to concentration in sections 6.4 and 7.1.

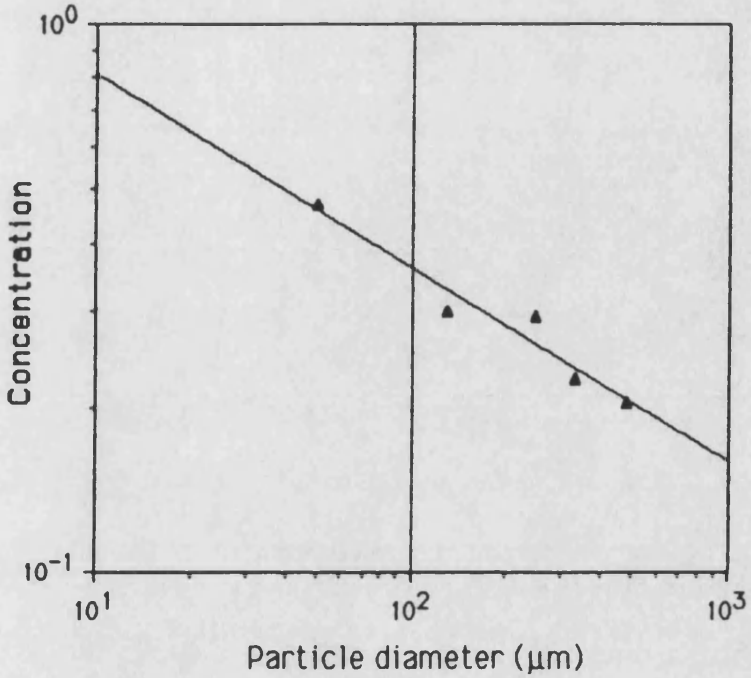

Figure (C.1): Plot of concentration as a function of particle diameter for several grades of sand.

APPENDIX D

SIMPLIFICATIONS TO THE BACKSCATTERING INTEGRAL

When deriving the volume backscatter model in Chapter 3, some details of the mathematics were omitted to avoid interrupting the logical flow of the derivation. In this appendix, these details are presented. First, we shall examine the variable transformation taking Equation (3.21) to (3.27). Following that, the integration by parts performed on Equation (3.27) to yield Equation (3.28) is discussed.

D.1 Variable Transformation of the Backscattering Integral

We wish to transform Equation (3.21) to Equation (3.27). Equation (3.21) is reproduced below as Equation (D.1).

$$I_{sr} \approx \frac{|M_r|^2 |T_{ws}|^2 P_0^2}{16\pi^2} \int_{V_1,V_2} \int \left\{ \left[2\frac{\Delta c_1}{c_0} k_s^2 + i\frac{k_s}{\rho_0} \left\{ \frac{\partial(\Delta\rho_1)}{\partial x_{T1}} \sin\theta_0 - \frac{\partial(\Delta\rho_1)}{\partial z_{s1}} \cos\theta_0 \right\} \right] \cdot \right.$$

$$\left[2\frac{\Delta c_2}{c_0} (k_s^2)^* - i\frac{k_s^*}{\rho_0} \left\{ \frac{\partial(\Delta\rho_2)}{\partial x_{T2}} \sin^*\theta_0 - \frac{\partial(\Delta\rho_2)}{\partial z_{s2}} \cos^*\theta_0 \right\} \right] \cdot$$

$$\exp\left\{ i|k_s| \left[a_r(x_{T1} - x_{T2}) - f_r(z_{s1} - z_{s2}) \right] \right\} \cdot$$

$$\left. \exp\left\{ -|k_s| \left[b_r(x_{T1} + x_{T2}) + 2d_r z_w + g_r(z_{s1} + z_{s2}) \right] \right\} \right\} \, dV_1 dV_2 \quad . \qquad (D.1)$$

We begin by performing the multiplication of the terms in square brackets in Equation (D.1) to obtain:

$$I_{sr} \approx \frac{|M_r|^2 |T_{ws}|^2 P_0^2}{16\pi^2} \int_{V_1,V_2} \int \left[\frac{4|k_s|^4 (\Delta c_1 \Delta c_2)}{c_0^2} + i\frac{2|k_s|^2 k_s^*}{\rho_0 c_0} \cdot \left\{ \frac{\partial(\Delta\rho_1 \Delta c_2)}{\partial x_{T1}} \sin\theta_0 - \right. \right.$$

$$\frac{\partial(\Delta\rho_1\Delta c_2)}{\partial z_{s1}}\cos\theta_0\Big\} - i\frac{2|k_s|^2 k_s}{\rho_0 c_0}\cdot\Big\{\frac{\partial(\Delta\rho_2\Delta c_1)}{\partial x_{T2}}\sin^*\theta_0 - \frac{\partial(\Delta\rho_2\Delta c_1)}{\partial z_{s2}}\cos^*\theta_0\Big\} +$$

$$\frac{|k_s|^2}{\rho_0^2}\Big\{\frac{\partial^2(\Delta\rho_1\Delta\rho_2)}{\partial x_{T1}\partial x_{T2}}|\sin\theta_0|^2 + \frac{\partial^2(\Delta\rho_1\Delta\rho_2)}{\partial z_{s1}\partial z_{s2}}|\cos\theta_0|^2 - \frac{\partial^2(\Delta\rho_1\Delta\rho_2)}{\partial x_{T1}\partial z_{s2}}\sin\theta_0\cos^*\theta_0 -$$

$$\frac{\partial^2(\Delta\rho_1\Delta\rho_2)}{\partial x_{T2}\partial z_{s1}}\sin^*\theta_0\cos\theta_0\Big\}\cdot\exp\Big\{i|k_s|\big[a_r(x_{T1}-x_{T2}) - f_r(z_{s1}-z_{s2})\big]\Big\}\cdot$$

$$\exp\Big\{-|k_s|\big[b_r(x_{T1}+x_{T2}) + 2d_r z_w + g_r(z_{s1}+z_{s2})\big]\Big\}\Big]\ dV_1 dV_2\ . \qquad (D.2)$$

Recall that fluctuations in acoustic wave speed and density are related to a common factor, concentration, S. This relationship is given by:

$$\Delta c = \frac{\partial c}{\partial S}\Delta S, \quad \Delta\rho = \frac{\partial\rho}{\partial S}\Delta S\ . \qquad (D.3)$$

Substituting Equation (D.3) into Equation (D.2) and multiplying the result by $\overline{(\Delta S)^2}/\overline{(\Delta S)^2}$ we obtain:

$$I_{sr} \approx \frac{|M_r|^2|T_{ws}|^2 P_0^2\,\overline{\Delta S^2}}{16\pi^2}\iint_{V_1,V_2}\Big[\frac{4|k_s|^4}{c_0^2}\Big(\frac{\partial c}{\partial S}\Big)^2 N_c + i\frac{2|k_s|^2 k_s^*}{\rho_0 c_0}\frac{\partial c}{\partial S}\cdot\frac{\partial\rho}{\partial S}\Big\{\frac{\partial N_c}{\partial x_{T1}}\sin\theta_0 -$$

$$\frac{\partial N_c}{\partial z_{s1}}\cos\theta_0\Big\} - i\frac{2|k_s|^2 k_s}{\rho_0 c_0}\frac{\partial c}{\partial S}\cdot\frac{\partial\rho}{\partial S}\Big\{\frac{\partial N_c}{\partial x_{T2}}\sin^*\theta_0 - \frac{\partial N_c}{\partial z_{s2}}\cos^*\theta_0\Big\} +$$

$$\frac{|k_s|^2}{\rho_0^2}\Big(\frac{\partial\rho}{\partial S}\Big)^2\Big\{\frac{\partial^2 N_c}{\partial x_{T1}\partial x_{T2}}|\sin\theta_0|^2 + \frac{\partial^2 N_c}{\partial z_{s1}\partial z_{s2}}|\cos\theta_0|^2 - \frac{\partial^2 N_c}{\partial x_{T1}\partial z_{s2}}\sin\theta_0\cos^*\theta_0 -$$

$$\frac{\partial^2 N_c}{\partial x_{T2}\,\partial z_{s1}} \sin^* \Theta_0 \cos\Theta_0 \Big\} \cdot \exp\Big\{ i|k_s| \big[a_r(x_{T1}-x_{T2}) - f_r(z_{s1}-z_{s2}) \big] \Big\} \cdot$$

$$\exp\Big\{ -|k_s| \big[b_r(x_{T1}+x_{T2}) + 2d_r z_w + g_r(z_{s1}+z_{s2}) \big] \Big\} \Big] \; dV_1 dV_2 \qquad (D.4)$$

where the definition of the correlation coefficient, N_c, defined in Equation (3.24) as:

$$N_c = \frac{\overline{\Delta S_1 \Delta S_2}}{\overline{(\Delta S)^2}} \qquad (D.5)$$

has been used to make the equation slightly less cumbersome. Next introduce the relative coordinates (x,y,z):

$$\begin{aligned} x &= x_{T1} - x_{T2} \\ y &= y_{T1} - y_{T2} \\ z &= z_{s1} - z_{s2} \end{aligned} \qquad (D.6a)$$

and the centre of mass coordinates (x',y',z'):

$$\begin{aligned} x' &= (x_{T1} + x_{T2})/2 \\ y' &= (y_{T1} + y_{T2})/2 \\ z' &= (z_{s1} + z_{s2})/2 \end{aligned} \qquad (D.6b)$$

and transform Equation (D.4) to the coordinate systems given by Equations (D.6). To do this we employ the standard relationship for a change of variables. That is, given a function f(s,t) where s=s(u,v), t=t(u,v) one may write:

$$\iint_{x,y} f(s,t)\,ds\,dt = \iint_{u,v} f(s(u,v),t(u,v)) \left|\frac{\partial(s,t)}{\partial(u,v)}\right| du\,dv \qquad (D.7a)$$

where

$$\left|\frac{\partial(s,t)}{\partial(u,v)}\right| = \begin{vmatrix} \frac{\partial s}{\partial u} & \frac{\partial t}{\partial u} \\ \frac{\partial s}{\partial v} & \frac{\partial t}{\partial v} \end{vmatrix} . \qquad (D.7b)$$

(In the transformation discussed above, we obtain a value of unity for Equation (D.7b).) Next, we note that if the fluctuations in concentration within the scattering volume is a stationary process, the correlation coefficient is a function only of the relative coordinates. In this case, we obtain for the derivatives of N_c,

$$\frac{\partial N_c}{\partial x_{T1}} = \frac{\partial N_c}{\partial x} \; ; \; \frac{\partial N_c}{\partial x_{T2}} = -\frac{\partial N_c}{\partial x} \; ; \; \frac{\partial^2 N_c}{\partial x_{T1}\partial x_{T2}} = -\frac{\partial^2 N_c}{\partial x^2}$$

$$\frac{\partial N_c}{\partial z_{s1}} = \frac{\partial N_c}{\partial z} \; ; \; \frac{\partial N_c}{\partial z_{s2}} = -\frac{\partial N_c}{\partial z} \; ; \; \frac{\partial^2 N_c}{\partial z_{s1}\partial z_{s2}} = -\frac{\partial^2 N_c}{\partial z^2} \qquad (D.8)$$

$$\frac{\partial^2 N_c}{\partial x_{T2}\partial z_{s1}} = \frac{\partial^2 N_c}{\partial x_{T1}\partial z_{s2}} - \frac{\partial^2 N_c}{\partial x\,\partial z} \; .$$

Making use of Equations (D.7) and (D.8), the variable transformation of Equation (D.4) to relative and absolute coordinates as defined in Equation (D.6) obtains:

$$I_{sr} \approx \frac{|M_r|^2|T_{ws}|^2 P_0^2(\overline{\Delta S})^2}{16\pi^2} \int_{V,V'} \int \left[\frac{4|k_s|^4}{c_0^2}\left(\frac{\partial c}{\partial S}\right)^2 N_c + \right.$$

$$i\frac{2|k_s|^2}{\rho_0 c_0}\cdot\frac{\partial c}{\partial S}\cdot\frac{\partial \rho}{\partial S}\left\{\frac{\partial N_c}{\partial x}\left(k_s^* \sin\Theta_0 + k_s \sin^*\Theta_0\right) - \frac{\partial N_c}{\partial z}\left(k_s^* \cos\Theta_0 + k_s \cos^*\Theta_0\right)\right\} -$$

$$\frac{|k_s|^2}{\rho_0^2}\left(\frac{\partial \rho}{\partial S}\right)^2\left\{\frac{\partial^2 N_c}{\partial x^2}|\sin\Theta_0|^2 + \frac{\partial^2 N_c}{\partial z^2}|\cos\Theta_0|^2 - \frac{\partial^2 N_c}{\partial x \partial z}\left[\sin\Theta_0 \cos^*\Theta_0 + \sin^*\Theta_0 \cos\Theta_0\right]\right\}\cdot$$

$$\left. \exp\left\{i|k_s|(a_r x - f_r z) - 2|k_s|(b_r x' + d_r z_w + g_r z')\right\}\right] dV\, dV' \qquad (D.9)$$

which is Equation (3.27), the desired result.

D.2 Integration By Parts of the Backscattering Integral

We wish to modify the form of Equation (D.9) to that of Equation (3.28) so that it no longer contains derivatives of N_c. We begin by writing Equation (D.9) in the form:

$$I_{sr} \approx \left\{K_1 \int_V \frac{\partial N_c}{\partial x} + K_2 \int_V \frac{\partial N_c}{\partial z} + K_3 \int_V \frac{\partial^2 N_c}{\partial x^2} + K_4 \int_V \frac{\partial^2 N_c}{\partial z^2} + \right.$$

$$\left. K_5 \int_V \frac{\partial^2 N_c}{\partial x \partial z}\right\} \cdot \exp\left\{i|k_s|(a_r x - f_r z)\right\}\, dV \qquad (D.10)$$

where the K_i's represent constants with respect to the relative coordinates and the integration over the absolute coordinates is included in these constants. We shall now integrate each of the terms in Equation (D.10) by parts. To do this we recall the formula:

$$\int u\,dv = u \cdot v - \int v\,du \qquad (D.11)$$

where u and v are functions of a common variable w, u=u(w), v=v(w). Setting up the first term in Equation (D.10) in this form yields:

$$T_1 \approx K_1 \iint_{y,z} \left[\int_x u\,dv \right] dy\,dz \qquad (D.12)$$

where

$$u(x) = \exp\{i|k_s|(a_r x - f_r z)\}\ ;\ dv(x) = \frac{\partial N_c}{\partial x}\,dx\ . \qquad (D.13)$$

Applying the fomula in Equation (D.11) to the integral in Equation (D.12), we obtain:

$$T_1 \approx K_1 \iint_{y,z} \left[N_c \exp\{i|k_s|(a_r x - f_r z)\} \Big|_{-\frac{L_v}{2}}^{+\frac{L_v}{2}} - i|k_s|a_r \int_{-\frac{L_v}{2}}^{+\frac{L_v}{2}} N_c \exp\{i|k_s|(a_r x - f_r z)\}\,dx \right] dy\,dz \qquad (D.14)$$

where the limits of $\pm L_v/2$ are chosen because in the derivation in Chapter 3, the dimensions of the insonified volume were assumed to be of length L_v. It was further assumed that the correlation length L_c satisfied the inequality $L_c << L_v$ so that the first term in Equation (D.14) is approximately zero at $\pm L_v/2$. This leads to the following expression for T_1:

$$T_1 \approx -iK_1|k_s|a_r \int_V N_c \exp\{i|k_s|(a_r x - f_r z)\}\,dV\ . \qquad (D.15)$$

The effect of the integration has been to introduce the factor "$-i|k_s|a_r$" into the equation. Following an analagous procedure on the second term in Equation (D.10) leads to:

$$T_2 \approx +iK_2|k_s|f_r\int_V N_c \exp\{i|k_s|(a_r x - f_r z)\}\, dV \,. \qquad (D.16)$$

The third, fourth and final terms in Equation (D.10) require repeating the integration by parts a second time. As an example we shall examine the final term in some detail. The first integration is performed on the x variable yielding:

$$T_5 \approx K_5\iint_{y,z}\Big[\frac{\partial N_c}{\partial z}\exp\{i|k_s|(a_r x - f_r z)\}\Big|_{-\frac{L_v}{2}}^{+\frac{L_v}{2}} - i|k_s|a_r\int_{-\frac{L_v}{2}}^{+\frac{L_v}{2}}\frac{\partial N_c}{\partial z}\exp\{i|k_s|(a_r x - f_r z)\}\,dx\Big]dydz \,. \qquad (D.17)$$

Since $L_c << L_v$, the derivative of N_c vanishes at the ends of the insonified volume so that T_5 is simply:

$$T_5 \approx -iK_5|k_s|a_r\int_V \frac{\partial N_c}{\partial z}\exp\{i|k_s|(a_r x - f_r z)\}\, dV \,. \qquad (D.18)$$

Performing a second integration by parts, this time on the z variable, results in:

$$T_5 \approx -iK_5|k_s|a_r \iint_{x,y} \left[N_c \exp\{i|k_s|(a_r x - f_r z)\} \Big|_{-\frac{L_v}{2}}^{+\frac{L_v}{2}} + i|k_s|f_r \int_{-\frac{L_v}{2}}^{+\frac{L_v}{2}} N_c \exp\{i|k_s|(a_r x - f_r z)\}\, dz \right] dx\,dy \qquad (D.19)$$

where as usual, the term containing N_c vanishes at the limits of the volume, obtaining:

$$T_5 \approx K_5|k_s|^2 a_r f_r \int_V N_c \exp\{i|k_s|(a_r x - f_r z)\}\, dV\,. \qquad (D.20)$$

Following this procedure for the third and fourth terms in Equation (D.10), collecting terms, and replacing the K_i's with their appropriate values, finally obtains:

$$I_{sr} \approx C_r \cdot \int_{V,V'} \left[D_r(x',z') N_c \exp\left\{ i|k_s|(a_r x - f_r z) - 2|k_s|(b_r x' + d_r z_w + g_r z') \right\} \right] dV\, dV'$$

$$C_r = \frac{|M_r|^2 |T_{ws}|^2 P_0^2 (\overline{\Delta S})^2 |k_s|^4}{16\pi^2} \qquad (D.21)$$

$$D_r(x',z') = \left[\frac{4}{c_0^2}\left(\frac{\partial c}{\partial S}\right)^2 + \frac{4}{\rho_0 c_0} \cdot \frac{\partial c}{\partial S} \cdot \frac{\partial \rho}{\partial S} \left\{ a_r \Re e\{(1-iA)\sin\Theta_0\} + f_r \Re e\{(1-iA)\cos\Theta_0\} \right\} + \right.$$

$$\left. \frac{1}{\rho_0^2} \cdot \left(\frac{\partial \rho}{\partial S}\right)^2 \left\{ a_r^2 |\sin\Theta_0|^2 + f_r^2 |\cos\Theta_0|^2 + 2a_r f_r \Re e\{\sin\Theta_0 \cos^*\Theta_0\} \right\} \right]$$

which is Equation (3.28), the required result.

APPENDIX E

THE MONTE CARLO INTEGRATION TECHNIQUE

There are several two-dimensional integrals contained in Chapter 3 which the author has not been able to solve analytically. Solutions of these integrals are required in order to obtain numerical estimates from the volume backscattering model. The Monte Carlo integration technique was chosen as an effective method of solving the integrals empirically. In this appendix, the method of Monte Carlo integration is reviewed and the technique is examined as it applies to the present problem.

Suppose there is a function f(x,y) which we wish to integrate over an area A. If we select a point within the area at random, call it $p_1=(x_1,y_1)$, and solve the equation:

$$I \approx f(p_1)\cdot A \tag{E.1}$$

we would have an estimate, albiet extremely crude, of the integral we which to solve; that is:

$$I = \int_A f(x,y)\, dA\ . \tag{E.2}$$

One may improve upon the estimate by solving Equation (E.1) at a large number of random points within area A, and averaging the result. In the limit of the number of points going to infinity, one obtains:

$$I = \lim_{N\to\infty} \frac{1}{N} \sum_{i=1}^{N} f(p_i)\cdot A = \int_A f(x,y)\, dA\ . \tag{E.3}$$

For $N < \infty$, Press et alia[87] approximate the error on 'I' as:

$$I \approx \frac{1}{N}\sum_{i=1}^{N} f(p_i)\cdot A \pm \sqrt{\frac{\langle f^2\rangle - \langle f\rangle^2}{N}}\cdot A \qquad (E.4)$$

where

$$\langle f\rangle \equiv \frac{1}{N}\sum_{i=1}^{N} f(p_i)\ ;\quad \langle f^2\rangle \equiv \frac{1}{N}\sum_{i=1}^{N} f^2(p_i)\ . \qquad (E.5)$$

For the backscatter problem, the area over which the integral was to be performed, was approximated by a rectangle, the dimensions of which are depicted in Figure (E.1) by the solid lines. The width of the rectangle is the -3dB beamwidth, and the length is $c_0\tau/2$ where c_0 is the average acoustic wave speed in the bottom and τ is the pulselength. Interest in the present study was primarily in backscatter at low grazing angles. At low grazing, the beam is refracted almost parallel to the interface. For this reason, the area of integration was further simplified to a rectangle whose length was parallel to the interface. This area is depicted by the dashed lines in the figure.

A Fortran computer program was written and the integrations performed on a digital computer with N large enough that the resulting error in 'I' was less than ±0.25dB. (In the event, N=75 proved sufficiently large.)

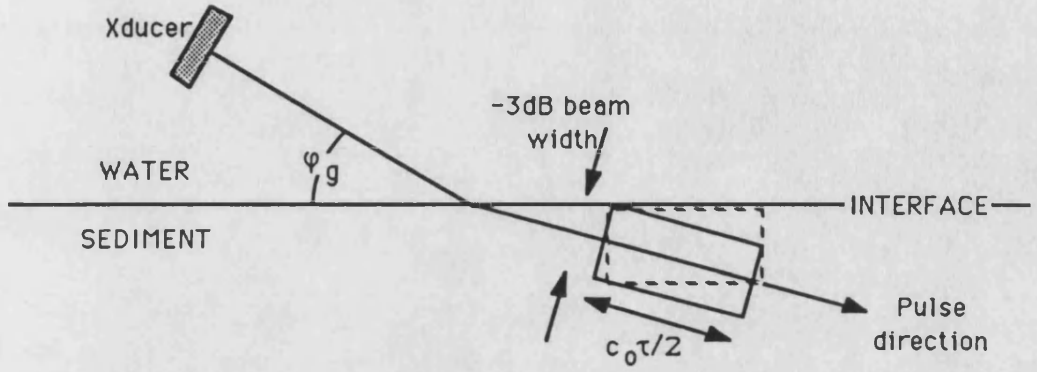

Figure (E.1): Sketch showing area insonified, to the -3dB width (solid rectangle) and area used in Monte Carlo integration (dashed rectangle).

APPENDIX F

CONSTANTS NEEDED IN THE VOLUME BACKSCATTER MODEL

In this appendix, physical constants required to obtain numerical estimates from the volume backscatter model derived in Chapter 3 are presented. The constants tabulated are for the present experimental setup and those from the published literature discussed in Chapter 7.

The appendix consists of two sections. In the first, values for acoustic wave speed, density, and attenuation are tabulated. In the second, the dependence of density and acoustic wave speed on concentration is estimated.

F.1 The Physical Constants

Below is a list of the physical constants for the bottom volume used by the author in his backscatter experiments. Following that, the physical constants (or estimates of them) are listed for the bottom volumes used by other scientists in backscatter experiments which have been discussed by the author.

PRESENT EXPERIMENT: Bottom consisted of many sand layers. Each layer consisted of one of four possible sand grades, each grade having a different mean particle diameter.

TABLE F.1

Particle dia.(μm)	Density (ρ_b m/kg^3)	Wave speed (c_b m/sec)	Attenuation $(A_0)'$
50	1750*	1538*	$13.2 \cdot 10^{-3}$ *
130	1940*	1628*	$11.2 \cdot 10^{-3}$ *
250	1946*	1660*	$9.43 \cdot 10^{-3}$ *
600	2138††	1778††	$7.76 \cdot 10^{-3}$ ††
Average	1944	1651	$10.4 \cdot 10^{-3}$

NOLLE ET ALIA[8]: Bottom consisted of a single sand grade with a mean particle diameter of 115μm.

TABLE F.2

Particle dia.(μm)	Density (ρ_b m/kg^3)	Wave speed (c_b m/sec)	Attenuation $(A_0)'$
115	1940#	1628#	$11.2 \cdot 10^{-3}$ #

JACKSON ET ALIA[72]: Bottom consisted of silty sand. Particles varied in size from about 10μm-1000μm.

TABLE F.3

Particle dia.(μm)	Density (ρ_b m/kg^3)	Wave speed (c_b m/sec)	Attenuation $(A_0)'$
10-1000	1740§	1590§	$10.7 \cdot 10^{-3}$

MCKINNEY & ANDERSON[69]: Data collected at several locations with differing bottom types. Model evaluated for the average of the data collected from all their sand bottoms. The sand particles ranged in size from about 10μm-1000μm.

TABLE F.4

Particle dia.(μm)	Density (ρ_b m/kg^3)	Wave speed (c_b m/sec)	Attenuation $(A_0)^\dagger$
10-1000	1944 §§	1651 §§	$10.4 \cdot 10^{-3}$ §§

PATTERSON[68]: No indication of bottom type given.

TABLE F.5

Particle dia.(μm)	Density (ρ_b m/kg^3)	Wave speed (c_b m/sec)	Attenuation $(A_0)^\dagger$
unknown	2000§	1740§	≈0

† Attenuation is accounted for by making the acoustic wave-number in the bottom complex so that $k_b \equiv \omega/c_0 \cdot (1 \pm iA_0)$.

* Taken from Thomas and Pace[81].

†† Extrapolated from values in Thomas and Pace[81].

* Used the values for 130μm sand from Thomas and Pace[81].

§ Paper actually gives the ratios c_b/c_w and ρ_b/ρ_w. The tabulated values were calculated assuming $c_w = 1500$m/s, $\rho_w = 1000$kg/m^3.

§§ The average of the constants for five sand grades in the range 50-500μm from Thomas and Pace[81] was used.

F.2 Estimate of $\partial\rho/\partial S$ and $\partial c/\partial S$ for Water-saturated Sand

Along with the constants tabulated above, an estimate is required of the rates of change of density and acoustic wave

speed with concentration, in the inhomogeneous medium. These are denoted $\partial\rho/\partial S$ and $\partial c/\partial S$ respectively. (See Equation 3.27.)

We begin by noting that Thomas and Pace[81] tabulate data for porosity, density and acoustic wave speed for five water-saturated sand grades. The mean particle diameters of the various sand grades range from 50-500μm. This represents almost the entire range of sands comprising the scattering volumes examined in the present paper. Therefore, estimates of $\partial\rho/\partial S$ and $\partial c/\partial S$ based on their data should provide acceptable values for our analysis. Employing the relationship between porosity and concentration given by Equation (C.5), the porosity values in [81] were converted to concentration. Table F.6 lists the values for porosity, density and acoustic wave speed taken from reference [81], along with the values of concentration obtained using Equation (C.5).

TABLE F.6

Particle dia.(μm)	Density (ρ_b m/kg^3)	Wave speed (c_b m/sec)	Porosity (P)	Concentration (S)
50	1750	1538	0.550	0.468
130	1940	1628	0.437	0.300
250	1946	1660	0.432	0.293
330	2018	1705	0.379	0.226
480	2072	1762	0.350	0.203

The density and wave speed are plotted as functions of concentration in Figures (F.1) and (F.2) respectively. Straight lines were mached to the data using a least squares fit. The

agreement between the fitted lines and the data is acceptable in both cases. From Figure (F.1) we obtain:

$$\rho_b = 2270 kg/m^3 - 1100 kg/m^3 \cdot S \qquad (F.1)$$

and from Figure (F.2) we obtain:

$$c_b = 1880 m/s - 750 m/s \cdot S \qquad (F.2)$$

for the equations of the straight lines fit to the data. This results in the following values for $\partial\rho/\partial S$ and $\partial c/\partial S$:

$$\partial\rho/\partial S = -1100 kg/m^3 \; ; \partial c/\partial S = -750 m/s \; . \qquad (F.3)$$

The estimates of $\partial\rho/\partial S$ and $\partial c/\partial S$ given by Equation (F.3) were used each time the volume backscattering model was evaluated.

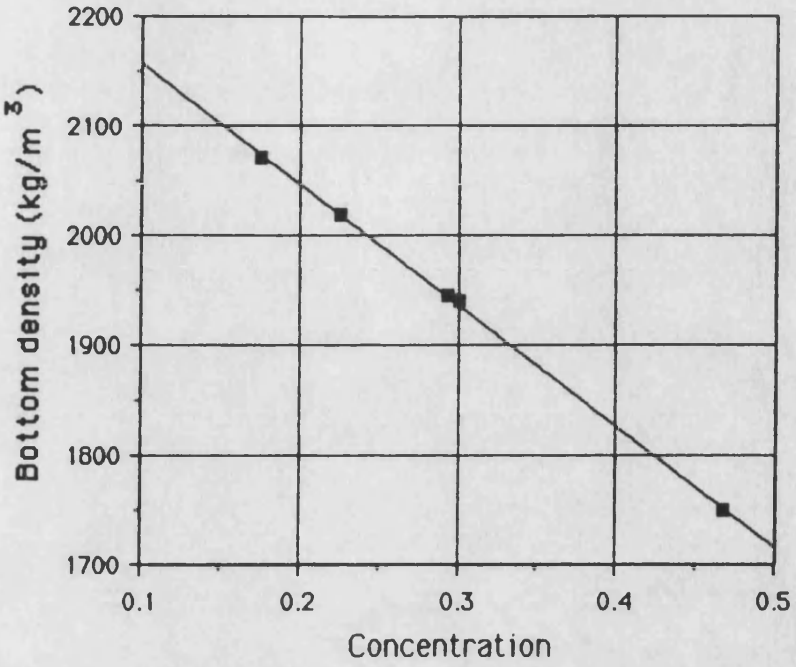

Figure (F.1): Plot of density vs. concentration for water-saturated sands. Mean particle diameters range from 50-500µm.

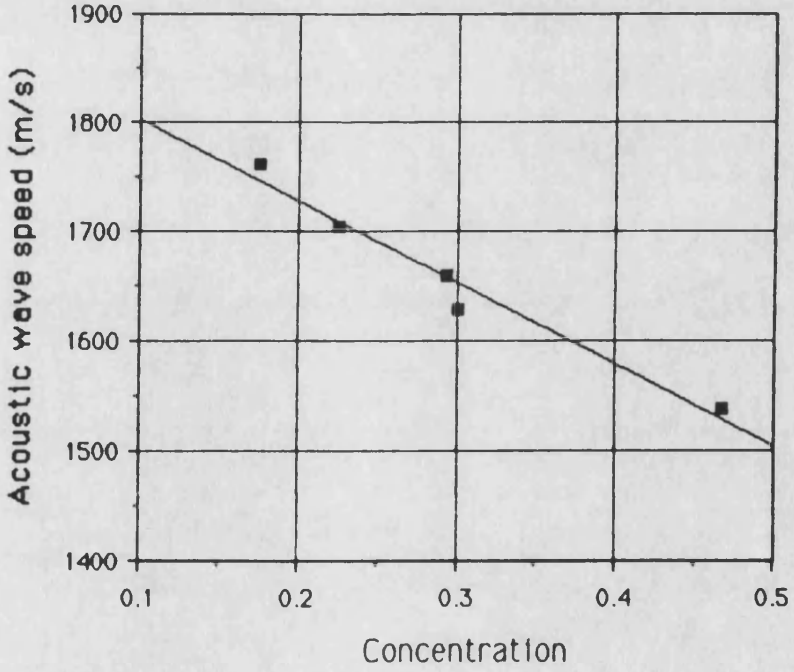

Figure (F.2): Plot of wave speed vs. concentration for water-saturated sands. Mean particle diameters range from 50-500µm.

REFERENCES

1. Heaps, H.S., "Non-Specular Reflection of Sound from a Sinusoidal Surface", JASA, 27, 698-705, 1955.

2. Eckart, C., "The Scattering of Sound from the Sea Surface", JASA, 25, 566-570, 1953.

3. Marsh, H.W., "Exact Solution of Wave Scattering by Irregular Surfaces", JASA, 33, 330-333, 1961.

4. Horton, C.W., Mitchell, S.K., Barnard, G.R., "Model Studies on the Scattering of Acoustic Waves from a Rough Surface", JASA, 41, 635-643, 1967.

5. Thorne, P.D., "Broadband Studies of Acoustic Scattering from a Model Rough Surface", Ph.D. Thesis, Bath U., Bath, England, 1982.

6. LaCasce, E.O., Tamarkin, P., "Underwater Sound Reflection from a Corrugated Surface", J. Applied Phys., 27, 138-148 1956.

7. Stockhausen, J.H., "Scattering from the Volume of an Inhomogeneous Half-Space", NRE Report, 63/9, 1963.

8. Nolle, A.W., Hoyer, W.A., Mifsud, J.F., Runyan, W.R., Ward, M.B., "Acoustic Properties of Water-Filled Sands", JASA, 35, 1394-1408, 1963.

9. Crowther, P.A., "Some Statistics of the Sea-Bed and Acoustic Scattering Therefrom", Acoustics and the Sea-Bed, ed. N.G. Pace, Bath U., Bath, 1983.

10. Ivakin, A.N., Lysanov, Yu. P., "Theory of Underwater Sound Scattering by Random Inhomogeneities of the Bottom", Soviet Physics-Acoustics, 27, 61-64, 1981.

11. Chernov, L.A., Waves in Randomly Inhomogeneous Media, [in Russian], Nauka, Moscow, 1975.

12. Strutt, J.W., The Theory of Sound, Dover, New York, 1945.

13. Uretsky, J.L., "Reflection of a Plane Sound Wave from a Sinusoidal Surface", JASA, 35, 1293

14. Meecham, W.C., "Variational Methods for the Calculation of the Distribution of Energy Reflected from a Periodic Surface", J. Applied Phys., 361-367, 1956.

15. Rice, S.O., "Reflection of Electromagnetic Waves from Slightly Rough Surfaces", The Theory of Electromagnetic Waves, A Symposium, Interscience New York, 351-378, 1951.

16. Wiener, N., Extrapolation, Interpolation and Smoothing of Stationary Time Series, Wiley, New York, 1960.

17. Marsh, H.W., Schulkin, M., Kneale, S.G., "Scattering of Underwater Sound by the Sea Surface", JASA, 33, 334-340, 1961.

18. Neumann, G., Tech. Memo. No. 43, Beach Erosion Board, 1953.

19. Marsh, H.W., "Non-Specular Scattering of Underwater Sound by the Sea Surface", Lecture 11, Underwater Acoustics: Proceedings of the NATO Institute at Imperial College, 193-197, ed. V.M. Albers, Plenum Press, New York, 1962.

20. Marsh, H.W., "Sound Reflection and Scattering From the Sea Surface", JASA, 35, 240-244, 1963.

21. Phillips, O.M., "The Equilibrium Range in the Spectrum of Wind-Generated Ocean Waves", J. Fluid Mech. 4, 1958.

22. Burling, R.W., "Wind Generation of Waves on Water", Ph.D. Thesis, Imperial College, U. of London, 1955.

23. Kuo, E.Y.T., "Wave Scattering and Transmission at Irregular Surfaces", JASA, 36, 2135-2142, 1964.

24. Urick, R.J., Saling, D.S., "Backscattering of Explosive Sound from the Deep-Sea Bed", JASA, 1962.

25. Kuo, E.Y.T., "The Effects of Boundary Surface Inhomogeneities on Acoustic Scattering. 1. Theory", JASA, 81, 1762-1766, 1987.

26. Roderick, W.J., Dullea, R.K., "High Resolution Bottom Backscatter Measurements", Naval Underwater Systems Center, TD 7181, 1984.

27. Jackson, D.R., Winebrenner, D.P., Ishimaru, A., "Comparison of Perturbation Theories For Rough Surface Scattering", JASA, 83, 961-969, 1988.

28. Mitzner, D., "Discussion of the Paper by C. Eckart on Sea Surface Scattering", JASA, 25, 1015(L), 1953.

29. Meecham, W.C., "On the Use of the Kirchhoff Approximation for the Solution of Reflection Problems", J. Rational Mech., 5, 323-334, 1956.

30. McDaniel, S.T., Gorman, A.D, "An Examination of the Composite- Roughness Scattering Problem", JASA, 73, 1476-1486, 1983.

31. Clay, C.S., "Fluctuations of Sound Reflected from the Sea Surface", JASA, 32, 1547-1551, 1960.

32. Beckmann, P., Spizzichino, A., The Scattering of Electromagnetic Waves from Rough Surfaces, Pergamon Press, New York, 1963.

33. Bass, F.G., Fuks, I.M., Wave Scattering from Statistically Rough Surfaces, Pergamon Press, Oxford, 1979.

34. Jackson, D.R., Winebrenner, D.P., Ishimaru, "Application of the Composite Roughness Model to High Frequency Bottom Backscattering", JASA, 79, 1410-1422, 1986.

35. Clay, C.S., Medwin, H., Acoustical Oceanography: Principles and Applications, Wiley-Interscience, New York, 1977.

36. Thorne, P.D., Pace, N.G., "Acoustic Studies of Broadband Scattering from a Model Rough Surface", JASA, 75, 133-144, 1984.

37. Pace, N.G., Al-Hamdami, Z.K.S., Thorne, P.D., "The Range Dependence of Normal Incidence Acoustic Backscatter from a Rough Surface", JASA, 77, 101-112, 1985.

38. Al-Hamdami, Z.K.S., "Laboratory Studies of Underwater Acoustic Backscattering from Rough Surfaces", Ph.D. Thesis, Bath U., Bath, England, 1984.

39. Kuperman, W.A., "Coherent Component of Specular Reflection and Transmission at a Randomly Rough Two-Fluid Interface", JASA, 58, 365-370, 1975.

40. Bass, F.G., "Izv. Vyssh. Uchebn. Zaved Radiofitz.", 4, 476, 1961; (JPRS: 10223).

41. Kur'yanov, B.F., "The Scattering of Sound at a Rough Surface with Two Types of Irregularity", Soviet Physics-Acoustics, 8, 252-257, 1963.

42. Bachmann, W., "A Theoretical Model for the Backscattering Strength of a Composite-Roughness Sea Surface", JASA, 54, 712-716, 1973.

43. Beckmann, P., "Shadowing of Random Rough Surfaces", Trans. IEEE Antennas Propagation, 13, 284-288, 1965.

44. Wagner, R.J., "Shadowing of Randomly Rough Surfaces", JASA, 41, 138-147, 1967.

45. Brockelman, R.A., Hagfors, T., "Note on the Effect of Shadowing on the Backscattering of Waves from a Random Rough Surface", Trans. IEEE Antennas Propagation, 14, 621-629, 1966.

46. Smith, B.G., "Geometrical Shadowing of a Random Rough Surface" Trans. IEEE Antennas Propagation, 15, 668-671, 1967.

47. Shumway, G., "Sound, Speed and Absorption Studies of Marine Sediments by a Resonance Method- Parts 1 and 2", Geophysics, 25, 451 and 659, 1960.

48. Morse, P.M., Vibration and Sound, p.354, McGraw Hill, New York, 1948.

49. Merklinger, H. M., "Bottom Reverberation Measured With Explosive Charges Fired Deep in the Ocean", JASA, 44, 508-53, 1968.

50. Buckley, J.P., Urick, R.J., "Backscattering from the Deep Sea-Bed at Small Grazing Angles", JASA, 44, 648-650, 1968.

51. Crowther, P.A., "Underwater Acoustic Boundary Scattering", A.B. Wood Lecture, Institute of Acoustics, and sources cited therein, 1977.

52. Wyber, R.J., "The Dependence of Bottom Backscattering on the Structure of a Layered Scattering Medium", JASA, 78, 665-671, 1985.

53. Volovov, V.I., Zhitkovskii, Yu.Yu., "Reflection and Scattering of Sound by the Ocean Bottom", p.395 in Ocean Acoustics Part 6, (in Russian), ed. L.M. Brekhovskikh, Moscow,1974.

54. Hamilton, E.L., "Compressional Wave Attenuation in Marine Sediments", Geophysics, 37, 620-646, 1972.

55 Lysanov, Yu.P., "Geoacoustic Model of the Upper Sediment Layer in Shallow Seas", Dokl. Akad. Nauk SSSR, 251, 200-202, 1980.

56. Zhitkovskii, Yu.Yu., "Comparison of the Sharp-Pulse (Explosion) and CW-Burst Methods For Measuring the Intensity of Sound Scattering By the Ocean Bottom", p.88 in Proc. Eighth All-Union Acoustics Conf., (in Russian), Sec. N, Moscow,1973.

57. Bunchuk, A.V., Zhitkovskii, Yu.Yu., "Sound Scattering by the Ocean Bottom in Shallow Water Regions", Soviet Physics-Acoustics, 26, 363-370, 1980.

58. Ivakin, A.N., Lysanov, Yu.P., "Underwater Sound Scattering by Volume Inhomogeneities of a Bottom Bounded by a Rough Surface", Soviet Physics-Acoustics, 27, 212-215, 1981.

59. Ivakin, A.N., Lysanov, Yu.P., "Backscattering of Sound From an Inhomogeneous Bottom at Small Grazing Angles", Soviet Physics-Acoustics, 31, 236-237, 1985.

60. Ivakin, A.N., "Sound Scattering By Random Inhomogeneities of Stratified Ocean Sediments", Soviet Physics-Acoustics, 32, 492-496, 1986.

61. Brekhovskikh, L.M., J. Exptl. Theoret. Phys, USSR, 23, 275-289, 1952. (Translated by R.M. Goss, U.S. Navy Electronics Laboratory Report, San Diego, Calif.)

62. Parker, J.G., "Reflection of Plane Sound Waves from a Sinusoidal Surface", JASA, 29, 377-380, 1957.

63. Jordan, R.J., "Reflection of a Plane Sound Wave by a Sinusoidal, Pressure-Release Surface", M.Sc. Thesis, T.U.N.S., Halifax, Canada, 1967.

64. Fortuin, L., "Survey of Literature on Reflection and Scattering of Sound Waves at the Sea Surface", JASA, 47, 1209-1228, 1970.

65. Heaps, H.S., "Reflection of Plane Waves of Sound from a Sinusoidal Surface", J. Applied Phys., 28, 815-818,1957.

66. Meecham, W.C., "Fourier Transform Method for the Treatment of the Problem of the Reflection of Radiation from Irregular Surfaces", JASA, 28, 370-377, 1956.

67. MacKenzie, K.V., "Bottom Reverberation for 530- and 1030-cps Sound in Deep Water", JASA, 33, 1498-1504, 1961.

68. Patterson, R.B., "Backscatter of Sound from a Rough Boundary", JASA, 35, 2010-2013, 1963.

69. McKinney, C.M., Anderson, C.D., "Measurements of Backscattering of Sound from the Ocean Bottom", JASA, 36, 158-163, 1964.

70. Wong, H.K., Chesterman, W.D., "Bottom Backscattering near Grazing Incidence in Shallow Water", JASA, 44, 1713-1718, 1968.

71. Boehme, H., Chotiros, N.P., Rolleigh, L.D., Pitt, S.P., Garcia, A.L., Goldsberry, T.G., Lamb, R.A., "Acoustic Backscattering at Low Grazing Angles From the Ocean Bottom. Part 1. Bottom Backscattering Strength", JASA, 77, 962-974, 1985.

72. Jackson, D.R., Baird, A.M., Crisp, J.J., Thomson, P.A.G., "High-Frequency Bottom Backscatter Measurements in Shallow Water", JASA, 80, 1188-1199, 1986.

73. Urick, R.J., Principles of Underwater Sound, McGraw Hill, 2nd Edition, 1975.

74. Berktay, H.O., "Possible Exploitation of Non-Linear Acoustics in Underwater Transmitting Applications", J. Sound Vib., 2, 435-461, 1965.

75. Muir, T.G., Blue, J.E., "Transient Response of the Parametric Acoustic Array", Proceedings: Conference of Non-Linear Acoustics, 1969.

76. Berktay, H.O., Smith, B.V., Braithwaite, H.B., Whitehouse, M., "Sub-Bottom Profilers Using Parametric Sources", Proceedings of the Conference on Applications of Non-Linear Acoustics, University of Bath, England, 1979.

77. Beckett, C., private communication.

78. Humphrey, V.F., "The Measurement of Acoustic Properties of Specimens of Limited Size By Use of a Parametric Source", University of Bath, England, 1983.

79. Berktay, H.O., Shooter, J.A., "Nearfield Effects in End-Fire Line Arrays", JASA, 53, 550-556, 1973.

80. MacKenzie, K.V., "Reflection of Sound From Coastal Bottoms", JASA, 32, 221-231, 1960.

81. Thomas, P.R., Pace, N.G., "Broadband Measurements of Acoustic Attenuation in Water-Saturated Sands", Ultrasonics, 13-16, Jan., 1980.

82. Ewing, W.M., Jardetzky, W.S., Press, F., Elastic Waves in Layered Media, McGraw Hill, New York, 1957.

83. Hamilton, E.L., "The Elastic Properties of Marine Sediments", J. Geophys. Res, 76, 579-604, 1971.

84. Brekhovskikh, L.M., Waves in Layered Media, 2nd ed., Academic Press Inc., London, 1980.

85. Jeffreys, H., Jeffreys, B., Methods of Mathematical Physics, 3rd ed., Cambridge Univ. Press, Cambridge, 1956.

86. Kinsler, L.E., Frey, A.R., Coppens, A.B., Sanders, J.V., Fundamentals of Acoustics, 3rd ed., Wiley, New York, 1982.

87. Press, W.H., Flannery, B.P., Teukolsky, S.A., Vetterling, W.T., Numerical Recipes, The Art of Scientific Computing, Cambridge Univ. Press, Cambridge, 1986.